A SEISMIC FRAMEWORK FOR ESTIMATING HYDROCARBON RESERVOIR VOLUMES AND THEIR LIKELIHOOD

A Thesis

Presented to

the Faculty of the Department of Earth and Atmospheric Sciences

University of Houston

In Partial Fulfillment

of the Requirements for the Degree

Master of Geophysics

By

Henrique A. Fraquelli

May, 2012

A SEISMIC FRAMEWORK FOR ESTIMATING HYDROCARBON RESERVOIR VOLUMES AND THEIR LIKELIHOOD

Henrique A. Fraquelli

APPROVED:

Dr. Robert Stewart, Chairman
Dept. of Earth and Atmospheric Sciences

Dr. Fred J. Hilterman
Dept. of Earth and Atmospheric Sciences

Dr. Thomas Holley
Department of Chemical & Biomolecular Engineering

Dean, College of Natural Sciences and Mathematics

ACKNOWLEDGEMENTS

• I wish to express my appreciation for my advisor Prof. Robert Stewart for his advice, encouragement, and vision, which allowed the work that now is materialized in this thesis.

• I would like to thank Prof. Fred J. Hilterman by the well log dataset from Gulf of Mexico which him generously provided for the second part of this thesis, and also by advices during the first steps of this research.

• I would like to thank Prof. Don Van Nieuwenhuise by all help that him provided to me in the University of Houston.

• I would like to thank the love and encouragement of my wife, Luciana Aita de Oliveira, which made it possible for me to bear the difficulties and challenges of my research work. I also would like to thank my son, Thiago Aita de Oliveira Fraquelli, by all the special things that the simple existence of him allowed me to feel.

• I would like to express my thankfulness to my aunt Ana Elisa Aita-Cherry, Dave Cherry, Jane Bauman Cherry, and Cecilia Aita-Cherry, for all help and availability that they provided to me and my family in the entire period of time that we have been lived in Houston.

• I would like to thank Petrobras, my company, by the support to me in my research in the University of Houston.

• I would like to thank University of Houston for the opportunity of living the special academic environmental that only the great universities can provide.

A SEISMIC FRAMEWORK FOR ESTIMATING HYDROCARBON RESERVOIR VOLUMES AND THEIR LIKELIHOOD

An Abstract of a Thesis

Presented to

the Faculty of the Department of Earth and Atmospheric Sciences

University of Houston

In Partial Fulfillment

of the Requirements for the Degree

Master of Geophysics

By

Henrique A. Fraquelli

May, 2012

Abstract

This thesis develops a framework to estimate the likelihood in fluid volumes in a hydrocarbon reservoir. It uses 3C-3D seismic data and well logs from the Blackfoot oilfield (Alberta-Canada). Results from cross validation techniques applied to distribution maps generated using the geostatistic method (thickness and percentage of sand) and the neural network method (porosity) are used to estimate the uncertainty related with the predicted distributions in the case of the Blackfoot oilfield (AB-Canada). These distribution maps as well as the estimated uncertainty associated with them are used as inputs in two different approaches for the application of uncertainty analysis in the estimation of hydrocarbon volumes (a Taylor expansion approach and a Monte Carlo approach). The results obtained using these two approaches give compatible hydrocarbon volume estimates for the Blackfoot pool, with P10$\sim$ 12 MMbbl, P50$\sim$ 8 MMbbl, and P90$\sim$ 5 MMbbl. Investigation about sources of uncertainty in seismic data revealed that the time picking error could explain, in the case of the Blackfoot reservoir, the uncertainty in the thickness parameter.

In the second part of this project, well log data from the Gulf of Mexico are used together with fluid substitution method and uncertainty analysis to evaluate how the observed variability in rock properties of the Gulf of Mexico for each specific depth value affects the response of the attributes that respond to fluid discrimination. A larger concern for deeper reservoirs was identified in the predicted results. Nevertheless, the fluid substitution results were considered robust in most conditions investigated in this project, allowing discrimination of gas, fizz gas, and water saturated reservoirs in some of the attributes that respond to the fluid content. This last result could allow the estimate of the missing parameter in the HCPV estimation: the hydrocarbon saturation distribution map.

Contents

1 Introduction **1**

1.1 The general problem 1

1.2 Study area and data employed 8

1.3 Objectives 10

1.4 Methodology 11

1.5 Thesis outline and implementation 12

1.6 Statistics and Monte Carlo simulation 13

1.6.1 Basic statistics 13

1.6.2 PDF's and CDF's 14

1.6.3 Monte Carlo simulation 16

1.7 Reservoir volume estimation methods 18

1.8 Fluid discrimination 19

2 Reservoir volume estimation and confidence **21**

2.1 The volumetric method 21

2.1.1 Deterministic versus Probabilistic methods 23

2.1.2 Reserves and resources 25

2.2 Geostatistic analysis 28

2.3 Estimating the reservoir volume confidence – the Blackfoot reservoir . 29

2.3.1 Uncertainty in thickness and percentage of sand 30

2.3.2 Uncertainty in the porosity 36
2.3.3 Uncertainty in the oil saturation 38
2.3.4 Uncertainty in the area of the reservoir 40
2.4 HCPV and its likelihood 42
2.4.1 Taylor expansion approach 44
2.4.2 Monte Carlo approach 46
2.4.3 Comparison of the results 50
2.5 Seismic error analysis 52
2.6 Ultimate recovery confidence – additional case 54

3 Estimating fluid discrimination 62
3.1 Applying the fluid substitution method 63
3.2 Characterizing the well log dataset 67
3.2.1 Non-seismic attributes/properties 67
3.2.2 Seismic attributes/properties 70
3.3 Fluid substitution 78
3.3.1 Monte Carlo simulation, fluid discrimination, & the effect of depth 85

4 Summary of conclusions 97

5 Future work 100

Bibliography 104

A Thickness error from the time picking error 108

List of Figures

1.1 A 3D reservoir scheme presenting the gas/oil contact (GOC) and the oil/water contact (OWC) (modified from Tearpock, 2011). 5

1.2 Base map of Blackfoot area. The 3C-3D survey area was inside the dashed line (from Lawton et al., 1996) in the right map. 9

1.3 PDF and CDF of a normal distribution (Gaussian distribution). . . . 15

1.4 Schematic of Monte Carlo simulation (from Jahn et al., 1998). 17

2.1 The two axis PRMS system: resources classification framework. . . . 27

2.2 Interrelationship of formation thicknesses (from Worthington, 2009). 32

2.3 Two results presented in Todorov and Stewart (1997). *Left*: Vp/Vs ratio distribution as obtained from the 3C-3D seismic data. *Right*: Vp/Vs (from seismic) versus Gamma-ray (from well logs). A good correlation between the two parameters can be observed. 35

2.4 Two results presented in Todorov (2000). *Left*: The Gamma ray index after cokriging. The Blackfoot reservoir is inside the encircled red line. *Right*: result of the cross validation test for the gamma ray index cokriging. 36

2.5 Histogram representing the error distribution for the gamma-ray index, as obtained using the cross validation test (see text for details). . . . 37

2.6 The area-depth method, from Jahn et al. (1998). 41

2.7 The area-thickness method, from Jahn et al. (1998). 43

2.8 The oil column distribution as in Todorov (2000). 44

2.9 Cumulative distribution function for the hydrocarbon pore volume estimation. Hollow square/red: Taylor expansion method. Black/diamond symbol: Monte Carlo approach. Green square: estimate of Todorov and Stewart. 47

2.10 Standard deviation of the estimated hydrocarbon volume obtained from the Monte Carlo simulation. When the number of simulations increases (shown in the horizontal axis of the graphics), the value associated with the predicted standard deviation (shown in the vertical axis) becomes stable. 49

2.11 Histogram of one realization of the Monte Carlo simulation applied to the volumetric calculation. The left vertical axis scale shows the relative number of simulations associated with each bin of the histogram. The right vertical axis scale shows the value associated with the CDF related to the simulated sample obtained from the Monte Carlo simulation. The blue/dark points show the value associated with the PDF for each bin, and the purple points/line show the equivalent normal distribution which would be obtained using the mean and the standard deviation value of the simulated sample. The yellow/light points/line show the CDF curve associated with the simulated sample. 50

2.12 Spectral response curve for PP (left) and PS (right) data (from Goodway and Tessman, 2001). 54

2.13 Cumulative distribution function for the hydrocarbon pore volume estimation. Hollow square: Taylor expansion method. Solid diamond: Monte Carlo approach. 59

2.14 Cumulative distribution function for the ultimate recovery estimation. Orange/square: Taylor expansion method – normal PDF case. Blue/diamond symbol: Monte Carlo approach. Hollow circle: Demirmem (2007) predictions. Star symbol: Taylor expansion method – lognormal PDF case. 60

2.15 Cumulative distribution function for the HCPV estimation for Blackfoot reservoir. Little square: Taylor expansion method – normal PDF case. Blue/diamond: Monte Carlo approach. Large square/green: Todorov-Stewart estimation. Star symbol: Taylor expansion method – lognormal PDF case. 61

3.1 Temperature versus depth. The blue/diamond points represent the sample data, while the magenta/square points represent the average value for each depth interval. 68

3.2 Pore pressure versus depth. The blue/diamond points represent the sample data, while the magenta/square points represent the average value for each depth interval. 69

3.3 Overburden pressure (blue/diamond) and Pore pressure (red/square) versus depth. 70

3.4 Average V_P versus depth. The blue/square points represent the wet sand samples, while the green/diamond points represent the shale samples. 71

3.5 Average bulk density versus depth. The blue/square points represent the wet sand samples, while the green/diamond points represent the shale samples. 72

3.6 V_P/V_S ratio versus depth. Wet sand: The sample data points are shown in blue/diamond, and the average value for each depth interval is shown in magenta/square. Shale: the sample data is shown in red/circle, and the average value for each depth interval is shown in green/triangle. . 73

3.7 Porosity for wet sand versus depth. Blue/diamond: sample data points. Magenta/square: average value for each depth interval. 75

3.8 Bulk modulus for wet sand versus porosity. Blue/diamond show sample data points, while magenta/square symbols show the average value of the sample points for each depth interval. Cyan line shows the Reuss modulus, while Green line shows the Voigt modulus. Black dashed line shows the Hill's modulus. A regression curve was fitted to the average value of the sample points for each specific depth, and is presented as a magenta dashed line. 77

3.9 Vp/Vs ratio versus Vp. Green/diamond: average value for each depth for shale. Blue/square: average value for each depth for wet sand (Sw= 1.0). Magenta/circle: average value for each depth for sands with Sw = 0.95 (fizz case). Yellow/triangle: average value for each depth for sands with Sw = 0.5. 80

3.10 P-Impedance versus S-impedance. Green/diamond: average value for each depth for shale. Blue/square: average value for each depth for wet sand (Sw= 1.0). Magenta/circle: average value for each depth for sands with Sw = 0.95 (fizz case). Yellow/triangle: average value for each depth for sands with Sw = 0.5. 81

3.11 NI versus PR. Green: average value for each depth for shale. Blue/square: sample data points for wet sand (Sw= 1.0). Magenta/square: average value for each depth for the wet sand case. Red/circle: average value for each depth for sands with Sw = 0.95 (fizz case). Yellow/triangle: average value for each depth for sands with Sw = 0.5. Dashed-dot lines: linear fitting for the sample data points for wet sand (light pink) and for the average value for each depth for shale (green). 83

3.12 $\lambda\rho$ versus $\mu\rho$. Green points: average value for each depth for shale. Blue/square: sample data points for wet sand (Sw= 1.0). Magenta/square: average value for each depth for wet sand case. Red/circle: average value for each depth for sands with Sw = 0.95 (fizz case). Yellow/triangle: average value for each depth for sands with Sw = 0.5. . 84

3.13 Illustration of the procedure to obtain the statistical properties of the original information in the well log dataset. Z1 and Z2 correspond to different depths. The mean and the standard deviation for each original well logged property was calculated for each specific depth. These statistical parameters were used as source parameters for the Monte Carlo simulation. 86

3.14 Different crossplots which are sensitive to fluid discrimination at depth= 0.64 km. Left/top: Vp/Vs vs. Vp. Right/top: $\mu\rho$ vs. $\lambda\rho$. Left/bottom: PR vs. NI. Right/bottom: I_S vs. I_P. In all plots, the symbols are: Blue/square: sample data points for wet sand (Sw= 1.0). Magenta/square: fizz gas case. Yellow/triangle: gas reservoir case ($S_{,}$ = 0.50). The big circle inside the distribution of points corresponds to its respective median point. 89

3.15 Different crossplots which are sensitive to fluid discrimination at depth= 1.25 km. Left/top: Vp/Vs vs. Vp. Right/top: $\mu\rho$ vs. $\lambda\rho$. Left/bottom: PR vs. NI. Right/bottom: I_S vs. I_P. In all plots, the symbols are: Blue/square: sample data points for wet sand (Sw= 1.0). Magenta/square: fizz gas case. Yellow/triangle: gas reservoir case ($S_{,}$ = 0.50). The big circle inside the distribution of points corresponds to its respective median point. 90

3.16 Different crossplots which are sensitive to fluid discrimination at depth= 1.62 km. Left/top: Vp/Vs vs. Vp. Right/top: $\mu\rho$ vs. $\lambda\rho$. Left/bottom: PR vs. NI. Right/bottom: I_S vs. I_P. In all plots, the symbols are: Blue/square: sample data points for wet sand (Sw= 1.0). Magenta/square: fizz gas case. Yellow/triangle: gas reservoir case ($S_{,}$ = 0.50). The big circle inside the distribution of points corresponds to its respective median point. 91

3.17 Different crossplots which are sensitive to fluid discrimination at depth= 2.10 km. Left/top: Vp/Vs vs. Vp. Right/top: $\mu\rho$ vs. $\lambda\rho$. Left/bottom: PR vs. NI. Right/bottom: I_S vs. I_P. In all plots, the symbols are: Blue/square: sample data points for wet sand (Sw= 1.0). Magenta/square: fizz gas case. Yellow/triangle: gas reservoir case ($S_{,}$ = 0.50). The big circle inside the distribution of points corresponds to its respective median point. 92

3.18 Different crossplots which are sensitive to fluid discrimination at depth= 2.90 km. Left/top: Vp/Vs vs. Vp. Right/top: $\mu\rho$ vs. $\lambda\rho$. Left/bottom: PR vs. NI. Right/bottom: I_S vs. I_P. In all plots, the symbols are: Blue/square: sample data points for wet sand (Sw= 1.0). Magenta/square: fizz gas case. Yellow/triangle: gas reservoir case ($S_{,}$ = 0.50). The big circle inside the distribution of points corresponds to its respective median point. 93

3.19 Different crossplots which are sensitive to fluid discrimination at depth= 3.40 km. Left/top: Vp/Vs vs. Vp. Right/top: $\mu\rho$ vs. $\lambda\rho$. Left/bottom: PR vs. NI. Right/bottom: I_S vs. I_P. In all plots, the symbols are: Blue/square: sample data points for wet sand (Sw= 1.0). Magenta/square: fizz gas case. Yellow/triangle: gas reservoir case ($S_{,}$ = 0.50). The big circle inside the distribution of points corresponds to its respective median point. 94

3.20 Different crossplots which are sensitive to fluid discrimination at depth= 3.57 km. Left/top: Vp/Vs vs. Vp. Right/top: $\mu\rho$ vs. $\lambda\rho$. Left/bottom: PR vs. NI. Right/bottom: I_S vs. I_P. In all plots, the symbols are: Blue/square: sample data points for wet sand (Sw= 1.0). Magenta/square: fizz gas case. Yellow/triangle: gas reservoir case ($S_{,}$ = 0.50). The big circle inside the distribution of points corresponds to its respective median point. 95

A.1 Schematic for the total time picking error. 109

List of Tables

2.1 Information data used in the calculations (modified from Demirmem, 2007). 57

2.2 Predicted UR from Demirmem, 2007) and from the Taylor expansion and Monte Carlo methods (Section2.4) 58

Chapter 1

Introduction

1.1 The general problem

Seismic data has been used to great advantage in the exploration of petroleum resources. Seismic is used in the construction of formation structure maps, which have to be tied to well log data. In addition, other elements of the basic geometry of the hydrocarbon trap (e.g. fault) can be derived from seismic data. Recently, the seismic technology has been recognized as a reliable technology after the update of the regulations published by the US. Securities and Exchange Commission in 2008 (Sidle and Lee, 2011; US SEC 2008). This means that seismic can now be used to validate and report petroleum resources and reserves. The general problem related to the evaluation of the volumetric information related to hydrocarbon reservoirs, which uses seismic as a fundamental tool, is the subject of this thesis.

The purpose of seismic interpretation is to extract all available geologic information from the seismic data. To do so, seismic data must be understood, specifically what are the properties related to the origin of the seismic response. Seismic reflections are related to the interfaces where the acoustic properties of the rocks change – typically, the density ρ and the compressional (P-wave) and shear (S-wave) velocities, V_p and V_s respectively. The amplitude of these reflections (the seismic response) is calculated from the contrasts of the impedances associated with this interface. Thus, seismic amplitudes represent contrasts in elastic properties between individual layers.

Brown et al. (2011), divided the principal reservoir properties that affect seismic amplitude in two groups. The first group, which contains the nature of the fluid, the gross lithology, the pressure, and the temperature, affects the reservoir as a whole (in first approximation). The second group, which contains porosity, net pay thickness or net-to-gross ratio, lithological detail, and hydrocarbon saturation, is formed by reservoir properties that can vary laterally over short distances. Thus, the second group presents reservoir properties that significantly affect the reserve estimates of a reservoir penetrated by a small number of wells. Still following Brown et al., lateral changes in amplitude of reservoir reflections can be caused by changes in any one or more of these second group of reservoir properties (i.e., there is an inherently ambiguity). Thus, Brown et al. point out that the interpretative approach to reservoir evaluation requires that simplifying assumptions be made.

Many of the properties that affect the seismic response can be measured directly using well logging tools or core samples. Thus, to fully understand the seismic reflections, rock physics modeling can be used as an important and useful tool associated with the seismic interpretation procedure. To do so, all well log data should first be

edited for borehole effects, balanced, and classified on basis of quality (Brown et al., 2011). In addition, when comparing seismic data with well log data, scale differences must to be taken into account. With this considerations in mind, integration between seismic data and well log data, or seismic interpretation and well log interpretation, constitutes a fundamental process in any reservoir characterization process.

From a purely seismic point of view, seismic interpretation implies picking and tracking laterally consistent seismic reflectors for the purpose of mapping geologic structures, stratigraphy and reservoir architecture. The geometrical expression of seismic reflectors is then mapped in space and time. The ultimate goal of seismic interpretation is to detect hydrocarbon accumulations, delineate their extent, and calculate their volumes (PRMS-AD, 2011). Quantitative seismic interpretation techniques can validate hydrocarbon anomalies and give additional information during prospect evaluation and reservoir characterization (Avset et al., 2005). Among these techniques are amplitude versus offset (AVO) analysis, acoustic and elastic impedance inversion, and forward seismic modeling. One of the main advantages of the 3D seismic data compared to well log data is that the former provides a better coverage of the geologic area associated with a hydrocarbon field. However, the seismic data is band-limited and is also contaminated by complex noise and phase errors. Hence, even if a seismic anomaly is present and fits the structure well, the anomaly by itself significantly lowers risk but is probably insufficient for a reporting of reserve volumes until confirmed by well control (PRMS-AD, 2011). As additional development wells are drilled and logged, the interpretation of the seismic data is revised and recalibrated. Aspects of the seismic interpretation that were initially ambiguous become

more reliable and detailed as uncertainties in the relationship between seismic parameters and field properties are reduced (PRMS-AD, 2011). Thus, in any part of the seismic interpretation process, integration of seismic with well log data interpretation is fundamental, since this integration of geophysical data allows to increasing confidence in the geophysical interpretation.

Figure 1.1 shows a schematic for a 3D reservoir presenting a gas/oil contact (GOC) and an oil/water contact (OWC). Figure 1.1 is also useful to illustrate some of the difficulties associated with the quantification of hydrocarbon volumes in reservoirs. To evaluate the reservoir's hydrocarbon volume, each one of the fluid phases presented in the reservoir must be mapped, as well as the boundaries related to the top and base of the reservoir. Thus, when a seismic amplitude anomaly is identified as the result of hydrocarbon saturation, the gas/oil and/or hydrocarbon/water contacts (GOC, GWC, or OWC) themselves can be mapped across the 3D seismic volume by noting where the amplitude anomalies terminate downdip (PRMS-AD, 2011). The amplitude interpretation must be geologic consistent with structural interpretation (Hilterman, 2001). Hence, the terminations of the amplitude anomalies should occur at a common structural contour within the sedimentary fairway, which is interpreted as the base of the trapped hydrocarbon - and a possible flat spot maybe observed. As discussed in Hilterman (2001), flat spots are enhanced if the reservoir is thick, presents enough dip and is identified on 3D seismic data.

However, if the downdip termination of the anomaly does not follow a structural contour within the reservoir fairway, there is risk that the seismic amplitude anomaly is not caused by the presence of hydrocarbon. Another possibility is that the hydrocarbon reservoir is too thin and/or too steeply dipping to exhibit a readily observable

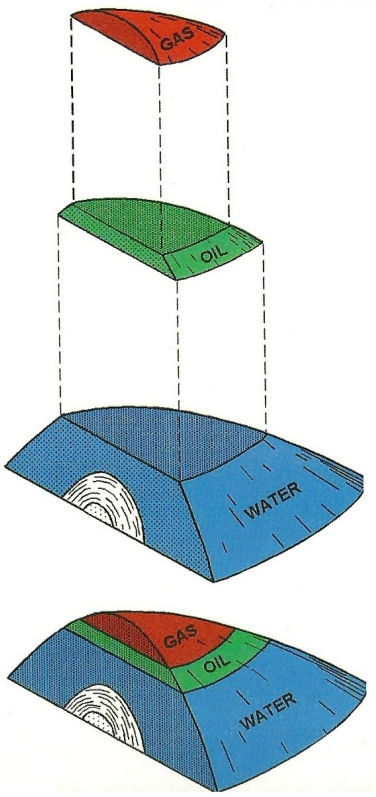

Figure 1.1: A 3D reservoir scheme presenting the gas/oil contact (GOC) and the oil/water contact (OWC) (modified from Tearpock, 2011).

flat spot but a seismic anomaly is present and fits the structure well; in this case the anomaly by itself significantly lowers risk but is probably insufficient for the reporting of reserve volumes until confirmed by well control (PRMS-AD, 2011). Through integration with well data and reservoir penetrations, the presence of a hydrocarbon accumulation can be confirmed, and the seismic amplitude data can be extrapolated from well control. This extrapolation to locations away from the wells can be done by generating *facies models* using several wells in the area (e.g. using geostatistic analysis), or by correlating them to certain attributes from seismic data (e.g. using a neural network method). The latter requires accurate correlation of the wells with

the seismic data, as well as the definition of appropriate rock physics models. In fact, rock physics is an essential link connecting seismic data to the presence of in situ hydrocarbons and to reservoir characteristics (Han and Batzle, 2004). Modeling the effects of fluid on rock velocity and density is a basic method used to estimate the influence of pore fluids on seismic data. With this purpose, Gassmann's equations are the relation most widely used to calculate seismic velocity changes resulting from different fluid saturations in reservoirs.

The use of multicomponent seismic data is an improvement in the seismic characterization of a hydrocarbon reservoir when compared to traditional P-wave seismic data. Coupled PP and PS seismic interpretation increases the confidence of the geophysical interpretation, as multicomponent seismic data add new measurements for investigate the subsurface. Through the analysis of multicomponent seismic data, rock properties as V_P/V_S can be estimated directly from the data, thus improving the predictions related to mineralogy, porosity, and reservoir fluid type (Miller, 1996). In general, two parameters (i.e., P- and S-impedance, or P- and S-wave velocity) can often be estimated from PP and PS seismic inversion (Miller, 1996).

The V_P/V_S value extracted from multicomponent data can also be used to identify sand channels, as the increase in V_P/V_S with shaliness has been used in seismic field studies to outline sandstone channels encased in shales (McCormack et al., 1984; Garotta et al., 1985). This use for V_P/V_S is validated by well control, as a decrease in V_P/V_S correlates with an increase in sand channel thickness as determined from well log data (McCormack et al., 1984; Garotta et al., 1985). Thus, multicomponent seismic data can provide an important contribution to the characterization of a hydrocarbon reservoir. This contribution will be described in more detail in Chapter

2.

A last comment about the general problem related to the reservoir volume estimation is that, whatever the methodology used for estimation of resource quantities for an accumulation of hydrocarbons, it is subject to uncertainty, and should be expressed as a range. Thus, uncertainty can be defined as the range of possible outcomes in an estimate (GEPRR, 2001). The use of uncertainties allows to assessing the risk and optimal decision-making related to some accumulation of hydrocarbon. In addition, the use of uncertainties allows a better integration among data from different sources and of different types, and allows also the estimation of the value of additional data (Avseth et al, 2005).

Recently, Sidle and Lee (2008) discussed a methodology to quantifying the reliability and value of the 3D seismic data. The authors applied a value-of-information model that includes multiple targets, budgetary constraints, and qualitative models relating poststack seismic amplitudes and amplitude-variation-with-offset (AVO) parameters to the quantities of interest for reservoir characterization, such as porosity and reservoir thickness. The geophysical methods described in their work incorporate uncertainty in the rock properties (e.g., porosity), errors in acquisition and processing, and other reservoir properties (e.g., thickness), allowing oil companies to base seismic accuracy assessments on hard data instead of expert assessment. The work of Sidle and Lee (2008) is related to one of the objectives of this thesis, since when we assess the uncertainties associated with some data/calculation, we can make a better interpretation of the results. In the following chapters, uncertainty analysis will be used to evaluate the confidence of the geophysical estimations carried out in this thesis.

1.2 Study area and data employed

This thesis uses two different datasets, each one selected to achieve a different goal within the umbrella of likelihood. To investigate the reservoir volume uncertainty, as associated with the volumetric method (see Chapter 2), the Blackfoot reservoir (AB-Canada) was selected. A reason for this selection is that there is published research available for this reservoir, which is able to provide the information needed to carry out a study about the confidence of the estimation of hydrocarbon volumes. A second dataset is associated with the Gulf of Mexico, and it was selected because the available data allows an extended use of uncertainty analysis to be applied to fluid discrimination evaluation.

The Blackfoot field is located southeast of Calgary, in Alberta, Canada, in Township 23, Range 23 (see Figure 1.2). The hydrocarbon reservoir associated with the Blackfoot field is the Glauconitic sandstone which is encountered at a depth of approximately 1550 m and the valley-fill sediments vary from 0 to over 35 m in thickness (Miller, 1996). The reservoir is made up of quartz sandstones with an average porosity of approximately 18%. Hydrocarbon reservoirs are found in structural and stratigraphic traps where porous channel sandstones pinch out against non-reservoir regional strata or low-porosity channel sediments. The main production zone in the Blackfoot area is the upper Glauconitic Group and the primary fluid in the upper incised valleys is oil (Feng, 2009). Gas is occasionally present in the upper channel valleys and whenever it comes out of solution (Miller, 1996; Lu and Margrave, 2001).

The acquisition parameters associated with the 3C-3D seismic data used in this

thesis is available in Lawson et al. (1996) and the survey was processed with PROMAX software by the CREWES Project, University of Calgary (Lu and Margrave, 1998). A comprehensive explanation of the data associated with this thesis, as well as about the Blackfoot reservoir, is discussed in Todorov (2000).

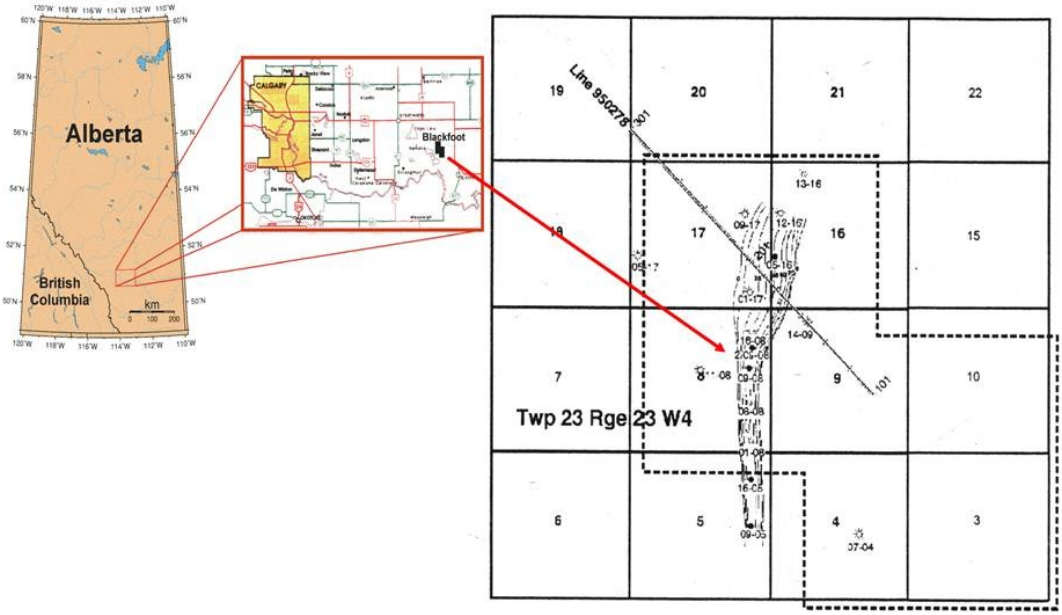

Figure 1.2: Base map of Blackfoot area. The 3C-3D survey area was inside the dashed line (from Lawton et al., 1996) in the right map.

The other region investigated in this thesis is in the shallow part of the Gulf of Mexico. The well log dataset used in this analysis was provided generously by Professor Fred J. Hilterman. This well log dataset contains 1,740 samples presenting measurements for 6 different properties (density for shale and for wet sand, P-wave velocity for shale and for wet sand, temperature, and mud weight). The well log samples are from depths of 0.21 km to 3.75 km.

1.3 Objectives

The objectives related to this thesis can be better described separately for the goals related for each dataset associated with this thesis, given the main goal which is related to both datasets: the investigation of the range of values resulting from a span of inputs. In addition, the objectives will be described as questions that I intend to answer in this project. These questions are

Part 1 – Blackfoot reservoir: a) How can we estimate the uncertainty related to geostatistical results? How may we use this uncertainty in the reservoir hydrocarbon pore volume (HCPV) estimation process? b) How will we associate uncertainty with probability in the estimation of geophysical properties? c) How would we associate a numerical probability with results obtained using a deterministic approach? d) Are the uncertainties originating in the seismic as well as in the well log data related to the uncertainty in the reservoir HCPV obtained from geostatistical analysis?

Part 2 – Gulf of Mexico: a) How does the observed spatial variability in a well log dataset influence the response of attributes that respond to fluid content in reservoirs? b) Is the fluid discrimination derived from fluid substitution robust when we consider the observed spatial variability in the measured properties of a well log dataset? c) How does depth affect the fluid discrimination in this case?

1.4 Methodology

In this thesis, I use two different datasets to investigate the two cases (two parts) being studied. In Part 1 of this thesis (Chapter 2), I first review the results obtained for Blackfoot oilfield (AB-Canada), as published in a series of papers by Todorov and Stewart (e.g. Todorov and Stewart, 1997; Todorov, 2000). These authors used 3C-3D multicomponent seismic data and well log data to generate distribution maps for thickness, percentage of sand, and porosity associated with the Blackfoot oilfield. The thickness and the percentage of sand distributions were generated by the authors using the cokriging geostatistical method (Isaaks and Srivastava 1989), while the porosity distribution was obtained using seismic inversion and the neural network methods (Todorov, 2000). From these distributions and the oil saturation in the Blackfoot field the authors derived an oil column distribution map (shown in Figure 2.8).

Cross validation techniques were applied by Todorov and Stewart (1997) to their results to evaluate the reliability of the final distributions. I use these cross-validation results as published by Todorov (2000), which present the associated absolute error obtained using the blind well procedure, as a way to estimate the uncertainty associated with the distribution maps of porosity, thickness, and percentage of sand. The saturation uncertainty is estimated using the well log data available to the Blackfoot reservoir. Using two different approaches, a Taylor expansion approach (Coleman and Steele, 2009) and a Monte Carlo simulation approach (Avseth et al. 2005), I can propagate the uncertainties associated with the source parameters needed for the hydrocarbon pore volume (HCPV) estimation to the HCPV estimated value itself.

In Part 2 of this thesis (Chapter 3), I use a well log dataset containing 1740

samples from the Gulf of Mexico presenting measured values for P-wave velocity (Vp) for shale and for wet sand, density for shale and for wet sand, temperature, and mud weight to investigate the questions listed in the objectives section of this thesis. I use the Gassmann's equation, the Monte Carlo simulation, and the observed variability in the sample values for specific depths to investigate their effect on the results of the fluid discrimination technique. The crossplots involving P-Impedance versus S-Impedance, NI versus PR, $\lambda\rho$ versus $\mu\rho$, and Vp/Vs versus Vp (all of them described in Hilterman, 2001) were selected to carry out this evaluation.

In this thesis, I have used the Hampson-Russell software to analyse and extract information from well log data. In addition, I have used Matlab, Scilab and MS-Excel to analyse well log data and to carry out the calculations associated with uncertainty analysis.

1.5 Thesis outline and implementation

Sections 1.6 through 1.8 present a discussion about the background needed to better understand the ideas developed in the following chapters; specifically, statistical knowledge, reservoir volume estimation methods and fluid substitution method are addressed. Chapter 2 presents the discussion about reservoir volume estimation and confidence. Chapter 3 presents the discussion about fluid discrimination in gas reservoirs. Chapter 4 presents a summary of the results obtained in this thesis, and Chapter 5 describes ideas to be developed in future work.

1.6 Statistics and Monte Carlo simulation

1.6.1 Basic statistics

In the theory of statistics, the parent population refers to the number of possible measured values ξ_i, which in the case of this population consist of an infinite number of values. Two independent parameters, the mean μ and the standard deviation σ_{parent} characterize the parent distribution when it is a normal distribution. Both parameters are related to each other through the equation below

$$\sigma_{parent} = \sqrt{\frac{\sum (\xi_i - \mu)^2}{N_{parent}}} \tag{1.1}$$

In practice, when we take a series of measurements in an experiment x_i we take a selection, or sample, from this parent distribution which results in a distribution called sample distribution. This distribution is centered on the mean of the data set, $\overline{x}$, and has a standard deviation given by

$$\sigma_{sample} = s_x = \sqrt{\frac{\sum (x_i - \overline{x})^2}{N-1}} \tag{1.2}$$

The goal in statistical analysis is to make use of this sample distribution to estimate the mean and standard deviation of the parent distribution. In the limit that $N \to \infty$ the parent and sample distributions are the same and $\overline{x} = \mu$ and $\sigma_{sample} = \sigma_{parent}$.

Another statistical parameter that is important when we perform uncertainty analysis is the coefficient of variation. The coefficient of variation is given by the ratio of the mean value and the associated standard deviation. Thus, the coefficient of variation is a dimensionless quantity, and is used in general to compare uncertainty involving parameters with different physical units.

1.6.2 PDF's and CDF's

Uncertainty is related to our incomplete knowledge. To describe uncertainties in a quantitative way, it is common to model the uncertainties as random variables, and also the use of statistical probability density functions (PDFs) and cumulative distribution functions (CDFs) to describe the uncertainty quantity. The CDF is obtained by integrating the PDF, so that the value of the CDF for a random variable X is equal to the area at the left of x under the PDF plot (see Figure 1.3). Thus, for a random variable X in the range $x_i < X < x_f$, we have that the probability associated with the random variable X is given by

$$P(x_i < X < x_f) = \int_{x_i}^{x_f} f(x)\, dx \tag{1.3}$$

where f(x) is the PDF, and the CDF is obtained from equation 1.3 using x_i as the minimum possible value of the random variable X, so that $X \leq x_f$. The CDF describes the probability that a random variable X with a given probability distribution $f(x)$ will be found at a value less than or equal to x_f, which defines a quantile q for $X \leq x_f$. As described in Dubrule (2003), a P90 probability associated with a reservoir is the reverse of the CDF for a random variable equal to x_f. Hence, P90 means that 90% of the values for X are larger than or equal to x_i. The reverse cumulative probability function commonly is known as expectation curve. In terms of the direct CDF, P90 is equivalent to the quantile q_{10}, since 10% of the values for X are lower than or equal x_f.

The PDF and CDF distributions describe the uncertainty quantity. As described in Avseth et al. (2005), the moments related to the PDF (e.g., the mean, standard deviation) tell us about the central tendency and the spread of the random variable.

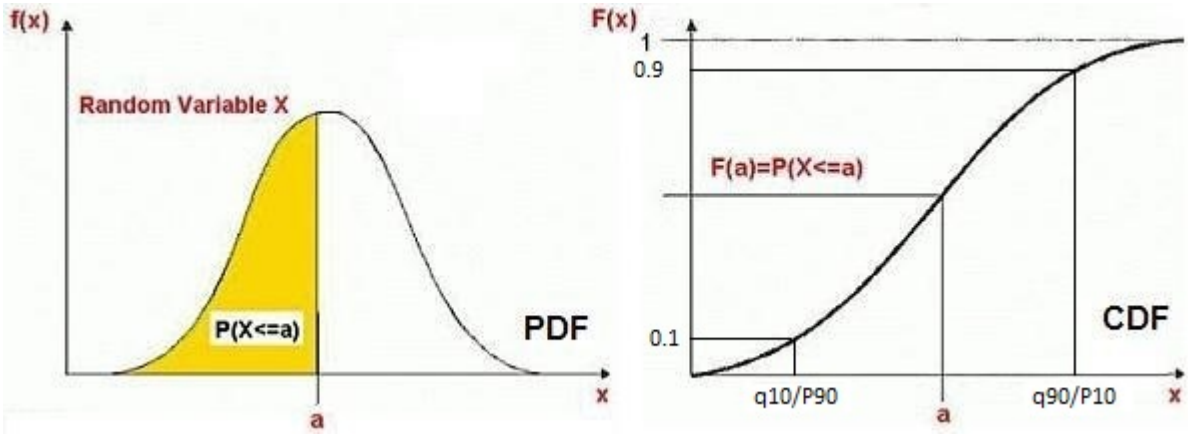

Figure 1.3: PDF and CDF of a normal distribution (Gaussian distribution).

One convenient way to handle the uncertainty related to a distribution of points in a sample, is the use of a parametric approach, in which we choose the PDF as a known function, and then estimate the parameters of the PDF from the data.

One convenient PDF is the Gaussian distribution, which is characterized by the mean and the standard deviation related to the sampled data. In the calculations carried out in this paper, the Gaussian distribution will be used to characterize the uncertainties associated with the available data. Investigations related to the use of different PDFs (e.g., lognormal distribution) will not be addressed in this thesis, but could be the subject of further scientific work. As an example of the use of different PDFs, one could say that the Gaussian distribution is often used to represent the PDF of porosity or of random errors, while the lognormal distribution often is used to model permeability (Dubrule, 2003).

The method presented in this thesis to estimate the uncertainty in the oil volume prediction makes use of the geostatistic analysis and the "blind well" procedure during the carrying out of the QC tests as describe in the Chapter 2. Thus, the absolute errors

related to the "blind well" tests are used to estimate the standard deviation necessary to characterize the PDF (Gaussian distribution) associated with the values predicted for each parameter. From this PDF, the CDF related to P10 (10% of probability associated with a predicted quantity) and P90 (90% of probability associated with a predicted quantity) are computed (Dubrule, 2003), providing an estimate of the uncertainty related to a specific value of the oil volume prediction. Chapter 2 discusses such a case.

1.6.3 Monte Carlo simulation

The Monte Carlo simulation is a powerful tool in uncertainty analysis. It is used in the volumetric estimation in the case of a probabilistic approach (PRMS-AD, 2011). The basic methodology of the Monte Carlo simulation is presented in Figure 1.4, which shows a schematic of Monte Carlo simulation (from Jahn et al., 1998). The Monte Carlo simulation generates a limited number of possible combinations of variables which approximates a distribution of all possible combinations (Jahn et al., 1998). As the number of sets of combinations increases, the result obtained from the Monte Carlo simulation gets closer of the theoretical result of using all possible combination. When the statistical moments related to the sample points simulated using the Monte Carlo simulation get stabilizes, the simulation can be halted.

In specific terms, let us discuss a theoretical example that describes how the Monte Carlo simulation works. Let us first assume that we have a variable X which we want to simulate from the multiplication of two independent parameters, α and β. To start the simulation to evaluate the uncertainty in X from the uncertainties in α and β, I

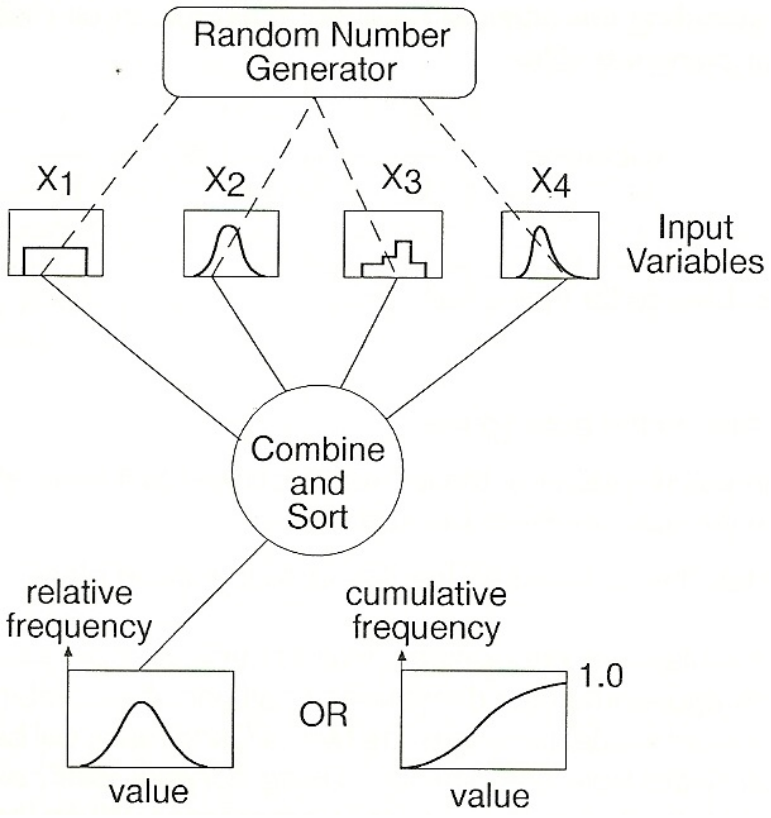

Figure 1.4: Schematic of Monte Carlo simulation (from Jahn et al., 1998).

assume that the central limit theorem is valid so that the errors for the variables α and β are from a *normal* parent population with mean α_{true} and standard deviation σ_α, in the case of the variable α, and with mean β_{true} and standard deviation σ_β, in the case of the variable β. Then, I run a numerical experiment using these parent populations for α and β. For these parent populations, N experiments are drawn randomly from each parent population specified. For each one of the simulated experiments I multiply in a deterministic manner the two simulated values for α and β. After enough numerical experiments, I can statistically characterize the variable X using the simulated values obtained for X.

If two variables are dependent, the value chosen in the simulation for the dependent variable can be linked to the randomly selected value of the first variable range (Section 3.3.1 presents an example of correlated Monte Carlo simulation). In addition, a different PDF can be chosen for each one of the parameters used as a source for the Monte Carlo simulation. A more detailed discussion of Monte Carlo simulation can be found in Coleman and Steele (2009) and Avseth et al. (2005).

1.7 Reservoir volume estimation methods

Different methods can be used to estimate the hydrocarbon volume associated with a reservoir. In general, a specified method is selected as corresponding to the developing phase of a hydrocarbon field. Three important methodologies to reserve estimation of hydrocarbon reservoirs are presented next.

Volumetric methods involve the calculation of reservoir rock volume, the hydrocarbons in place in that rock volume and the estimation of the portion of the hydrocarbons in place that ultimately will be recovered. After discovery, during initial delineation and development of a field, volumetric estimation is the key to estimation. Material balance methods of reserves estimation involve the analysis of pressure behavior as reservoir fluids are withdrawn. As depletion proceeds and adequate production data becomes, material balance may represent a practical second method. In general, material balance methods result in more reliable reserves estimates than volumetric estimates (PRMS-AD, 2011). Production decline analysis methods of reserves estimation involve the analysis of production behavior as reservoir fluids are

withdrawn. Analysis of production decline curve can provide estimation of three important items: remaining oil and gas reserves, future expected production rate, and remaining productive life of well or reservoir.

The volumetric estimation is the only means available to assess hydrocarbons in place prior to acquiring sufficient pressure and production information to apply material balance techniques (Dean, 2007). In general, recoverable hydrocarbons are estimated from the in place estimates and a recovery factor that is estimated from analogue pool performance and/or simulation studies. The volumetric method used to estimate the petroleum initial in place and analogous methods used to estimate recovery factors are used during exploration, discovery, appraisal, and initial development stages of the exploration and production cycle of any petroleum recovery project (PRMS-AD, 2011). Chapter 2 presents a more detailed discussion about the use of the volumetric method in hydrocarbon volume estimation.

1.8 Fluid discrimination

Given the bulk modulus and densities of fluids, the bulk modulus and density of the solid matrix, and the rock bulk modulus and density at a know saturation, the Gassmann's equation allows the calculation of the bulk modulus at any other saturation (Smith et al., 2003):

$$K_{sat} = K_{dry} + \frac{(1 - \frac{K_{dry}}{K_{ma}})^2}{\frac{\phi}{K_{fl}} + \frac{(1-\phi)}{K_{ma}} - \frac{K_{dry}}{K_{ma}^2}} \tag{1.4}$$

where K_{sat} is the saturated bulk modulus, K_{dry} is the bulk modulus of the porous rock frame, K_{fl} is the bulk modulus of the pore fluid, and ϕ is the porosity.

Basic assumptions involving the use of the Gassmann's equation (Wang, 2001) are given by: the rock (both the matrix and the frame) is macroscopically homogeneous and isotropic; all the pores are interconnected or communicating; the pores are filled with a frictionless fluid (liquid, gas, or mixture); the rock-fluid system under study is closed (undrained); the pore fluid does not interact with the solid in a way that would soften or harden the frame.

The Gassmann's equation is free of assumptions about pore geometry. However, if multiple pore types are presented in the rock, more complex models should be considered (Berryman and Milton, 1991). In this thesis, I adopt a simple application of the Gassmann's equation, and assume that all model assumptions described before are met.

P-wave velocities, V_P, are affected by porosity, pore geometry and fluid content, mineralogy, effective stress, cementation, and fractures (McCormack et al., 1984). Thus, any of these properties play a role in the observed variation of V_P with depth. If the fluid content effect can be isolated from the other properties, the fluid substitution method can be applied in a very reliable way, and the Gassmann's equation can be used to evaluate the response of V_P to different fluids. In Chapter 3, further discussion and results will be presented about this procedure.

Chapter 2

Reservoir volume estimation and confidence

2.1 The volumetric method

As discussed in Section 1.7, in the early stages of the development of a hydrocarbon field the volumetric method is an important tool used by the oil industry for estimation of petroleum resources. The volumetric method makes use of the volumetric equation, which is given by (Murtha and Ross, 2009)

$$OOIP = \frac{A \cdot h \cdot \phi \cdot (1 - S_{iw})}{B_{oi}} = \frac{GRV \cdot N/G \cdot \phi \cdot (1 - S_{iw})}{B_{oi}}, \tag{2.1}$$

where OOIP is the *oil originally in place*, A is the reservoir area, h is the net pay thickness, ϕ is the porosity, S_{iw} is the initial water saturation, B_{oi} is the initial formation volume factor, GRV is the gross rock volume, and N/G is the net-to-gross

ratio. The terms included in the numerator of the right side of Equation 2.1 define the hydrocarbon pore volume (HCPV) associated with a reservoir. Thus, the HCPV is given by

$$HCPV = A \cdot h \cdot \phi \cdot (1 - S_{iw}) = GRV \cdot N/G \cdot \phi \cdot (1 - S_{iw}), \tag{2.2}$$

In order to use Equation 2.2 to calculate the hydrocarbon pore volume, previous estimations of the reservoir's area, net pay thickness, porosity, and initial water saturation must be carried out. In any form of the volumetric equations presented above, the net pay thickness, the porosity, the initial water saturation and the net-to-gross ratio are given by their average values for the specific area or GRV (Murtha and Ross, 2009).

If the depth to the cap rock (one surface) and the depth to the hydrocarbon water contact (another surface) is determined, the GRV is given by the volume that is in between these two surfaces. In the absence of fluid-contact data, the lowest known occurrence of hydrocarbons generally controls the proved limit (Demirmen, 2007).

The geometry of the cap rock of a hydrocarbon reservoir is never very well defined, thus the depth and lateral location of the spill point (the structurally lowest point in a hydrocarbon trap that can retain hydrocarbons) are uncertain (Abrahamsen et al. 1998). Another origin for the uncertainty in GRV is the time-to-depth conversion in seismic observations, as well as possible dips of the top of the formation (PRMS-AD, 2011). In general, the uncertainty in the GRV, or in the Area, is the largest among the source parameters used in the estimation of reserves (Heiberg and Swinkels 2001, Abrahamsen et al. 1998, PRMS-AD, 2011). Geostatistical methods can be used to preserve spatial distribution information and incorporate it in subsequent reservoir

simulation applications (PRMS, 2007). Thus, geostatistical analysis may improve estimates of the range of recoverable quantities.

The uncertainty associated with the rock properties originates from the variability in the rock (PRMS-AD, 2011). It is determined from different techniques (e.g., petrophysical evaluation, core measurements, seismic response). For fluid properties, a few well-chosen samples may provide a representative selection of the fluids (PRMS-AD, 2011), although sometimes gradients in fluid composition are observed.

2.1.1 Deterministic versus Probabilistic methods

As discussed in the PRMS-AD (2011), the range of uncertainty of recoverable and/or potentially recoverable volumes reflects a range of estimated potentially recoverable volumes. This range of uncertainty may be represented either in deterministic scenarios or by a probabilistic distribution, and it represents the confidence in our volume prediction.

When using the deterministic method (deterministic scenarios), the resources typically should be classified as representing low, best (which represents the most realistic assessment of recoverable quantities), and high estimates, where these estimates are based on *qualitative* assessments of relative uncertainty using consistent interpretation (GEPRR, 2001). Typically in the deterministic method, the first goal is to make a best estimate of the recoverable volume. After this, estimates of the upside and downside case of recoverable volumes are made. These three scenarios together allow a estimation of the range of uncertainty in the best estimate. One advantage of this way to estimate the range of uncertainty in the recoverable volume is that this

approach allows that each assumption adopted can be identified specifically (e.g., a particular value of the water saturation was used for the best estimate scenario). However, this range of uncertainty in the best estimate does not allow a direct quantitative association with a numerical probability, only an uncertainty associated with the adopted scenario.

On the other hand, probabilistic methods naturally allow the representation of the range of uncertainty in terms of percentages. Where probabilistic methods are used, the probabilities associated with the low, best, and high case scenarios should be consistent with those values appropriate for the equivalent category of resources (GEPRR, 2001). For instance, in the P90 estimation range there should be at least a 90% chance (hence, P90) that the actually recovered volume will equal or exceed the low estimate scenario. In the same way, in the P10 estimation range one should concludes that there should be at least a 10% of chance that the actually recovered volume will equal or exceed the high estimate scenario. Common industry practice is to use the median (P50) as the best technical estimate for a single reservoir/zone (PRMS-AD, 2011). P50 gives the quantity for which there is a 50% probability that the quantities actually recovered will equal or exceed the estimate (PRMS-AD, 2011). In this thesis, I propose to investigate the use of the hydrocarbon pore volume equation in the estimation of hydrocarbon volumes, using the uncertainty analysis as the main tool. From this approach, probabilities can be associated with the HCPV predicted.

Summarizing, the calculation of the volumetric for a hydrocarbon field involves the combination of a number of input parameters (as presented in Equations 2.1 and refhpv), each of these has a range of uncertainty in its estimation. This uncertainty

in the input parameters arises from the inaccuracy in the measured data, plus the uncertainty as to what the values are for the parts of the field for which there are no measurements. The uncertainty associated with each parameter may be expressed in terms of a probability density function (section 1.6.3), and these can be combined to create a probability density function for OOIP and HCPV. In the description of range of uncertainties it is common to use CDF curves, in which the hydrocarbon volumes are associated with cumulative probabilities (Avseth et al., 2005).

2.1.2 Reserves and resources

Petroleum classification systems play an important role in the petroleum industry. Reserves are defined in the PRMS-AD (2011) as "those quantities of petroleum anticipated to be commercially recoverable by application of development projects to known accumulations from a given date forward under defined conditions. Reserves must further satisfy four criteria: They must be discovered, recoverable, commercial, and remaining (as of a given date) based on the development project(s) applied". On the other hand, resources are defined in the PRMS-AD (2011) as encompassing "all quantities of petroleum (recoverable and unrecoverable) naturally occurring on or within the Earths crust, discovered and undiscovered, plus those quantities already produced". In addition, the resource classification can be subdivided in two groups: contingent resources and prospective resources.

Contingent resources are defined in the PRMS-AD (2011) as "those quantities of petroleum estimated, as of a given date, to be potentially recoverable from known accumulations by application of development projects but which are not currently

considered to be commercially recoverable due to one or more contingencies. Contingent resources are a class of discovered recoverable resources.". On the other hand, prospective resources are defined in the PRMS-AD (2011) as "those quantities of petroleum which are estimated, as of a given date, to be potentially recoverable from undiscovered accumulations.".

The hydrocarbon volumes calculated in this thesis should then be classified as a resource, because, for instance, no economic evaluation was performed in any step applied in their calculation (neither considered later). Thus, the criteria associated with reserves can not be satisfied in this case. Good discussions about economic/commercial evaluation of hydrocarbon reserves are available in Rose (2001) and Bratvold and Begg (2008).

Figure 2.1 shows the resource classification framework as presented in the PRMS-AD (2011). The Blackfoot reservoir is a producing oilfield, so if a commercial evaluation of the field was performed or even available, any estimated OOIP quantity would be classified as a reserve. However, as previously discussed, this commercial evaluation is not available for the Blackfoot reservoir. Thus, the OOIP quantity should be classified as a contingent resource, because the quantities of petroleum in the Blackfoot reservoir are estimated from discovered accumulations.

The two axis PRMS system described in Figure 2.1 also considers the range of uncertainty associated with some reserve/resource quantity. If the total petroleum initially in-place is classified as a reserve, this quantity can be classified as 1P (proved), 2P (proved plus probable), and 3P (proved plus probable plus possible) reserves. The equivalent categories for projects with contingent resources are 1C, 2C, and 3C, while

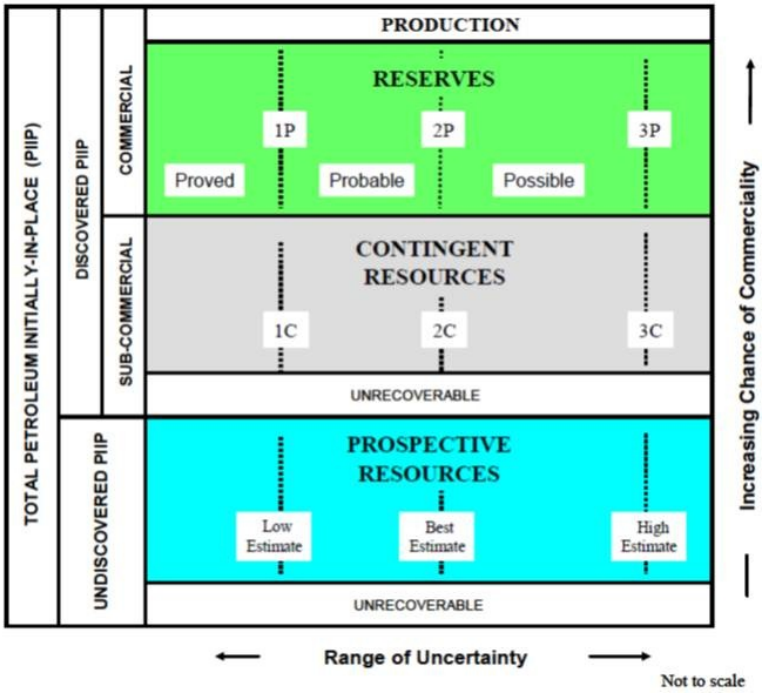

Figure 2.1: The two axis PRMS system: resources classification framework.

the terms low estimate, best estimate, and high estimate are used for prospective resources.

The quantities calculated in the next sections for the Blackfoot reservoir, the HCPV values, are related to the OOIP quantity by the initial oil volume factor B_{oi} (which is unknown, but it is numerically constant in terms of the probabilities associated with HCPV discussed later). Thus, unless the estimation of B_{oi}, the values of P90, P50, and P10 estimated in the next sections for the Blackfoot reservoir should be understood as 1C (proved), 2C (proved plus probable), and 3C (proved plus probable plus possible) contingent resources, respectively.

2.2 Geostatistic analysis

Geostatistical modeling makes use of statistical methods to describe mathematically the variability within any given reservoir unit or pool (GEPRR, 2001). Geostatistical analysis adds spatial correlation to the interpretation process, as well as adds small scale variability which is hard to identify from seismic only because of their limited resolution. Geostatistic methods can be incorporated in different stages of a developing hydrocarbon reservoir, such in defining horizons and estimating reservoir structures, as well as in the seismic inversion itself.

When applying the geostatistical method, the geoscientist depends on the quality of the data as well as of the interpretation procedure adopted to characterize some geological structure. Thus, to use the geostatistical results we have to keep in mind that them are dependent on the amount of data available, the technical evaluation of the input data, and the statistical algorithm used in the modeling (GEPRR, 2001). In fact, the value of the geostatistical analysis depends on the ability to synthesize all available knowledge and data.

One of the main uses of geostatistic analysis is related to hydrocarbon volume estimation for a given area. The hydrocarbon volume estimation requires the interpretation and input of data from different sources (seismic, well logs, well cores), each of them has an inherent uncertainty. Volumetrically, seismic data represents the most comprehensive data available from the subsurface (GEPRR, 2001). However, as discussed in Chapter 1, the reliability of the seismic interpretation depends on the quality of the seismic response and the pick of a given horizon. In addition, the time-to-depth conversion depends on mathematical models that relate velocity

and time to depth (PRMS-AD, 2011). These uncertainties are then inherited by top structure maps, which are used together with hydrocarbon contacts to delineate and characterize a hydrocarbon pool or field. Another source of uncertainty is the scale related to each geophysical data available to the interpretation process. Information provided by well logs, like porosity and water saturation, are from a very different scale compared to the volumes as viewed by the seismic data. Attempts to address this last kind of uncertainty, shows that the uncertainty associated with upscaling procedures in net-to-gross estimations are less than 10% in good quality reservoir, and about 50% in poorer quality reservoir (Ringrose, 2007).

In the case of the Blackfoot reservoir study made by Todorov (2000), and used in part in this thesis, geostatistic analysis was used to obtain the properties distribution maps discussed in the next sections. Specifically, Todorov used the cokriging technique to integrate the 3C-3D seismic interpretation with the well log data and to add spatial correlation between these properties to the geophysical interpretation. In addition, geostatistic analysis allows tests to estimate the error in the accuracy of the results. This last point will be discussed in the next section.

2.3 Estimating the reservoir volume confidence – the Blackfoot reservoir

As already discussed in Section 2.1, to calculate the hydrocarbon pore volume (HCPV) estimations of the thickness and extension of the reservoir rock, as well as the quality of the reservoir rock, its porosity and its oil saturation have to me estimated. In

addition, to add value for the information of the HCPV estimation, uncertainty analysis should be carried out, thus resulting in a likelihood associated with the HCPV predicted.

In this section, first I discuss the process that was applied by Todorov (2000) to estimate a single HCPV value. Then, I discuss ways to estimate the uncertainty in each parameter used by Todorov to calculate his HCPV value. Next, use two different methods to associate a probability with a HCPV estimation. The first method is based in the Taylor expansion, and allows the association of the HCPV value predicted by Todorov (2000) with probabilities from errors associated with the parameters used to estimate HCPV. The second method is a Monte Carlo simulation, a primarily probabilistic one. The results of both methods are compared, so that both methodologies can be evaluated upon their results for the Blackfoot reservoir.

The results presented in this chapter were presented as a study case at the 2011 SEG Annual Meeting in the workshop *Use of Seismic Technology in Petroleum Resources Estimation and Classification*, which was sponsored by the SEG Gas and Oil Reserve Committee.

2.3.1 Uncertainty in thickness and percentage of sand

Different kinds of thicknesses can be associated with a hydrocarbon reservoir. The gross thickness is defined as the total thickness of an evaluation interval, typically between the top of the reservoir and the oil/water contact. Beyond the gross thickness, there are three types of net thickness: net sand, net reservoir, and net pay thickness (Worthington, 2009). The differences used among these three types of thickness is,

in general, the cut-offs applied to the gross thickness.

Of these three last types of thicknesses, Net Pay is a key parameter in the volumetric estimation of hydrocarbon resources, because it identifies those penetrated geological sections that have sufficient reservoir quality and interstitial hydrocarbon volume to function as significant producing intervals (Worthington, 2009). However, as discussed also by Worthington, "there is no universal definition of Net Pay, there is no general acceptance of its role in integrated reservoir studies, there is no recognized method for evaluating it, and there are disparate views on how to make use of it."

With the considerations of the paragraph above in mind, it is important to define clearly what is each one of the thicknesses associated with reservoir evaluation. Net sand can be understood as a net potential reservoir, because it describes the thickness interval which contains rocks that are associated with good reservoirs. In a clastic geological environment, the net sand thickness is a subinterval of the gross thickness, and a a cut-off applied in the gamma-ray log (an estimator for the volume of shale) is in general adopted to characterize the net sand interval. The net reservoir thickness contain rocks that have been identified as having capability to store fluids and allow them to flow. In general, a cut-off applied in the porosity log is used to define the net reservoir thickness from the net sand thickness, and then net reservoir thickness is a subinterval of the net sand thickness. The net pay thickness comprises the net reservoir containing a significant volume of hydrocarbons in place. It is then a subinterval of the net reservoir thickness. The net pay thickness takes into account the hydrocarbon saturation associated with the reservoir and if the hydrocarbon can be produced at economic rates. Traditionally, a water saturation cut-off is used to define the net pay thickness. Figure 2.2 illustrates the differences between net sand,

net reservoir, and net pay thickness.

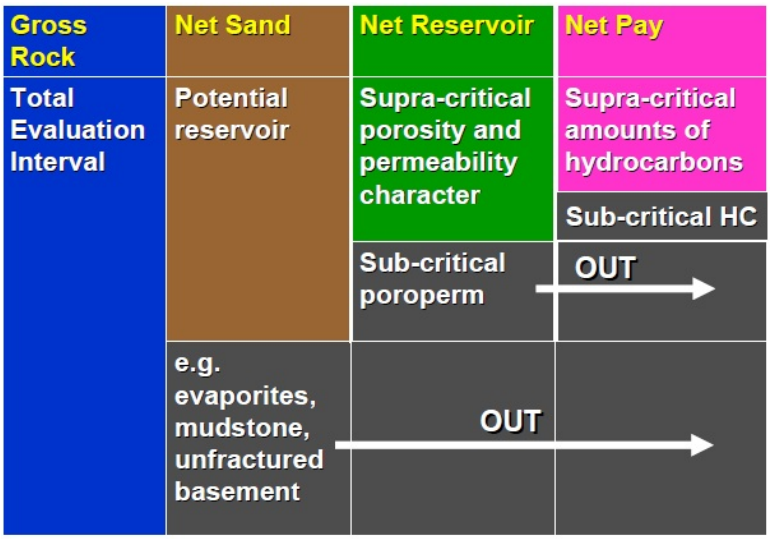

Figure 2.2: Interrelationship of formation thicknesses (from Worthington, 2009).

Next, a discussion about the estimation of the percentage of sand and of thickness distribution maps will be discussed, as well as a procedure to estimate their uncertainty.

SAND PERCENTAGE DISTRIBUTION MAP

The analysis of the isochron maps from multicomponent data allows the computation of the V_P/V_S (Todorov, 2000), which is given by

$$\frac{V_P}{V_S} = 2\,\frac{t_{PS}}{t_{PP}} - 1 \tag{2.3}$$

where t_{PP} is the P-P isochron and t_{P-S} is the P-S isochron.

In the case of the Blackfoot reservoir, the sand/shale distribution mapping was carried out by Todorov (2000) using an observable correlation between the Gamma-ray index (GRI) obtained from the gamma-ray log (GR) and the V_P/V_S value obtained from the 3C-3D seismic data (see Figure 2.3). As discussed by Potter, Miller, and

Margrave (1996), clay which is incorporated into the rock matrix will make the rock less able to resist shearing forces, resulting in an overall increase in the V_P/V_S with the shaliness in the Blackfoot area. This result supports an expected correlation between the V_P/V_S ratio and the GRI, and was used by Todorov (2000) to map the distribution of the sand content in the reservoir.

As discussed by Asquith and Krygowski (2004), the GRI is in first order a good indicator of the shale fractional volume V_{sh} in sandstone reservoirs. Then, the sand fractional volume V_{ss} in the same reservoir can be calculated using that $V_{ss} = 1 - V_{sh}$. Thus, the information contained in the GR well log can be spread out using geostatistic analysis and the extensive spatially information associated with the 3C-3D seismic data. In this process, Todorov (2000) used a cokriging technique to carry out the geostatistic analysis. Applying the cokriging method, Todorov spread the information of the GRI to the whole area, using the V_P/V_S as a vector, then generating a realization of cokriging GRI distribution map. From the GRI distribution map, Todorov obtained a realization for the sand percentage distribution map. Ten realizations were generated using this procedure, allowing a meaningful sand percentage distribution map for the Blackfoot reservoir area. Figure 2.4 shows one of the cokriging GRI realizations.

The confidence of the cokriging GRI result was evaluated by Todorov using cross-validation tests. Specifically, Todorov carried out *blind well* procedures for each one of the available wells (i.e., 10 wells), obtaining the absolute error associated with the cokriging GRI prediction for each well location. Figure 2.4 shows also the results for the cross validation test performed by Todorov. After the verification of the cross validation test, which validated the cokriging result, a sand percentage distribution

map was generated from the 10 realizations of the cokriging GRI result. This sand percentage map was then used by Todorov together with other geophysical data (described in this chapter) to carry out a single deterministic estimation for HCPV. To obtain an estimate of the final net sand distribution map from the final percentage of sand distribution map, in a way consistent to Worthington (2009), a cut-off in the percentage of sand values have to be applied to the latter.

I have used the results of the cross validation test as described above to evaluate the uncertainty in the sand distribution map used by Todorov to estimate HCPV. To do this, I realize that the cross validation test allow a measure of the accuracy of the cokriging result. In fact, for each well location there are two measurements: the well log value and the simulated value using cokriging. Both values can be compared, allowing an estimation of the error in the cokriging prediction. Using the 10 *blind well* tests, I obtained from the absolute errors published by Todorov 10 estimates of the error in the cokriging procedure. Figure 2.5 shows a histogram of the distribution of the errors obtained from this procedure. Taking the standard deviation of these errors, I estimated an overall uncertainty of 10% associated with the sand percentage distribution map provided by Todorov (2000).

THICKNESS DISTRIBUTION MAP AND ITS UNCERTAINTY

To obtain a thickness distribution, Todorov (2000) used geostatistic to integrate a seismic isochron map derived from the seismic survey and the corresponding thickness estimated from the well data. In this methodology, the thickness is calculated in all well locations (in this case, 11 wells). A good correlation was observed by Todorov between the isochron values obtained from seismic and the thickness calculated at

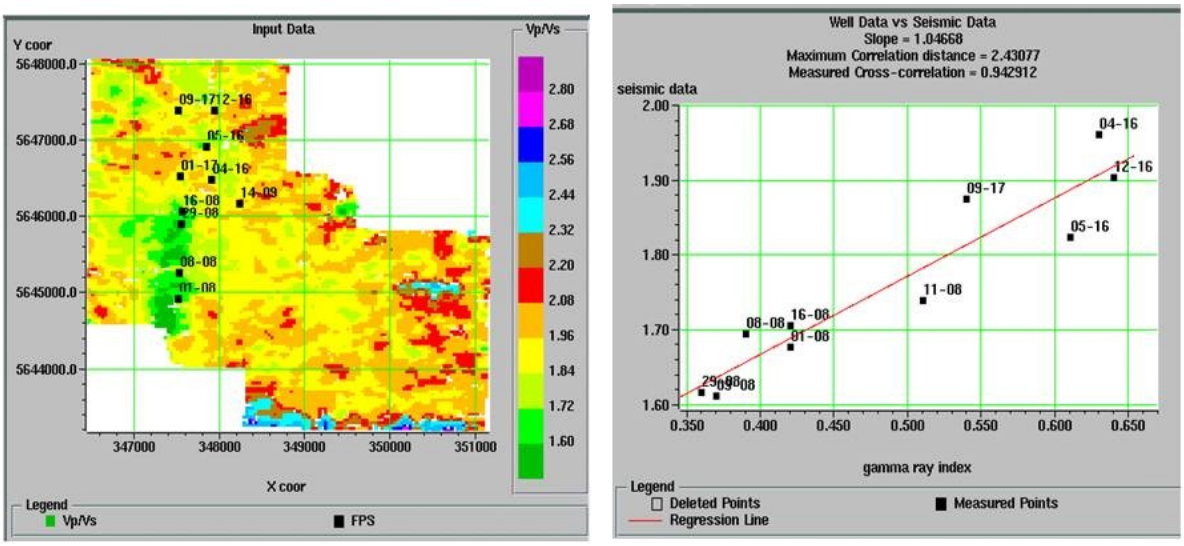

Figure 2.3: Two results presented in Todorov and Stewart (1997). *Left*: Vp/Vs ratio distribution as obtained from the 3C-3D seismic data. *Right*: Vp/Vs (from seismic) versus Gamma-ray (from well logs). A good correlation between the two parameters can be observed.

the well locations. This correlation was then used to spread the information of the thickness values in the well locations for the whole area, using a cokriging method. From this procedure, Todorov obtained a realization for the thickness distribution map. In total, ten realizations were carried out, and the final thickness distribution map was obtained from them. This final thickness distribution map was then used in the estimation of the HCPV value by Todorov.

Cross validation tests were carried out in the same fashion described for the sand percentage map, in order to evaluate the thickness distribution maps obtained from the cokriging method. Thus, a blind well procedure was applied for each one of the 11 wells used to estimate the thickness distribution map. Each one of these blind well tests allowed an estimate of the error associated with the generated thickness map. Taking the standard deviation of these errors, I estimated an overall uncertainty of 6%

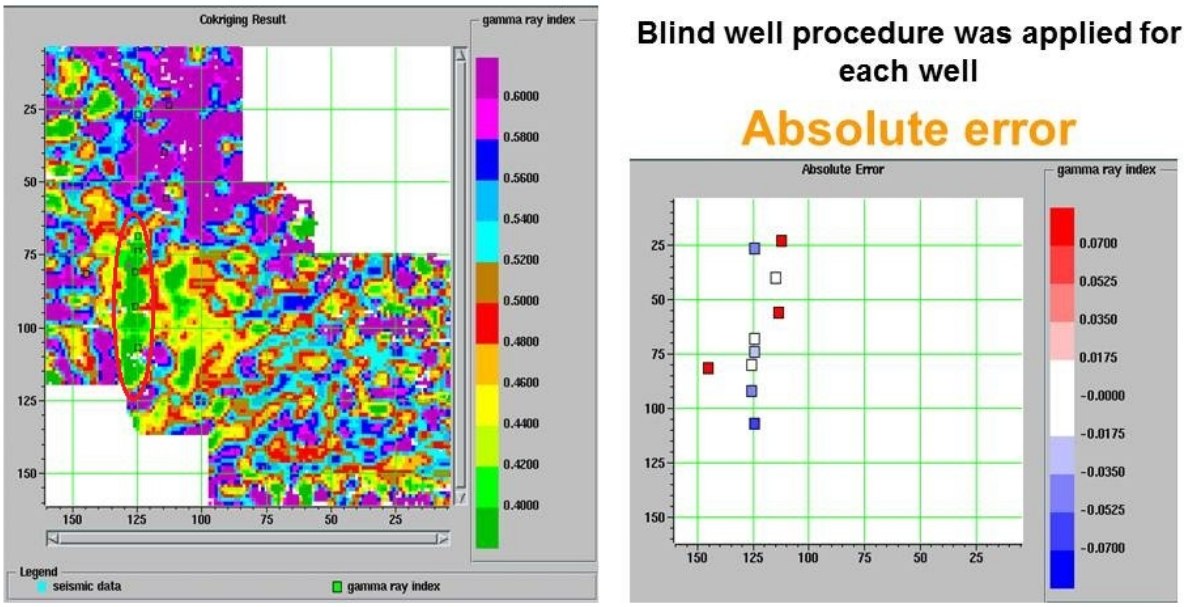

Figure 2.4: Two results presented in Todorov (2000). *Left*: The Gamma ray index after cokriging. The Blackfoot reservoir is inside the encircled red line. *Right*: result of the cross validation test for the gamma ray index cokriging.

associated with the sand percentage distribution map provided by Todorov (2000).

2.3.2 Uncertainty in the porosity

As discussed in Jahn et al. (1998), reservoir porosity can be measured using core samples or from logs. Logging is the most common method employed, since the core coverage is not complete (Jahn et al., 1998). When the core porosities are available, the results obtained from both methodologies should be compared to each other. The main tool for measuring porosity is the formation density log, although other logging tools can be used, such as the neutron and sonic tools. Section 3.2 discuss some calculations associated with the porosity property.

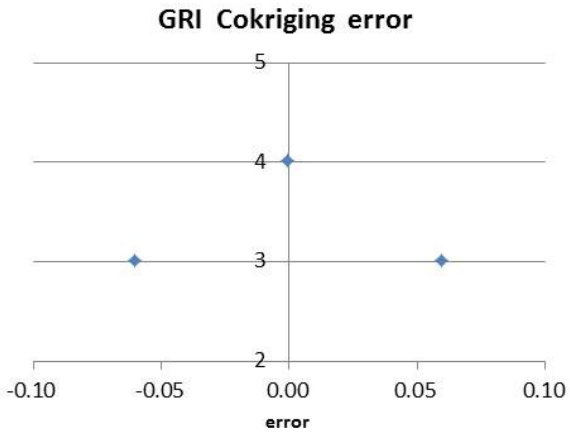

Figure 2.5: Histogram representing the error distribution for the gamma-ray index, as obtained using the cross validation test (see text for details).

In the case of the Blackfoot reservoir, a porosity distribution map was also generated by Todorov (2000) using the 3C-3D seismic data. This porosity map was generated using a method for deducing rock properties based on the integration of seismic attributes and measured well log curves. The method used was a neural network method.

This integration was made first by looking for a relationship between the rock properties and some seismic attribute from the 3C-3D seismic data, at the well locations. When a suitable relationship was determined, it can be applied to the seismic volume, and thus a predicted log property volume was then generated. To obtain an estimate of the final net reservoir distribution map from the final percentage of sand distribution map, in a way consistent to Worthington (2009), a cut-off in the porosity values should be applied to the latter.

To apply a quality control test in these calculations, Todorov (2000) tested the

reliability of the relationship used to map the porosity distribution carrying out cross-validation tests. The results of the porosity map were then compared to the values observed in the well locations. This comparison allowed to estimate the error associated with the porosity predicted by the neural network method. The overall uncertainty associated with the differences between both values for porosity, using the methodology applied to the thickness and percentage of sand distribution maps, was estimated in 11%.

2.3.3 Uncertainty in the oil saturation

The oil saturation S_{oil} is obtained indirectly, from the water saturation S_{water}, assuming that

$$S_{oil} = 1 - S_{water}, \tag{2.4}$$

where is implicit when using this equation that the reservoir has only two fluid phases (oil and water).

The water saturation is calculated from well log data, in general using the Archie's equation (Asquith and Krygowski, 2004). The process of its determination includes the use of information available in the resistivities and porosities from well logs, from the drilling mud properties and from the information about the geothermal gradient in the neighborhood of the well. Different from the cases of the other parameters involved in the prediction of the oil column, the saturation property can not be easily spread in a constrained way using the seismic data, since the seismic data does not correlated in general in a suitable way to the saturation information of the reservoir.

In his studied of the Blackfoot reservoir, Todorov (2000) adopted a constant value for the water saturation, and thus for the oil saturation. An oil saturation $S_{oil} = 0.75$ in the whole reservoir ($S_{water} = 0.25$) was made available from producing wells in the reservoir, and this value was used in the calculations for the oil column carried out by Todorov (2000). To obtain an estimate of the final net pay distribution map in a way consistent to Worthington (2009), a cut-off in the water saturation values should be applied to the data. As no water saturation distribution map was generated by Todorov (2000), the author in fact used the net reservoir distribution map as an approximation for the net pay distribution map (because he adopted a constant value $S_w = 0.25$ to the whole reservoir). Thus, some overestimation of the HCPV values can be expected from the Todorov estimate.

The uncertainty in the S_{water} parameter was estimated from the evaluation of the standard deviation associated with the variation in the values of S_{water} calculated for three wells in the Blackfoot reservoir. Thus, I use the dispersion in the water saturation values associated with the reservoir interval in depth to calculate the coefficient of variation of S_{water} in the reservoir. The S_{oil} saturation uncertainty was then obtained from the uncertainty in S_{water}, resulting in a fractional uncertainty of 10% Although this calculation is not very well constrained, it allows a estimation for the uncertainty in the hydrocarbon saturation by associating the S_{oil} with variations presented in the observed values.

2.3.4 Uncertainty in the area of the reservoir

The reservoir's area delimits the extension of the hydrocarbon accumulation. Together with the interval thickness, the area allows the estimation of the gross rock volume (GRV = area × interval thickness). Two different methodologies are in general used to estimate the reservoir's area: the area-depth method and the area-thickness method. Next, I discuss briefly both methods as presented by Jahn et al. (1998).

In the area-depth method, the area is estimated in different depth intervals (in general going from the top of reservoir to its base). In any value of depth interval, a value of area is associated. Doing a plot of area versus depth, and connecting the measured points of the area-depth pairs, a curve describing the area-depth relationship for the top of the reservoir can be derived. If the gross thickness can be estimated from wells (an average value for the gross thickness), a second curve representing the area can be derived in the area-depth plot for the base of the reservoir. The area between the two curves is equal the volume of rock between the two markers. With a estimation for the oil-water contact (OWC), the area above the OWC is the oil bearing GRV. A limitation of this method is that the gross thickness is constant across the whole field (Jahn et al., 1998). Figure 2.6 illustrates the area-depth method (from Jahn et al., 1998).

The area-thickness method is used in general when the assumption of a constant thickness or a linear trend in the thickness across the field is not valid anymore. In this case a more complex methodology has to be used. In the case presented as an example by Jahn et al., the hydrocarbon volume is constrained by the structural feature of the field and the distribution of reservoir rock. Figure 2.7, from Jahn et al.

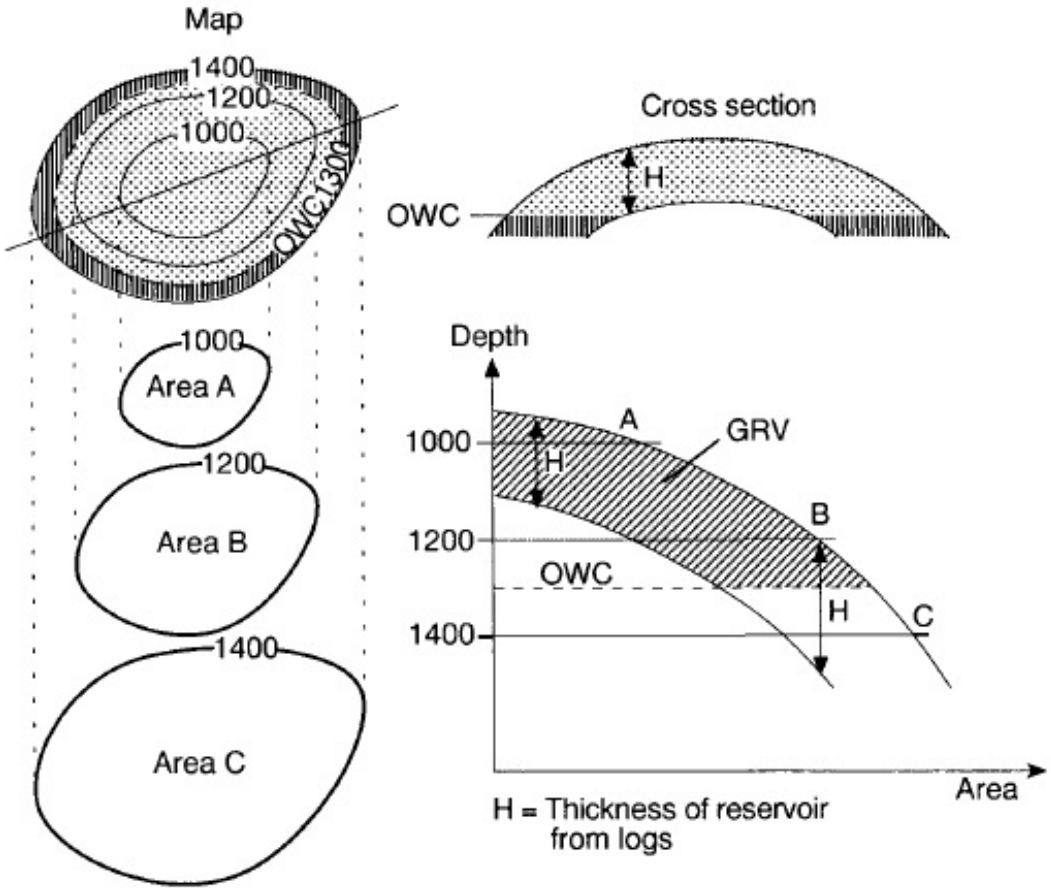

Figure 2.6: The area-depth method, from Jahn et al. (1998).

(1998), is useful to illustrate this methodology.

In the top/left of Figure 2.7, the structure map related to a hypothetical reservoir is shown (labeled 1), and in the top/right its net sand map (labeled 2). In the bottom/right, the net oil sand map is shown (labeled 3), and in the bottom/left, the net oil sand volume is shown (labeled 4). In the example discussed by Jahn et al. (1998), the reservoir presents a channel sand geometry (thus the thickness is not constant along the reservoir). The net sand map presented in Figure 2.7 represents the thickness associated with the channel sand adopted in the example considered by

Jahn et al. The area associated with the reservoir, and then its gross rock volume, has to take into account this constraint of the channel sand geometry together with the structural map which contains the fluid contacts and the top of the reservoir information. Thus, the structural map and the net sand map are used to obtain the net oil sand map, which is also shown in Figure 2.7. The final result is obtained estimating the thickness at different contours in the net oil sand map, and it is shown with the label 4 in Figure 2.7.

In his work about the Blackfoot reservoir, Todorov (2000) associated the extension of the reservoir with the area related to a oil column higher than 3 m (see Figure 2.8). Adopting the result from Todorov, I evaluate the uncertainty in the reservoir's area including in the area value the contours close to the contour associated with an oil column of 3m. The uncertainty in the area estimated in this way was associated with an uncertainty value of 30% of the reservoir's area.

2.4 HCPV and its likelihood

As discussed in the previous sections, I used the cross-validation procedure applied to validate predicted values obtained using geostatistical analysis (thickness and percentage of sand distributions) and the neural network method (porosity distribution) as a way to estimate the overall uncertainty in the results of these distributions. These overall uncertainties (based on the coefficient of variation; Coleman and Steele, 2009) were approximately 6% for the thickness, 10% for the percentage of sand, and 11% for the porosity. I also used the well log data available from the Blackfoot reservoir

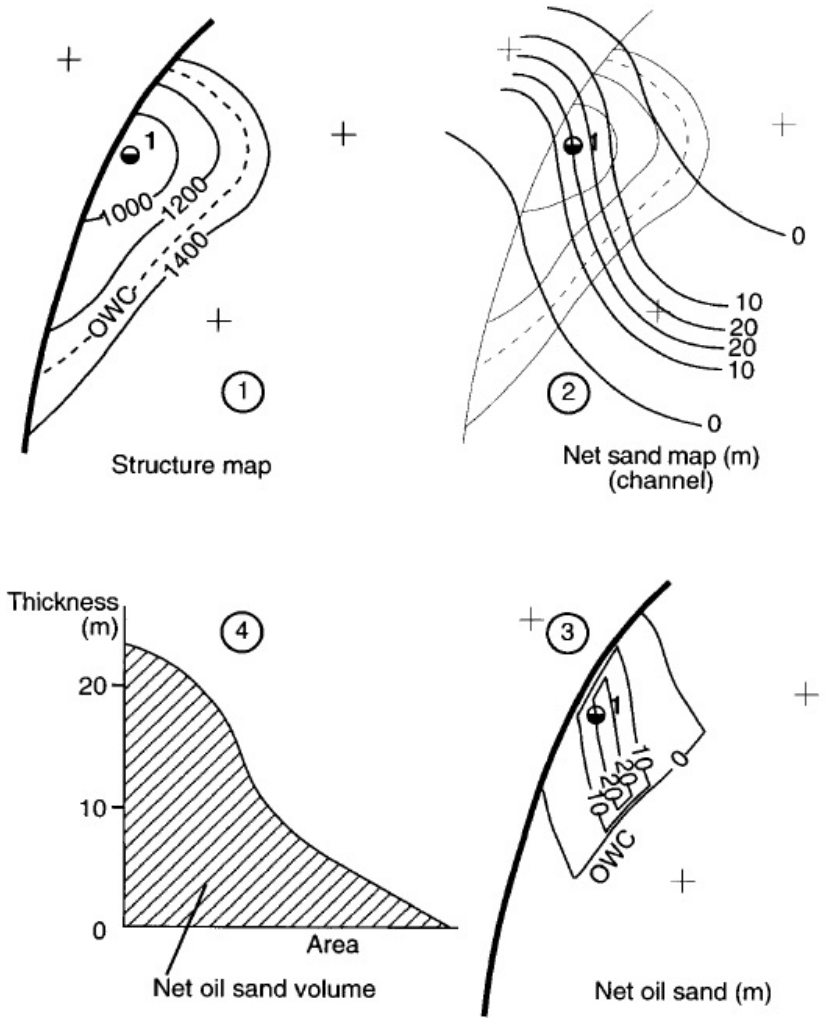

Figure 2.7: The area-thickness method, from Jahn et al. (1998).

to estimate the uncertainty in the water saturation which allowed me to estimate the oil saturation uncertainty through the coefficient of variation. The oil saturation uncertainty was estimated to be 10%. I used the information of the oil column distribution (Figure 2.8) as presented in Todorov (2000) to estimate the uncertainty in the reservoir area, which was about 30%.

I then used two different approaches to evaluate the overall uncertainty in the

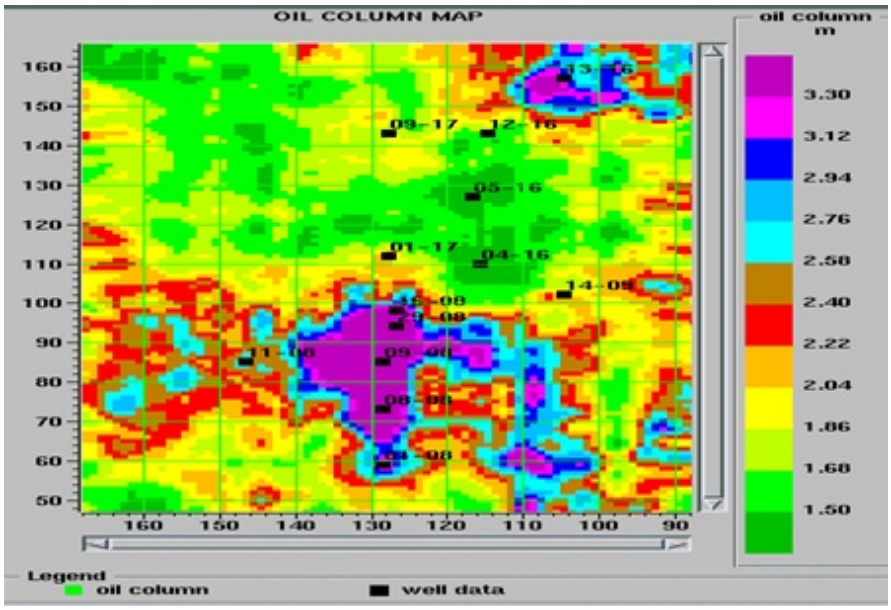

Figure 2.8: The oil column distribution as in Todorov (2000).

hydrocarbon pore volume (HCPV) estimation from the uncertainties estimated previously, assuming in both approaches that the parameters used to calculate the hydrocarbon pore volume were not correlated to each other.

2.4.1 Taylor expansion approach

The first approach was based on the Taylor expansion (Coleman and Steele, 2009) and it allowed the calculation of the uncertainty in HCPV using the expression below:

$$\left(\frac{\sigma_{HCPV}}{HCPV}\right)^2 = \left(\frac{\sigma_{thickness}}{thickness}\right)^2 + \left(\frac{\sigma_{\%sand}}{\%sand}\right)^2 + \left(\frac{\sigma_{\phi}}{\phi}\right)^2 + \left(\frac{\sigma_{S_{oil}}}{S_{oil}}\right)^2 + \left(\frac{\sigma_{Area}}{Area}\right)^2 \quad (2.5)$$

where %sand is the percentage of sand, ϕ is the porosity, and S_{oil} is the oil saturation. The values in the denominators in the equation 1 are the average values for each property in the Blackfoot reservoir, so that each term presented in Equation 2.5 is the coefficient of variation (CV = mean/standard deviation) specific for each parameter.

The coefficient of variation, CV, is a dimensionless quantity and is used in general to compare uncertainty in properties measured using different units/scales (Deutsch, 2002; Miller and Kahn, 1962).

Equation 2.5 assumes that the parameters associated with the volumetric calculation are independent to each other. In general this is not the case, since dependencies between parameters often exist and must be represented in the probabilistic estimation of hydrocarbon volumes (PRMS-AD, 2011). However, in the specific case of the Blackfoot reservoir, Todorov does not provide any of these dependencies. Thus, it is more appropriate to use the special case where the parameters are independent to each other when discussing the uncertainty in the estimated HCPV value. In the case of considering dependencies in the parameters associated with Equations 2.1 and 2.2, covariance terms related to the dependent parameters should be added to the right side of Equation 2.5 (Coleman and Steele, 2009).

In the approach applied for the Blackfoot reservoir the single deterministic prediction for HCPV carried out by Todorov (2000) was used, assuming that this predicted value represented a best estimate scenario (GEPRR, 2001). After that, the uncertainty in the HCPV prediction using the overall values of the uncertainties obtained previously for each term in the right side of Equation 2.5 was estimated.

Hence, I used the relationship between the probability density function (PDF) and the cumulative distribution function (CDF) already discussed in Section 1.6.2, as well as the estimated uncertainty in the predicted HCPV, calculated using Equation 1, to link a estimated HCPV value with its likelihood (see Figure 2.9). I call this last procedure probability from errors. An interesting point of the methodology used in

this first approach is that it can use the estimation of the uncertainty in the parameters used in deterministic predictions of HCPV to link the best estimate scenario result with probabilities (using probability from errors). Figure 2.9 shows the predicted CDF obtained using the Taylor approach discussed in this section, using the estimate for the uncertainty related to each parameter contained in Equation 2.5, as presented in the previous sections.

Although the PRMS-AD (2011) discuss ways to link deterministic predictions of OOIP with probabilities, the PRMS-AD discuss this procedure as a collection of scenarios which is then translated into a probability curve for OOIP. Thus, the methodology discussed by the PRMS-AD (2011) is not the same of the described previously in this section. A comparison of the HCPV prediction using the method described in this section and the method of collection of scenarios as described in the PRMS-AD (2011) should be object of future research.

In addition, to evaluate the prediction for the CDF associated with the HCPV estimation described in this section, a second approach was carried out in the uncertainty analysis for HCPV, which uses a methodology that is primarily probabilistic. Thus, a Monte Carlo simulation approach was carried out taking into account the same uncertainty values considered in the Taylor expansion methodology. The Monte Carlo simulation approach and its results are discussed in the next section.

2.4.2 Monte Carlo approach

The second approach used to evaluate the uncertainty in the HCPV estimated value was based on the Monte Carlo simulation which allowed a direct link between the

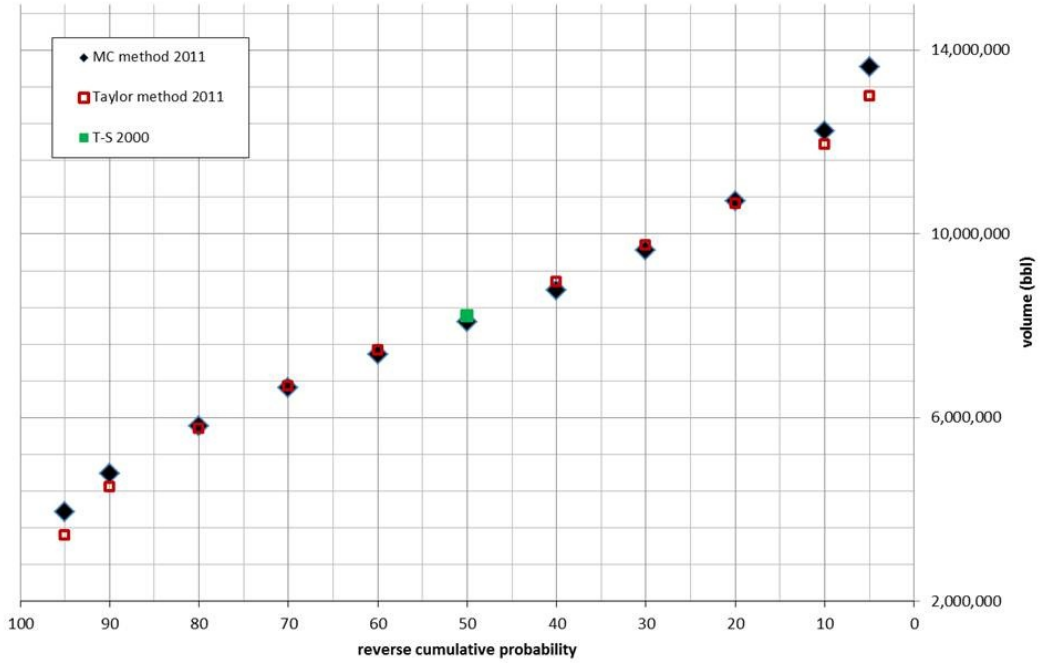

Figure 2.9: Cumulative distribution function for the hydrocarbon pore volume estimation. Hollow square/red: Taylor expansion method. Black/diamond symbol: Monte Carlo approach. Green square: estimate of Todorov and Stewart.

predicted value of HCPV and its likelihood (the Monte Carlo simulation approach is primarily a probabilistic one). Section 1.6.3 presents a brief review about how Monte Carlo simulation works, and Section 3.3.1 discuss briefly the case for a correlated Monte Carlo simulation. A detailed discussion about the use of Monte Carlo simulation can be found in Coleman and Steele (2009).

The parameters used in the Monte Carlo simulation were given by the uncertainty values of the parameters as used in the Taylor expansion method. The PDF for all parameters were adopted as normal distributions. Ten thousand simulations were carried out in the Monte Carlo simulation. This number was selected because it guarantees that the statistical parameters associated with the results obtained from

the Monte Carlo simulation were stable. Figure 2.10 shows the evolution of the estimated standard deviation of the hydrocarbon volume with the number of simulations used in the Monte Carlo simulation. This result was also verified in equivalent results for the mean and the median values obtained from the Monte Carlo simulation. Thus, it can be concluded that increasing the number of simulations does not improve the final estimation. Figure 2.11 shows the result of one realization obtained using the Monte Carlo simulation. The predicted CDF as obtained using the Monte Carlo approach is shown in Figure 2.9.

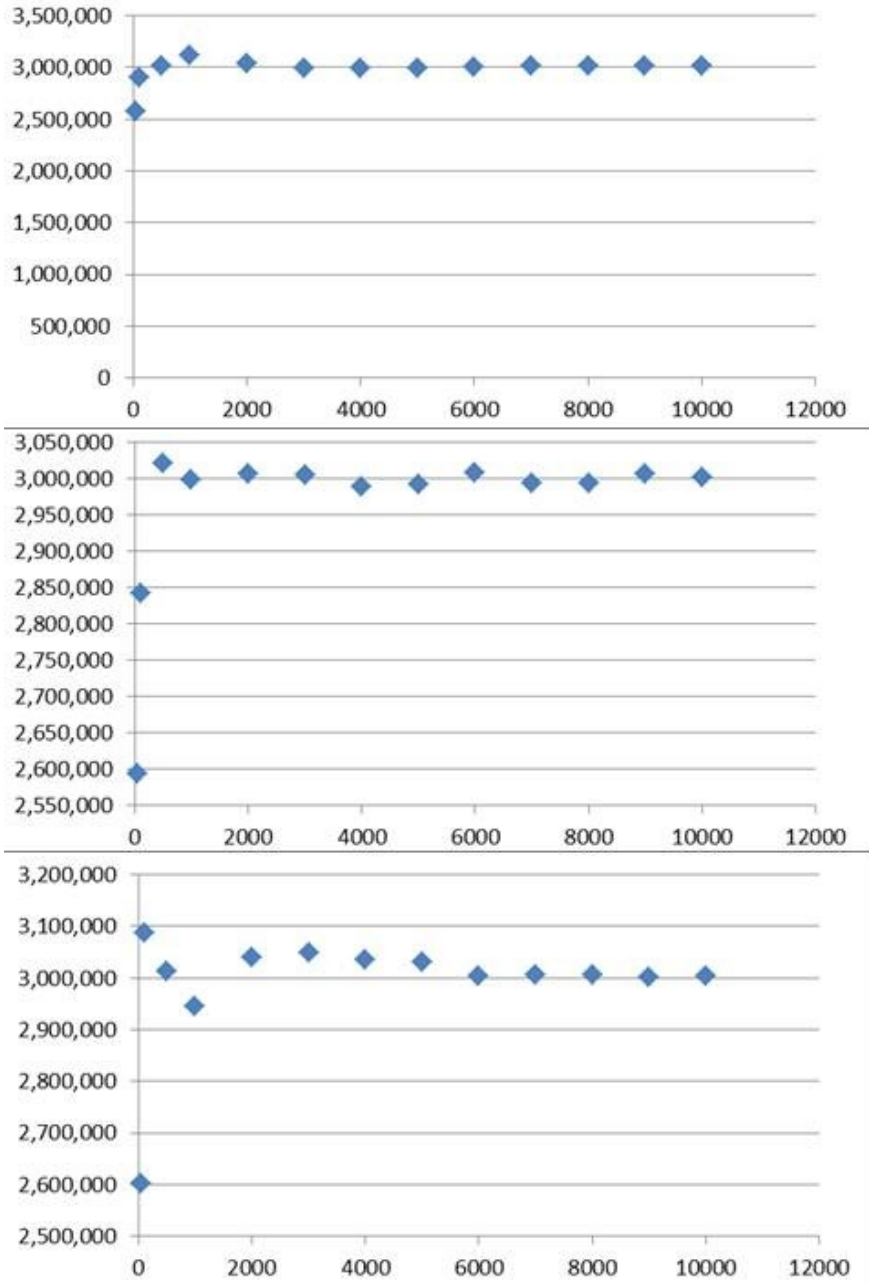

Figure 2.10: Standard deviation of the estimated hydrocarbon volume obtained from the Monte Carlo simulation. When the number of simulations increases (shown in the horizontal axis of the graphics), the value associated with the predicted standard deviation (shown in the vertical axis) becomes stable.

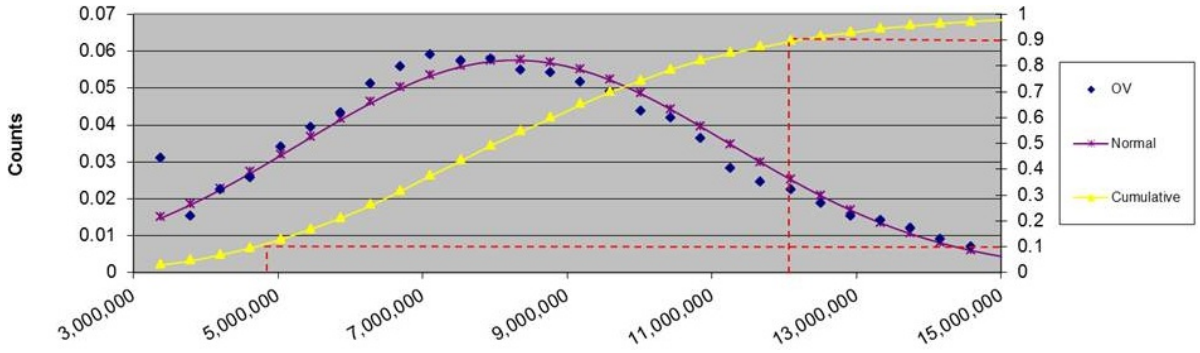

Figure 2.11: Histogram of one realization of the Monte Carlo simulation applied to the volumetric calculation. The left vertical axis scale shows the relative number of simulations associated with each bin of the histogram. The right vertical axis scale shows the value associated with the CDF related to the simulated sample obtained from the Monte Carlo simulation. The blue/dark points show the value associated with the PDF for each bin, and the purple points/line show the equivalent normal distribution which would be obtained using the mean and the standard deviation value of the simulated sample. The yellow/light points/line show the CDF curve associated with the simulated sample.

2.4.3 Comparison of the results

Figure 2.9 shows a CDF plot presenting the results obtained using both methodologies described previously for HCPV of the Blackfoot reservoir. It also shows the predicted HCPV value as calculated by Todorov (2000). From Figure 2.9, it can be seen that both approaches presented compatible hydrocarbon volumes estimations for the Blackfoot pool, with P10$\sim$ 12 MMbbl (there is 10% of chance that this reservoir has more than 12MMbbl), P50$\sim$ 8 MMbbl, and P90$\sim$ 5 MMbbl. A recent accounting (Ken Mitchell, pers. comm., 2011), using the actual amount of oil produced from the Blackfoot pool, suggests an original oil in place of 5.5 MMbbl. In addition, the presence now observed of a gas cap in the Blackfoot reservoir (information not available in the time in which Todorov did his calculations) shows that a initial formation

volume factor different from one should be used to compare the HCPV estimation by Todorov (2000) with the OOIP value (2011). However, the value of the oil initial formation factor is not available.

The two methods used in the precious sections to generate a CDF for the HCPV associated with the Blackfoot reservoir presented compatible results. Between P20 and P80 both methodologies present results that are remarkably similar. When considering the tails of the PDF associated with each method, however, the Taylor expansion approach showed lower HCPV values than the ones predicted by the Monte Carlo simulation approach.

Thus, upon the assumptions adopted in the investigation described in the previous sections, both methodologies can be used without any clear advantage of one methodology over the another. This does not mean that the methodologies used in this investigation are the most correct to be associated with the Blackfoot reservoir. For a conclusion like that to be made, further investigation should be made about any possible dependency associated with the reservoir parameters related to the Blackfoot reservoir (not considered in my calculations).

However, the fact that both methods generated similar results allows an interesting possibility. The Taylor expansion method used standard propagation errors procedures to generate the CDF for HCPV. In fact, it can be seen in Figure 2.9 that there are no predicted HCPV value associated with P50 (the best estimate case) for the Taylor expansion method. This happens because the Taylor method used the deterministic single HCPV value predicted by Todorov (2000). Thus, any deterministic procedure used to estimate a single value for HCPV (a best estimate case) could be

associate to a likelihood of the estimation using probability from errors and Taylor expansion methodology. However, this possibility should include a comprehensive investigation about the CDF curve predicted by the actual oil companies operating a hydrocarbon field (which is out of the scope of an academic investigation) and its comparison with the prediction methodology presented in this thesis.

In addition, further investigation should be made about how the errors in the parameters used to the HCPV estimation can be obtained from the data used in the calculation. A very simple attempt was developed in this thesis, for the thickness error, and it is presented in the next section.

2.5 Seismic error analysis

As discussed in the previous section, the investigation about the possible origin of the uncertainties associated with the parameters used in the calculation of HCPV could be very useful to deal with a deterministic single value for the HCPV estimation. The thickness uncertainty, for example, can be related to the uncertainty in the picking time.

To do this, I used the time picking error equation (Stewart et al., 1984) to estimate the uncertainty associated with the time picking procedure. The time picking error t_e is given by

$$t_e = \frac{1}{f_m \cdot \ log_2 \left[1 + \left(\frac{S}{N}\right)^2\right]} \tag{2.6}$$

where f_m is the maximum frequency in the data, and (S/N) is the signal-to-noise ratio. Figure 2.12 shows the spectral response curves for PP and PS data for the

Blackfoot reservoir (Goodway and Tessman, 2001). Using Equation 2.6, I then applied the information of the seismic data of Blackfoot reservoir in the time picking error equation [$f_{m,PP} \sim$ 100Hz, $(S/N)_{PP} \sim 30$]. I found that the time picking error ($t_e \sim$ 1.2ms; using Vp= 3783m/s, I estimated a depth error of 4.5m) is consistent with the overall uncertainty calculated to the thickness parameter using the cross validation test in the geostatistical method. This result suggests that the time picking error could explain, in this case, the uncertainty in the thickness parameter. However, the value of (S/N) is not very well defined in general. Appendix A presents the mathematical case for the relation between the thickness error and the time picking error.

Another possible way to determine (S/N) is using the Meunier's expression (Meunier, 2011), in which the signal-strength estimate SSE is given by

$$SSE(f) = SS(f)\sqrt{SD \cdot NR \cdot RA},$$

where SSE is an estimator of (S/N) and is a function of frequency, SS is the source strength, SD is the source density (number of SP per surface unit), NR is the number of receivers per SP (source point), and RA is the area of the receiver station. The equation provided by Meunier was derived for use with vibroseis data, which is not the case in the Blackfoot seismic survey. However, Meunier (2011) also provided a relationship between the source-strength SS(f) from vibroseis sources and from explosives. Thus, Meunier (2011) states that experiments have shown that there is an equivalence in these sources in the bandwidth of 5 to 25 Hz, between 1 kg of explosives and one 400-kN vibrator sweeping 1.25 Hz/s.

Using this equivalence, and the parameters for SD, NR, and RA from the acquisition parametrization of the Blackfoot data (Lawton et al., 1996), a SSE about 130 was

obtained. This value obtained for SSE seems large, and in fact the Meunier equation was not applied taking into account the attenuation of the seismic wave between the source and the reflector associated with the time picking event (the source strength SS was considered independent of frequency in the calculation of SSE). Using the estimate for SSE, from Meunier equation, into Equation 2.6 allows a time picking error of 0.8 ms and a depth error of 2.7 m. Further investigation must be made to evaluate the use of the Meunier's expression, which takes into account acquisition parameters, in the interpreted seismic data used in Equation 2.6.

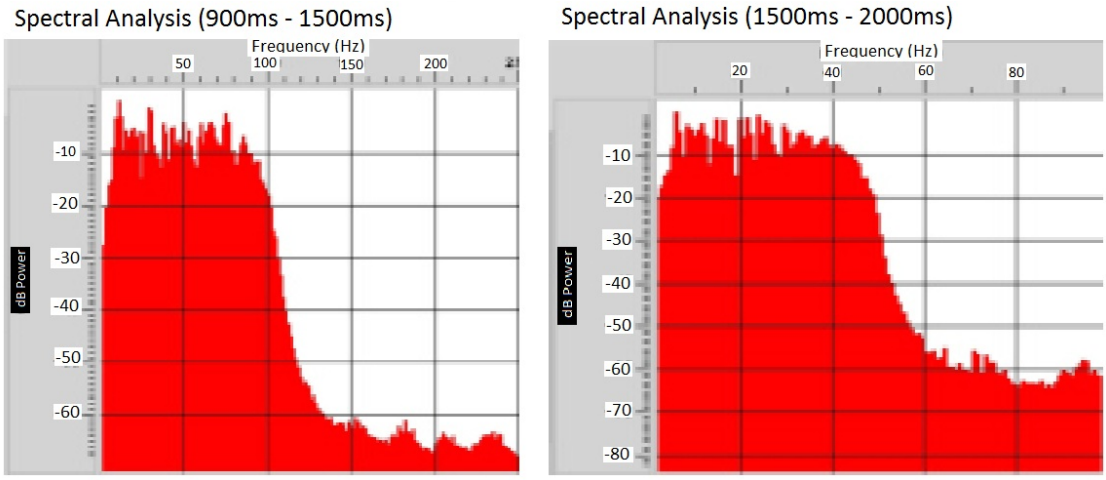

Figure 2.12: Spectral response curve for PP (left) and PS (right) data (from Goodway and Tessman, 2001).

2.6 Ultimate recovery confidence – additional case

An additional case presented by Demirmem (20007) was used to compare both methodologies described in Section 2.4. The application of these methodologies in the framework described previously requires modifications in the equations used in this thesis

to estimate the hydrocarbon volumes. However, these modifications can be easily implemented to match and apply the methodologies described in Section 2.4, and they are described below.

In his work, Demirmem (2007) discussed different methods used in hydrocarbon reserves estimation. Specifically about the volumetric method, his work presented some quantitative results for the reservoir "*KK*", and also the mean and the standard deviation values to each one of the parameters included in the volumetric estimation presented by him. Table 2.1 presents the values provided by Demirmem (2007) for the source parameters of the volumetric equation.

In fact, Demirmem calculated the ultimate recovery hydrocarbon volume, which is given by

$$UR = OOIP \times RE, \tag{2.7}$$

where $OOIP$ is the original oil in place and RE is the recovery efficiency. Thus, the modifications needed in the methods described in Section 2.4 are mainly the inclusion of new source parameters in the respective calculations.

The equation used by Demirmem (2007) to calculate OOIP presents a small modification when compared to Equation 2.1, so that the oil formation volume factor B_{oi} is replaced by the shrinkage factor b_{oi}. Thus, in Demirmem (2007), the OOIP is defined by

$$OOIP = A \cdot h \cdot \phi \cdot (1 - S_{iw}) \cdot b_{oi} \;\; = \;\; GRV \cdot N/G \cdot \phi \cdot (1 - S_{iw}) \cdot b_{oi}, \tag{2.8}$$

so that $B_{oi} \;=\; {b_{oi}}^{-1}$.

The method used for Demirmem (2007) to estimate the ultimate recovery (UR)

value is based on stochastic reserves calculations for the reservoir *KK*. The input variables used in the calculations were assumed independent and lognormally distributed. The resulting (untruncated) UR distribution is also lognormal. In his simulation, the lognormal distributions were defined by P90 and P10 parameters, with the other parameters calculated from the simulation.

Demirmem (2007) does not explain how he defined the uncertainty in the source parameters of the ultimate recovery equation (the mean and standard deviation values). Thus, any calculation making use of the Demirmem (2007) data can not be compared directly to the calculations described in Section 2.3 (which made use of error estimation from geostatistic analysis). However, the values provided by Demirmem (2007) can be used to compare the predictions for HCPV and UR associated with both methods described in Section 2.4. To do so, small modifications in these methods have to be implemented, which consist in the inclusion of terms associated with b_{oi} and RE in Equation 2.5 and in the Monte Carlo simulation. The Taylor expansion and the Monte Carlo methodologies used the values for the mean and the standard deviation presented in Table 2.1 as the source parameters needed to estimate UR. In the case of the Monte Carlo simulation method, a lognormal distribution was used as the PDF associated with the reservoir's area. The remaining source parameters were assumed normally distributed.

The results obtained from this analysis are presented in Table 2.2, which shows the predicted ultimate recoveries estimate values obtained from Demirmem (2007) as well as the predictions obtained using the Taylor expansion method and the Monte Carlo method. Figure 2.13 shows the prediction for HCPV for the reservoir *KK*, as

Table 2.1: Information data used in the calculations (modified from Demirmem, 2007).

Parameter	P90	P10	P50	Mean	STD
A(acre) $\times$ 1000	1.20	2.90	1.87	1.98	0.70
h (ft)	70	148	102	106	32
n/g	0.68	0.92	0.79	0.80	0.09
ϕ_i	0.18	0.24	0.21	0.21	0.02
S_{oi}	0.64	0.74	0.69	0.69	0.04
b_{oi}	0.75	0.79	0.77	0.77	0.02
RE	0.28	0.40	0.33	0.34	0.02

calculated using the Taylor expansion method and the Monte Carlo method. As can be verified from the values contained in Table 2.2 and Figure 2.14, the results for UR from the Taylor expansion and the Monte Carlo simulation methods were compatible with the predicted values from Demirmem (2007).

As in the case of the Blackfoot reservoir, good agreement is observed between P20 and P80 in the predicted UR/CDFs obtained using both methods presented in Section 2.4. In the case of P90, the UR value associated with the application of the Taylor expansion underestimates the obtained by Demirmem (2007) – the Taylor expansion predicts P90 that is 82% of the predicted P90 by Demirmem (2007). For P10, the difference in the predictions is less than 2% in any methodology used.

The result for P90 is expected, because each one of the PDFs used by Demirmem (2007) to perform the calculations assumed a lognormal distribution and the Taylor expansion method described in Section 2.4 adopted a normal distribution for the UR value. In the Monte Carlo method, a lognormal distribution was used to simulate the reservoir's area values, thus the Monte Carlo method result in a better approximation for the calculation performed by Demirmem. A better agreement between the results of Demirmem (2007) and the Taylor expansion method can be obtained if we

perform the CDF calculation associated with the Taylor expansion assuming UR as a lognormal distribution (see Figure 2.14). Adopting a lognormal distribution for UR in the Taylor expansion method also allows a better agreement in the comparison of the Taylor expansion and the Monte Carlo methods.

Table 2.2: Predicted UR from Demirmem, 2007) and from the Taylor expansion and Monte Carlo methods (Section2.4)

Estimation	P90	P10	P50	Mean	STD
UR (MMBL) Taylor expansion - normal case	18.6	81.4	50	50	24.6
UR (MMBL) Taylor expansion - lognormal case	20.3	82.5	44.5	46.1	25.5
UR (MMBL) Monte Carlo	21.9	83.1	44.1	49.5	26.4
UR-untruncated (MMBL) Demirmem (2007)	22.5	81.8	42.9	48.7	26.2

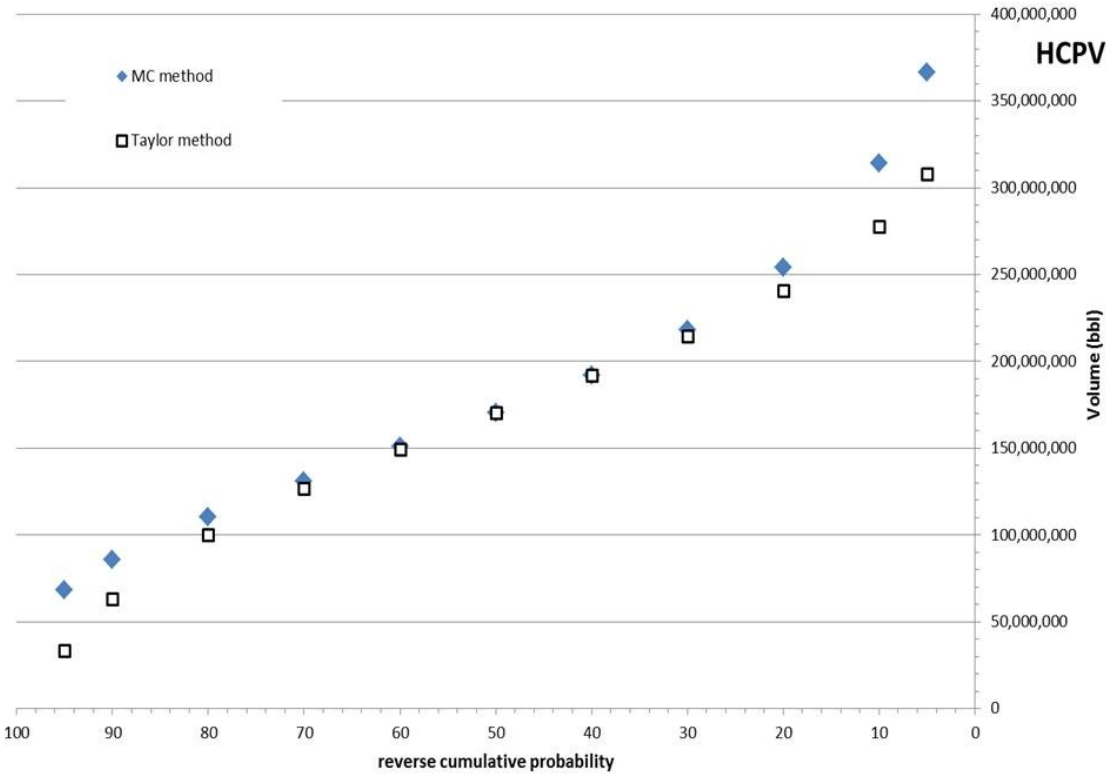

Figure 2.13: Cumulative distribution function for the hydrocarbon pore volume estimation. Hollow square: Taylor expansion method. Solid diamond: Monte Carlo approach.

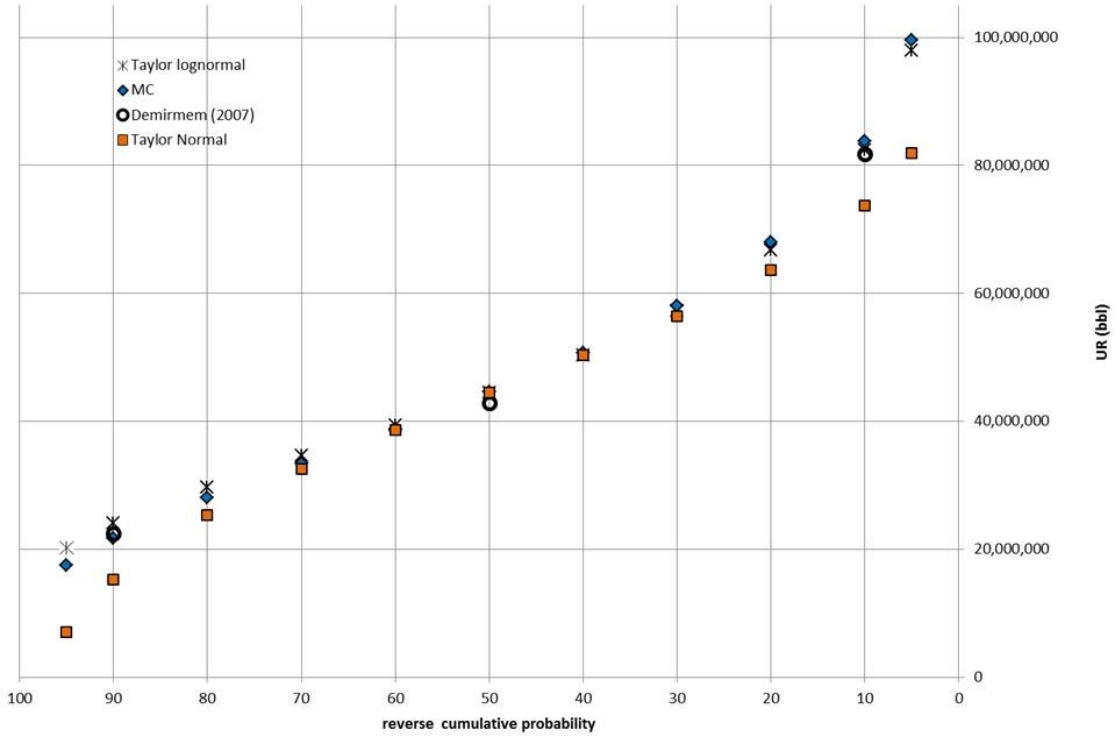

Figure 2.14: Cumulative distribution function for the ultimate recovery estimation. Orange/square: Taylor expansion method – normal PDF case. Blue/diamond symbol: Monte Carlo approach. Hollow circle: Demirmem (2007) predictions. Star symbol: Taylor expansion method – lognormal PDF case.

A LOGNORMAL HCPV DISTRIBUTION IN THE BLACKFOOT RESERVOIR

The lognormal distribution for HCPV used in the reservoir *KK* can also be applied to the case of the Blackfoot reservoir. The result is presented in Figure 2.15. From this Figure, it can be seen that the predictions obtained from the lognormal Taylor expansion and the Monte Carlo simulation are more consistent in the tails of the PDFs (extremes in the reverse cumulative probability values) than the case where the Taylor expansion assumes a normal distribution for HCPV. The Monte Carlo

simulation does not assume any shape for the HCPV distribution. Thus, the better match obtained with the lognormal Taylor expansion approach suggests that the HCPV distribution is more consistent with a lognormal distribution than a normal one, as expected from the theory (Murtha, 2002).

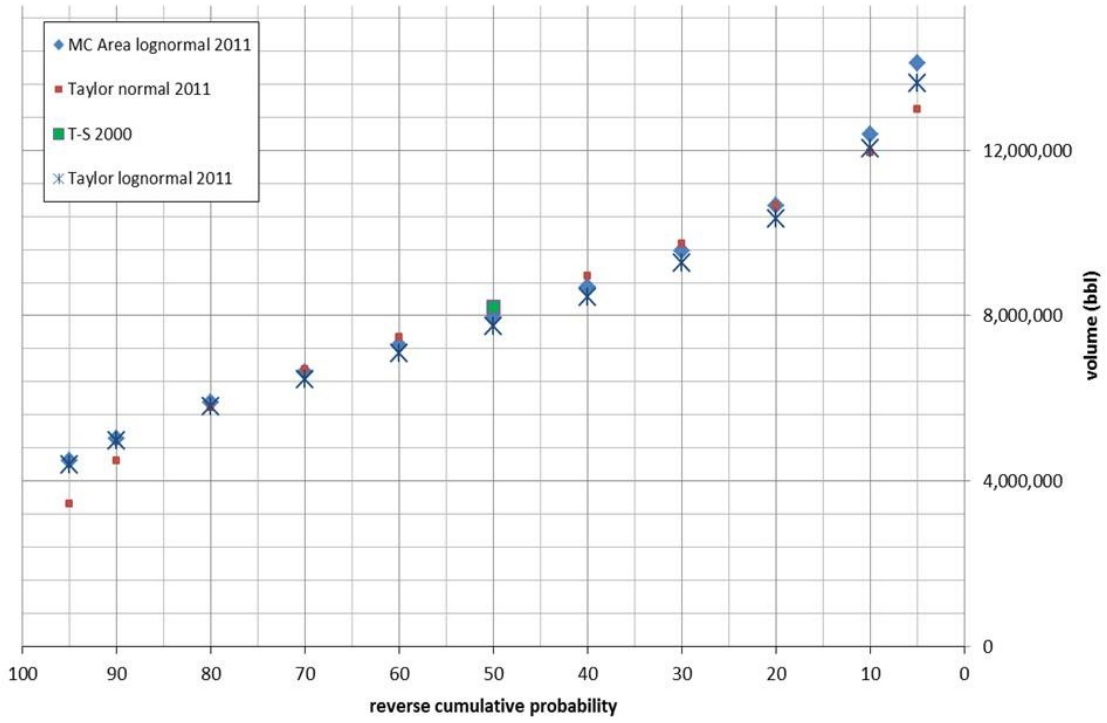

Figure 2.15: Cumulative distribution function for the HCPV estimation for Blackfoot reservoir. Little square: Taylor expansion method – normal PDF case. Blue/diamond: Monte Carlo approach. Large square/green: Todorov-Stewart estimation. Star symbol: Taylor expansion method – lognormal PDF case.

Chapter 3

Estimating fluid discrimination

Fluid discrimination is an important part of any exploration project of hydrocarbon reservoirs. As presented in Chapter 2, the hydrocarbon saturation is one of the parameters needed to evaluate the hydrocarbon volumes. One way to investigate the discrimination of fluids makes use of rock physics models and of the Gassmann's equation, and then looks for dependence in attributes with different fluid saturation values. Ultimately, we would find some seismic value or attribute(s) that, with logs, could predict S_w. This would then be used in Equation 2.1 to help predict OOIP.

In this chapter, I first characterize a well log dataset which contain information that allows the application of fluid substitution methods. This characterization allows the estimation of the statistical properties associated with the geophysical properties contained in the well log dataset. Then, I apply fluid substitution technique in the well log data. The fluid substitution data is applied for each sample separately. From these results, I calculated the mean and standard deviation associated with each property

for each specific value of depth. In this second line of investigation, I can evaluate which properties/attributes allow a better fluid discrimination. In a third part of this study, I investigate the robustness of any conclusion achieved in the previous part. Which properties/attributes sensitive to fluid discrimination investigated before can overcome the restriction imposed by the spatial variability observed in the well log data for each specific value of depth? To proceed with this investigation, I use Monte Carlo simulation to perform uncertainty analysis.

This chapter of the thesis makes use of a well log dataset from Gulf of Mexico generously provided by Prof. Fred J. Hilterman.

3.1 Applying the fluid substitution method

The P-wave and S-wave velocities (V_p and V_s) are calculated using the following equations

$$V_P = \sqrt{\frac{K + 4/3 \cdot \mu}{\rho}} = \sqrt{\frac{M}{\rho}} \tag{3.1}$$

and

$$V_S = \sqrt{\frac{\mu}{\rho}} \tag{3.2}$$

where K is bulk modulus, μ is shear modulus, M is the compressional modulus, and ρ is the bulk density.

To perform fluid substitution, which was briefly discussed in Section 1.8, we have to realized which terms in equations 3.1 and 3.2 are sensitive to the fluid content. On the one hand, the shear modulus μ is not sensitive to the variation in the fluid content (Mavko et al., 2009; Han and Batzle, 2004). On the other hand, K and ρ are sensitive

to the fluid content. As discussed by Han and Batzle (2004), a explanation for this difference of sensitivity is that the bulk-volume deformation produced by a passing seismic wave results in a pore-volume change and causes a pressure increase in pore fluid (water). This pressure increase stiffens the rock frame and causes an increase in bulk modulus. Shear deformation, however, does not produce a pore-volume change, and consequently different fluids do not affect shear modulus. Therefore, any fluid-saturation effect should correlate mainly to a change in bulk modulus.

The calculation of the effect in density of the variation in the density of the fluid is simple, and will be present later. In the case of the bulk modulus K we have a more complex situation. It is well accepted, however, that the Gassmann's equation allows the estimation of the fluid content in porous sandstones (Mavko et al., 2009).

Thus, Gassmann's equations are commonly used in the fluid substitution approach to predict velocity changes resulting from different pore fluid saturations. There are different forms to present the Gassmann's equation (Mavko et al., 2009). One of these forms is presented below (Han and Batzle, 2004), where K_s (sometimes labeled K_{sat}) is the bulk modulus of the saturated rock and K_d is the bulk modulus of the rock frame (or dry rock). Thus, for a rock with porosity ϕ,

$$K_s \;=\; K_d + \Delta_d \tag{3.3}$$

where Δ_d is given by

$$\Delta K_d \;=\; \frac{K_{ma}\,(1 - K_d/K_{ma})^2}{1 - \phi - K_d/K_{ma} + \phi \cdot K_{ma}/K_f} \tag{3.4}$$

and it contains the effect of the fluid in the bulk modulus. In these equations, K_{ma}, K_f, K_d, K_s, are the bulk moduli of the mineral grain or matrix, fluid, dry rock

(or porous frame), and saturated rock frame, respectively. The shear modulus is considered insensitive to the fluid content (Han and Batzle, 2004), thus we have that

$$\mu_s \;=\; \mu_d \tag{3.5}$$

where μ_s and μ_d are the saturated and dry-rock shear moduli. ΔK_d is an increment of bulk modulus as a result of fluid saturation of dry rock.

In addition to the modification of the saturated bulk modulus K_{sat} when we perform a fluid substitution, the bulk density value also has to be modified. The effect in the bulk density of a variation in the density of the fluid can be calculated using the equation below,

$$\rho_b \;=\; \phi\,\rho_{fluid} + (1-\phi)\rho_{ma} \tag{3.6}$$

where ρ_b is the bulk density of the saturated rock, ρ_{fluid} is the fluid density, ϕ is the porosity of the rock, and ρ_{ma} is the density of the rock matrix. In the case in which the fluid is composed by gas and brine, the fluid density is given by

$$\rho_{fluid} \;=\; S_w\,\rho_{brine} + S_{gas}\,\rho_{gas} \tag{3.7}$$

where S_w is the brine saturation, ρ_{brine} is the brine saturation, S_{gas} is the gas saturation, and ρ_{gas} is the gas density. Along the calculations presented in this chapter, I adopted $\rho_{gas} = 0.5\,\mathrm{gm/cc}$, and ρ_{brine} is calculated using Equation 3.11. To calculate the bulk modulus of mineral matrix, we need to know the mineral composition of the rock. This information is not available from the data, so a value presented by Mavko et al. (2009) used in sandstones, $K_{ma} = 36\,\mathrm{GPa}$, was adopted.

The main assumptions involved with the Gassmann's equation are (Han and Batzle, 2004):

1) the porous material is isotropic, elastic, monomineralic, and homogeneous;

2) the pore space is well connected and in pressure equilibrium;

3) the medium is a closed system with no pore-fluid movement across boundaries;

4) there is no chemical interaction between fluids and rock frame (thus, the shear modulus remains constant),

and were already discussed in Section 1.8.

The fluid substitution method is a well-recognized technique used to understand and predict how seismic velocities and impedances depend on pore fluids constituents (Avseth et al., 2005). However, the use of the fluid substitution technique is not without some risk. As discussed by Chaveste and Hilterman (2007), there is ambiguity in the relationship between rock properties (e.g., P-wave and S-wave velocities, density) and petrophysical properties (e.g., lithology, porosity, pore fluids). More than one combination of petrophysical properties can yield the same rock property value.

To apply fluid substitution to the well log dataset available in this study, I first used the mud weight to calculate the pore pressure, and then used the pore pressure and temperature information for each depth to calculate the brine density and velocity in that specific depth (Mavko et al., 2009). In addition, the S-wave velocity data (V_S) was obtained using the V_P data and the Greenberg-Castagna relations for the appropriate lithology (Hilterman, 2001). The porosity was obtained using the density log and appropriate values for the matrix density and the fluid density (Hilterman, 2001). After these steps, the fluid substitution method was applied to the well log data, using the Gassmann's equation. Sections 3.2 and 3.3 present a more detailed discussion of all steps taken to apply the fluid substitution procedure.

3.2 Characterizing the well log dataset

The well log database contains samples over a depth range from 700 ft to 12,300 ft (0.21 km to 3.75 km). The results of the characterization of the well log dataset were presented separately in two groups: non-seismic attributes/properties and seismic attribute/properties. The original information contained in the well log dataset was worked using standard procedures, which are presented next.

3.2.1 Non-seismic attributes/properties

The original information in the well log dataset contains the information about temperature and mud weight. Figure 3.1 shows the variation of the temperature versus depth. In this figure, the sample data points and the average of the sample data points for each specific depth are presented. It can be seen in this figure that the spread in temperature increases with depth. The well log dataset shows a temperature gradient given by T(°C) = 19.45· depth(km) + 25.01, which is in agreement with the temperature gradient for Gulf of Mexico as given by Husson et al. (2008). This temperature gradient was estimated using the least squares method and it is also shown in Figure 3.1.

The original information in the well log dataset for Gulf of Mexico also includes measurements of the mud weight. Assuming that the drilling mud weight equals the formation pore pressure (Bachrack et al, 2007), the mud weight can be used to estimate the pore pressure through the equation below:

$$P_p\,(psi) \;\simeq\; MW \cdot z \cdot 0.052 \tag{3.8}$$

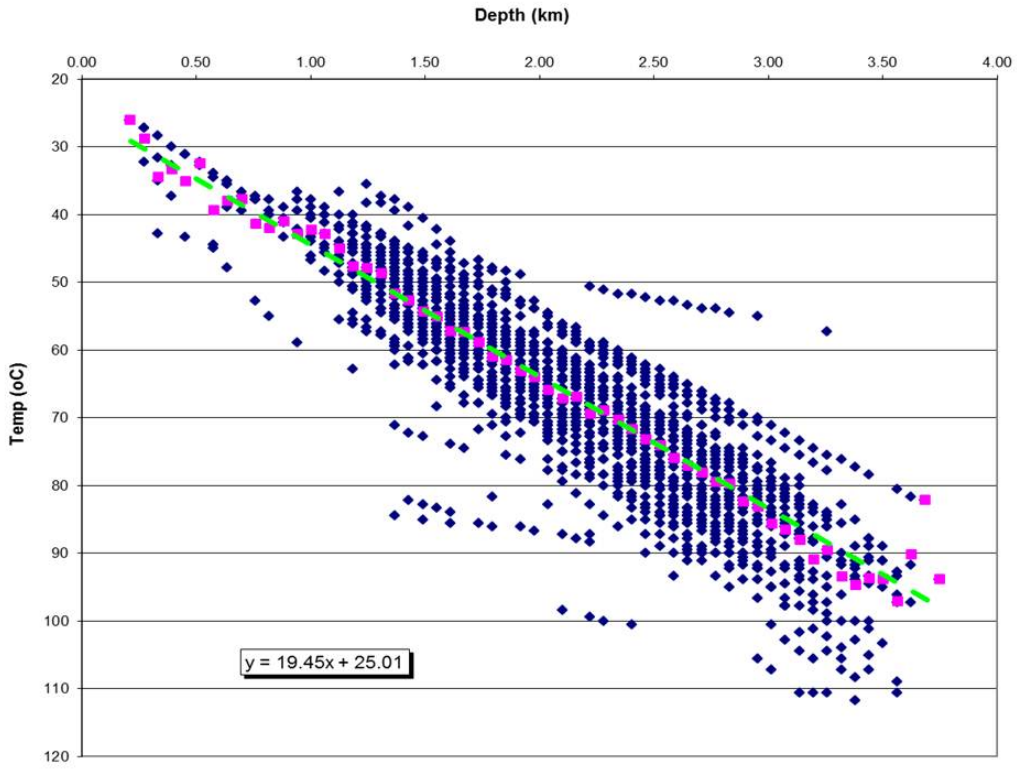

Figure 3.1: Temperature versus depth. The blue/diamond points represent the sample data, while the magenta/square points represent the average value for each depth interval.

where P_p is the pore pressure in psi, MW is the mud weight in pounds per gallon, and z is the total vertical depth in feet. If the correct mud weight was used, it is expected that the actual pore pressure would be 1–2 psi lower than the predicted one using Equation 3.8 (Castagna, pers. comm., 2011).

Figure 3.2 shows the variation of the pore pressure versus depth. In this figure, the sample data points are shown in blue/diamond, while the average of the sample data points for each specific depth are shown in magenta/square. It can be seen in the pore pressure variation with depth that the spread of the pore pressure values increases with depth. The pore pressure gradient fits very well a straight line, which

was obtained with the least squares method The pore pressure gradient is given by $P_p(MPa) = 14.67 \cdot depth(km) - 3.21$, which is consistent with the presented Husson et al. (2008).

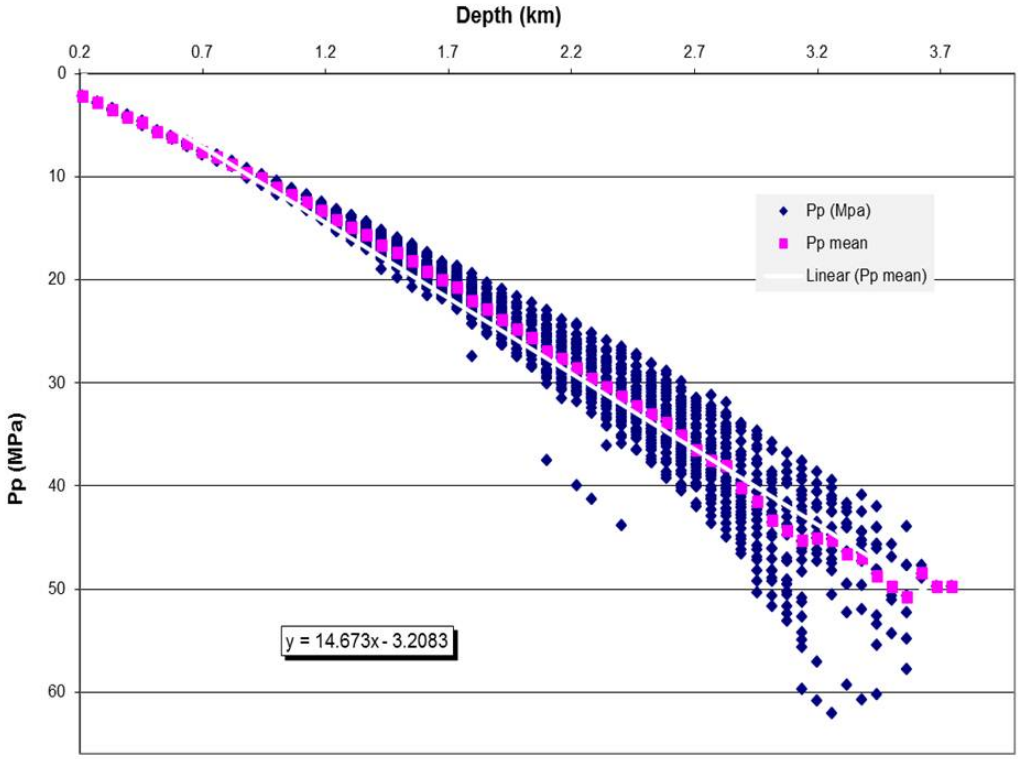

Figure 3.2: Pore pressure versus depth. The blue/diamond points represent the sample data, while the magenta/square points represent the average value for each depth interval.

Using the information contained in the density logs, the overburden pressure can be calculated through the equation below (Zoback, 2010):

$$P_{overburden} \;=\; p_0 \;+\; \int_0^z \overline{\rho}\; g\; z\; dz \tag{3.9}$$

where the overburden pressure is given in MPa, the bulk density ρ_b is given in Kg/m^3, g is the acceleration due to gravity (I adopted 9.8 m/s^2), and P_0 is the datum pressure.

Figure 3.3 shows the gradients of the overburden pressure and of the pore pressure, as a function of the depth z. The gradient values estimated from the plot, using a straight line fitted using the least square method, were 0.0227 MPa/m for the overburden pressure (which are in good agreement with the estimated values presented in Castagna et al. 1993b and Husson et al. 2008).

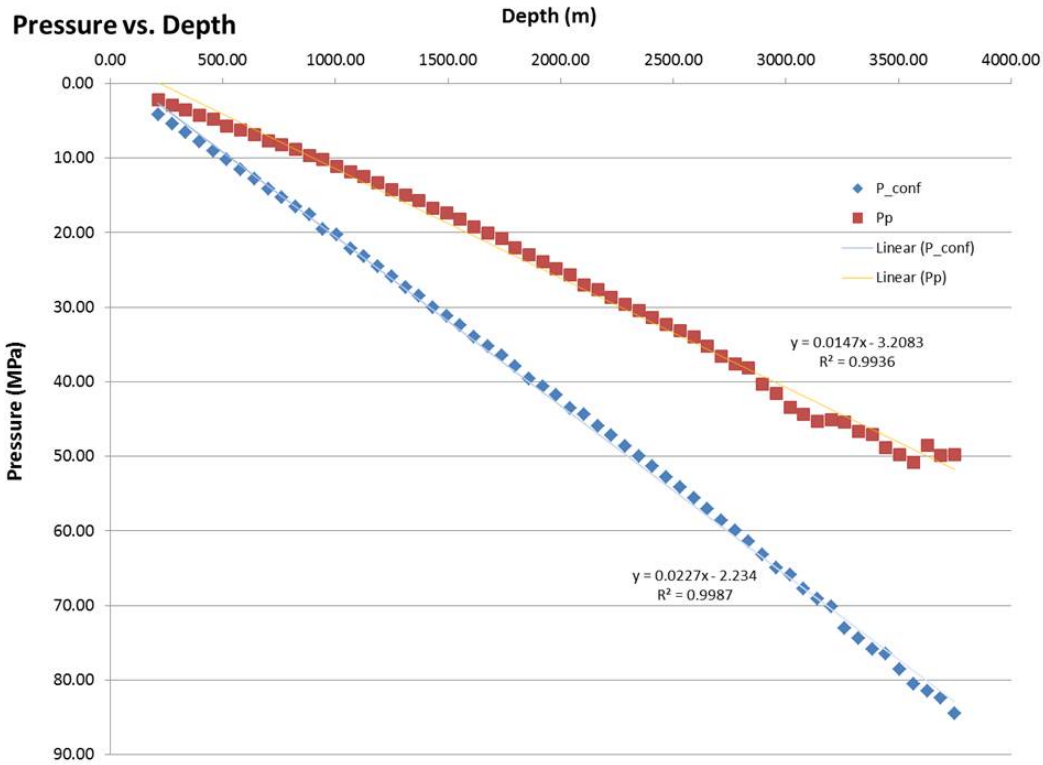

Figure 3.3: Overburden pressure (blue/diamond) and Pore pressure (red/square) versus depth.

3.2.2 Seismic attributes/properties

Figure 3.4 shows the variation of the P-wave velocity V_P for wet sand (blue/squares) and for shale (green/diamond) as a function of depth. It can be seen in the figure that

V_P increases with depth, but that there is also a crossover around depth equal to1 km of the average values of V_P for shale and for wet sand. A linear fit carried out using the least square method shows that the V_P for wet sand variation can be described by the expression $V_P^{wet\ sand} = 0.5914 \cdot z + 1.6386$ ($R^2 = 0.99$), where z is in km and V_P is in km/s. The same procedure applied to V_P for shale gives $V_P^{shale} = 0.4586 \cdot z + 1.741$ ($R^2 = 0.99$).

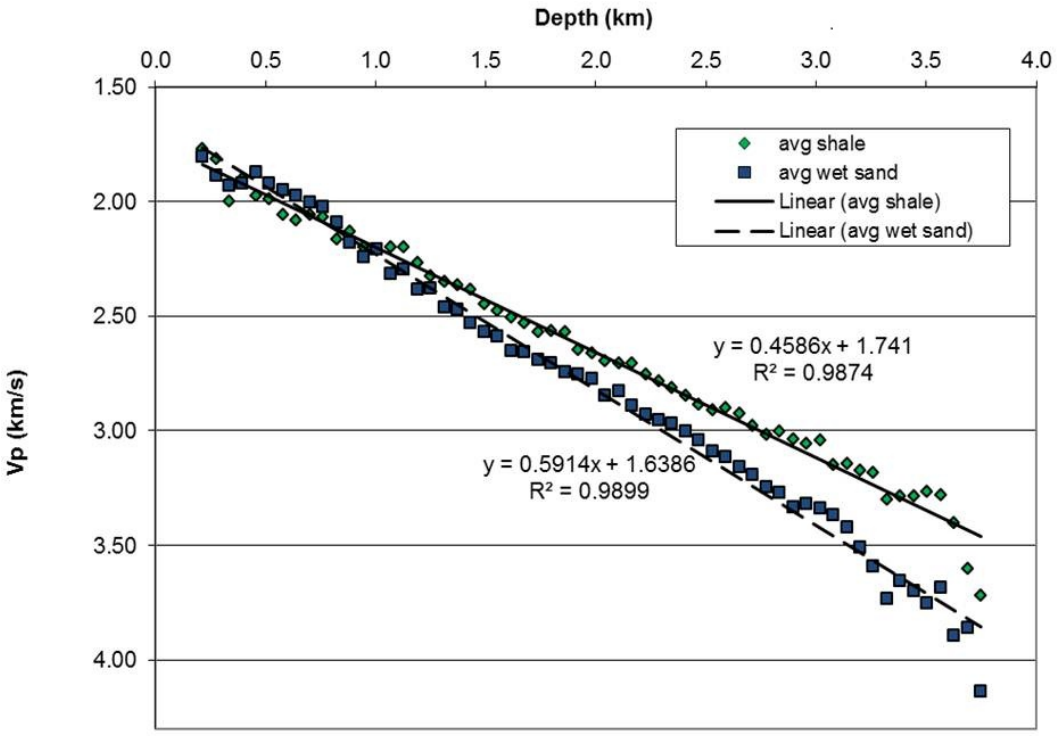

Figure 3.4: Average V_P versus depth. The blue/square points represent the wet sand samples, while the green/diamond points represent the shale samples.

Figure 3.5 shows the variation of the density for wet sand and for shale as a function of depth. It can be seen in figure 3.5 that ρ increases with depth. A linear fit carried out using least square method shows that the density for wet sand variation with depth can be described by the expression $\rho_{wet\ sand} = 0.000025 \cdot z + 1.99$ ($R^2 =$

0.96), where z is in feet and ρ is in gm/cc. The same procedure applied for the density for shale gives $\rho_{shale} = 0.000025 \cdot z + 2.05$ ($R^2 = 0.84$). These expressions are consistent with that described in Hilterman (2001).

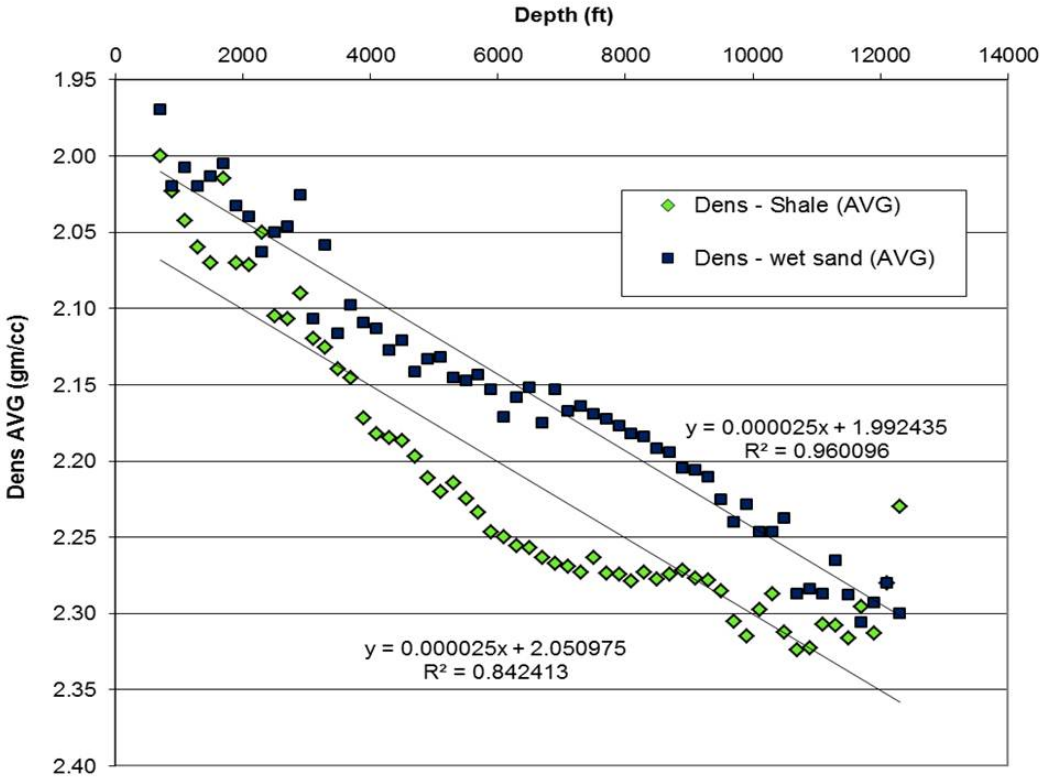

Figure 3.5: Average bulk density versus depth. The blue/square points represent the wet sand samples, while the green/diamond points represent the shale samples.

The shear velocity V_S was estimated using the Greenberg and Castagna (1992) equations, applying the relation associated with each related lithology separately (shale or wet sand). After that, the V_P/V_S value was calculated. V_P/V_S as a function of depth is presented in the figure 3.6, where the sample data points are presented in blue/diamond (wet sand) and red/circle (shale), and the average value for each specific depth is presented in magenta/square (wet sand) and green/triangle (shale).

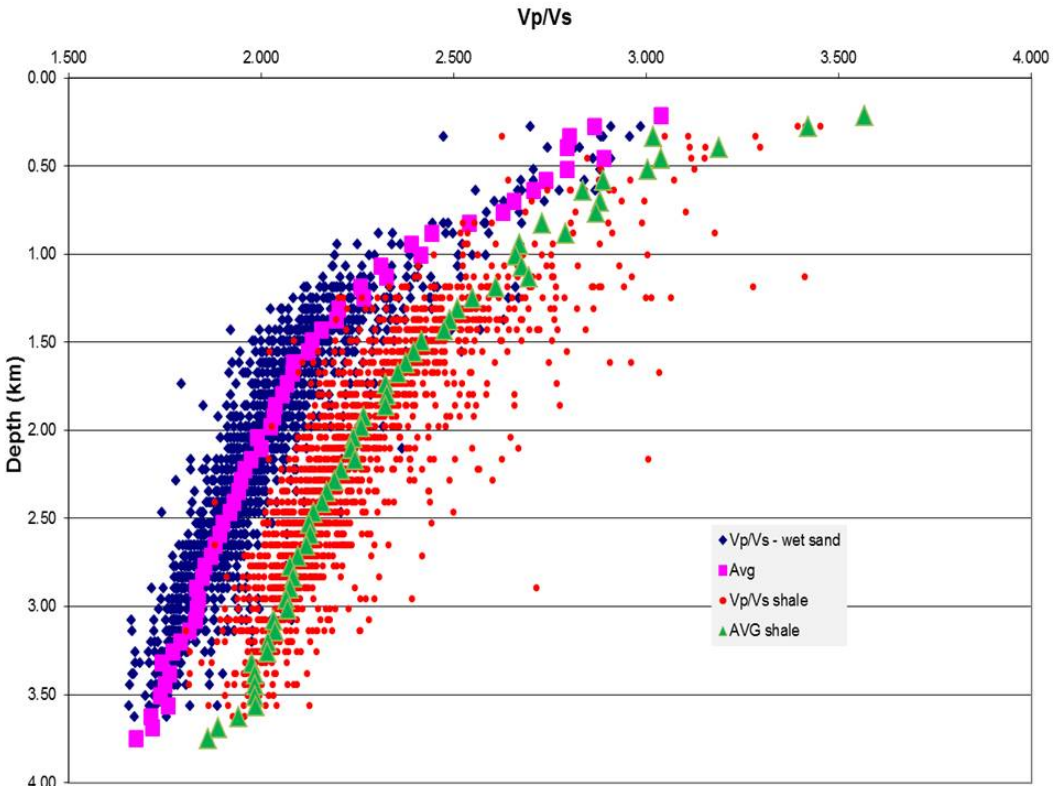

Figure 3.6: V_P/V_S ratio versus depth. Wet sand: The sample data points are shown in blue/diamond, and the average value for each depth interval is shown in magenta/square. Shale: the sample data is shown in red/circle, and the average value for each depth interval is shown in green/triangle.

The porosity ϕ was estimated using the density log and the relation given by (Ezekwe, 2011)

$$\phi = \frac{\rho_{ma} - \rho_b}{\rho_{ma} - \rho_f} \tag{3.10}$$

where ρ_{ma} is the rock matrix, ρ_b is the bulk density, and ρ_f is the fluid density. In the calculations carried out in this thesis, a value of $\rho_{ma} = 2.65\,\mathrm{g}/cm^3$ was adopted. The fluid density was calculated using Equation 3.7.

to use Equation 3.7 for the calculation of the fluid density, first I calculated the brine density using the environmental corrections as presented in Mavko et al. (2009),

which takes into account the temperature, pressure, and salinity associated with the fluid. The equation used (from Mavko et al., 2009), is shown below

$$\begin{aligned} \rho_{brine} &= \rho_{water} + S\{0.668 + 0.44S + 10^{-6}[300P - 2400PS + \\ &+ T(80 - 3T - 3300S - 13P + 47PS]\} \end{aligned} \tag{3.11}$$

where S is the salinity of sodium chloride associated with the brine, T is the temperature, P is the pressure, and ρ_{water} is the density of pure water. In the calculations presented in this thesis, a constant value for the salinity equal to 25,000 ppm was adopted. The density for pure water was calculated using the equation presented in Mavko et al. (2009), and it is given by:

$$\begin{aligned} \rho_{water} &= 1 + 10^{-6}(-80T - 3.3T^2 + 0.00175T^3 + 489P - 2TP + \\ &+ 0.016T^2P - 1.3 \cdot 10^{-5}T^3P - 0.333P^2 - 0.002TP^2 \end{aligned} \tag{3.12}$$

In Equations 3.11 and 3.12 the pressure P is in MPa units, the temperature T is in $^{\circ}C$, the salinity S is in fractions of one (parts per million divided by 10^6), and the density is in g/cm^3.

Thus, after the environmental corrections associated with Equations 3.11 and 3.12, the porosity for wet sand was calculated. Figure 3.7 shows the variation of porosity for wet sand as a function of depth. Blue/diamond points shows the wet sand sample data, while the magenta/square symbols show the average porosity estimated for each depth interval. The porosity values present a large spread along the depth values, and this spread is reduced only where the dataset does not have enough sample data points. A linear fitting applied to the average data resulted in an expression for porosity as a function of depth that is given by $\phi = -0.0509 \cdot z + 0.402$ ($R^2 = 0.96$),

where ϕ is porosity and z is depth in km. The use of this kind this expression to estimate porosity values for some specific depth should be made knowing that the spread of the porosity values is large, so that the uncertainty associated with this estimation is also very large.

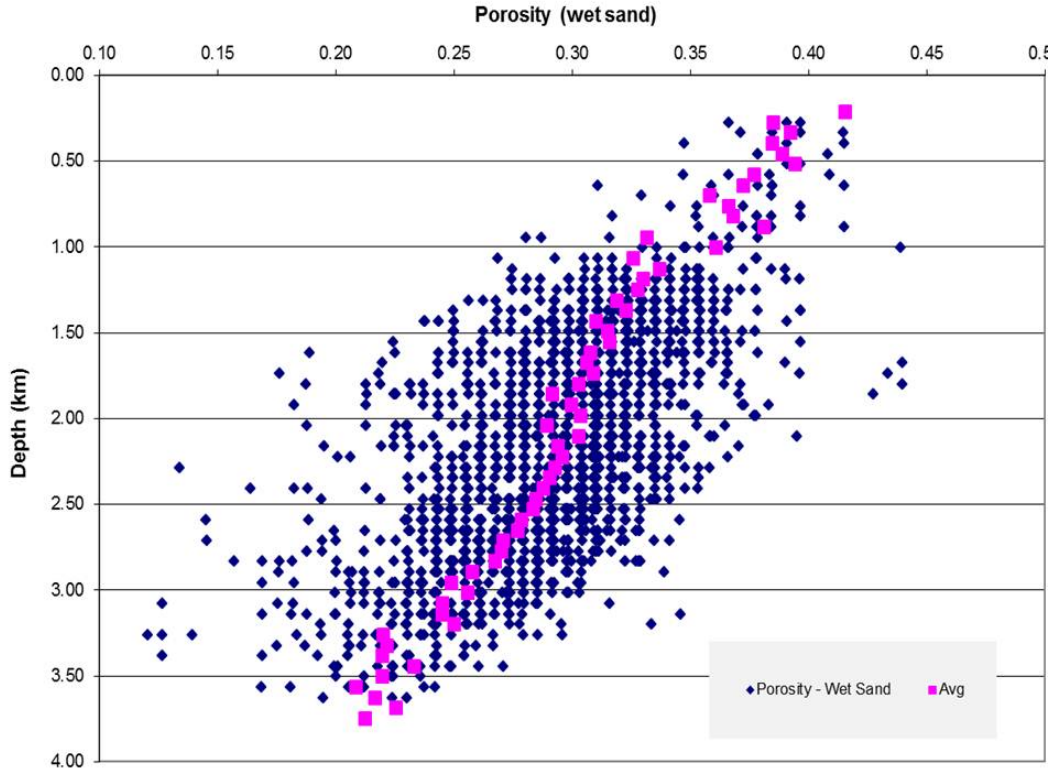

Figure 3.7: Porosity for wet sand versus depth. Blue/diamond: sample data points. Magenta/square: average value for each depth interval.

The P-wave velocity in brine in m/s is given by (Mavko et al., 2009)

$$\begin{aligned} V_{brine} &= V_w + S\,(1170 - 9.6T - 0.055T^2 - 8.5\cdot 10^{-5}T^3 + \\ &+ 2.6P - 0.0029TP - 0.0476P^2) + \\ &+ S^{3/2}(780 - 10P + 0.16P^2) - 1820S^2 \end{aligned} \tag{3.13}$$

where the P-wave velocity in pure water is given by (Mavko et al., 2009)

$$V_w \;=\; \sum_{i=0}^{4}\sum_{j=0}^{3} \omega_{ij}\; T^i\; P^j \tag{3.14}$$

and the coefficients ω_{ij} are given by

$\omega_{00} = 1402.85 \quad , \quad \omega_{01} = 1.524 \quad , \quad \omega_{02} = 3.437\times10^{-3} \quad , \quad \omega_{03} = -1.197\times10^{-5}$

$\omega_{10} = 4.871 \quad , \quad \omega_{11} = -0.0111 \quad , \quad \omega_{12} = 1.739\times10^{-4} \quad , \quad \omega_{13} = -1.628\times10^{-6}$

$\omega_{20} = -0.04783 \;,\; \omega_{21} = 2.747\times10^{-4} \;,\; \omega_{22} = -2.135\times10^{-6} \;,\; \omega_{23} = 1.237\times10^{-8}$

$\omega_{30} = 1.487\times10^{-4},\; \omega_{31} = -6.503\times10^{-7},\; \omega_{32} = -1.455\times10^{-8},\; \omega_{33} = 1.327\times 10^{-10}$

$\omega_{40} = -2.197\times10^{-7},\; \omega_{41} = 7.987\times10^{-10},\; \omega_{42} = 5.230\times10^{-11},\; \omega_{43} = -4.614\times10^{-13}$

in both equations, P is the pressure in MPa, T is the temperature in $^{\circ}C$ and S is the salinity of sodium chloride associated with the brine in fractions of one (parts per million divided by 10^6).

The bulk modulus of the wet sand, $K_{wet\ sand}$, can be calculated using the values of the P-wave velocity and density, together with Equation 3.1. To calculate the Reuss and Voigt moduli (Avseth et al., 2005), information of the bulk modulus of the rock matrix (K_{ma}) of sandstones and of the bulk modulus of the brine (K_{brine}) have to be estimated. As discussed previously, a value of $K_{ma} = 36$ GPa was adopted in this study (Mavko et al., 2009). The bulk modulus of the brine was calculated using the velocity and density values computed using Equations 3.11 and 3.13. From the Reuss and Voigt moduli, the Hill's modulus was calculated. The result of this calculation is presented in Figure 3.8. A possible origin for the large spread of the

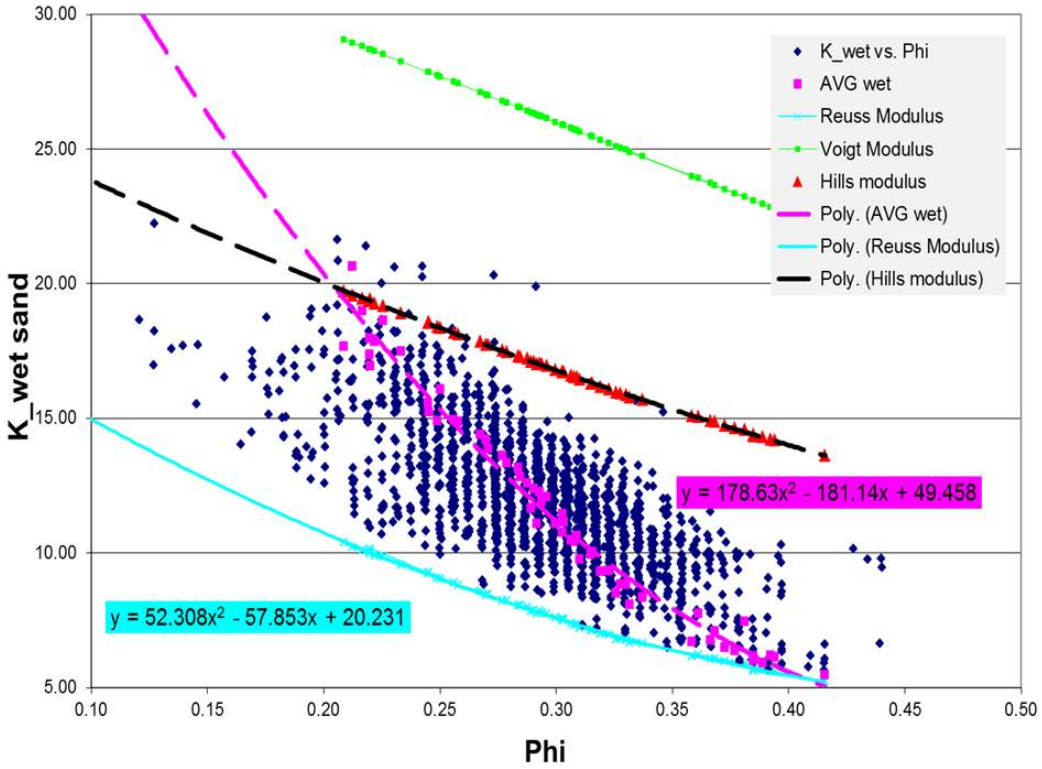

b

Figure 3.8: Bulk modulus for wet sand versus porosity. Blue/diamond show sample data points, while magenta/square symbols show the average value of the sample points for each depth interval. Cyan line shows the Reuss modulus, while Green line shows the Voigt modulus. Black dashed line shows the Hill's modulus. A regression curve was fitted to the average value of the sample points for each specific depth, and is presented as a magenta dashed line.

sample values observed in Figure 3.8 can be associated with mineralogy effects, since the classification of the lithology between shale and wet sand is subject to cut-offs and uncertainty. However, as the original information in the well log dataset does not contain quantitative information from gamma-ray log, this hypothesis can not be verified.

The well log data was also used for obtaining a locally calibrated relationship

between the P-wave velocity and the density for wet sands. This relationship will be used during the fluid substitution procedure, when in Section 3.3.1 a correlated Monte Carlo approach which uses the expression related to that is applied. The expression obtained for the locally calibrated data is given by $\rho = 0.4241\ V_P^{0.1785}$, with ($R^2 = 0.97$), and with V_p given in feet and density in g/cm^3.

3.3 Fluid substitution

Now that the well log dataset characterization was discussed, the application of fluid substitution to the wet sand sample data points is described. The effect of three different saturations were investigated. The first saturation corresponds to the wet sand case, which have $S_w = 1.0$. The second saturation corresponds to a reservoir with characteristics of fizz gas, which $S_w = 0.95$. The third and last case corresponds to a gas reservoir with $S_w = 0.5$.

The effect of the variation of the fluid saturations was investigated using crossplots that are recognized in the literature as sensitive to the fluid content (Hilterman, 2001). These crossplots were:

- Vp/Vs versus Vp,
- P-impedance (Ip) versus S-impedance (Is),
- Normal incident reflectivity (NI) versus Poisson reflectivity (PR),
- $\lambda\rho$ versus $\mu\rho$.

The Vp/Vs–Vp crossplot is sensitive to the fluid content because when the rock pore space is filled with a different fluid, the Vp velocity tends to change as a response

to the fluid change, while the Vs velocity is insensitive to this fluid change. The result is that in the Vp/Vs–Vp crossplot, a point representing a specific overall set of properties of a porous rock will change its position in the crossplot as a response to the variation of some of the original rock properties. A caveat in the use of this crossplot to evaluate fluid content is that the Vp/Vs–Vp crossplot is also sensitive to variations of other properties such as pore pressure, porosity and clay volume (Avseth et al., 2005).

Figure 3.9 shows the effect of the different saturations and of the lithology in the Vp/Vs—Vp crossplot. The response to the variation of the lithology shows that sandstones and shales have different behavior in this crossplot. Figure 3.9 also shows shale tends to have Vp/Vs ratio that is larger than the Vp/Vs value for sandstones for a constant value of V_P. This is specially clear in the shallow areas, which in this crossplot corresponds to high Vp/Vs ratio and low Vp.

The effect of the fluid saturation is also clear in Figure 3.9. In the case of a mixture of gas and brine, when the water saturation is reduced it is possible to discriminate the wet sand case from the fizz gas case. As the water saturation continues to be reduced, we can observe in Figure 3.9 that the Vp/Vs ratio becomes insensitive to the gas saturation — the Vp/Vs ratio becomes essentially flat with V_P.

Continuing with the analysis of the effect of the fluid saturation, the case of the Ip–Is crossplot is discussed. The P-impedance Ip is obtained from the expression below

$$Ip \;=\; V_P \; \rho \tag{3.15}$$

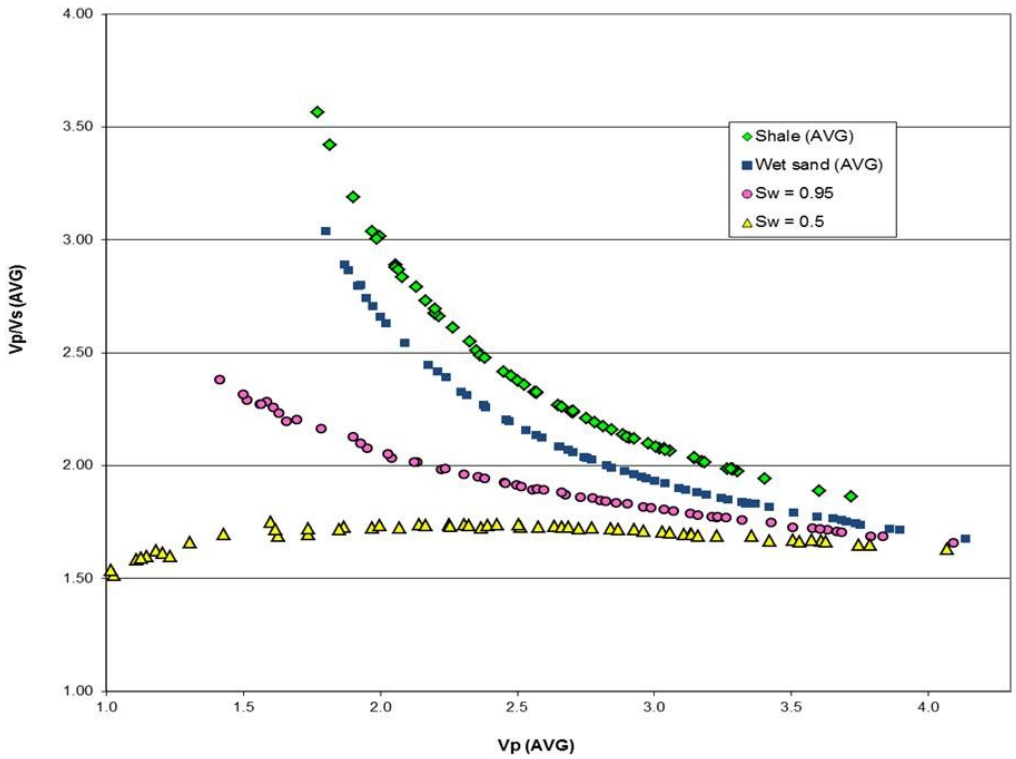

Figure 3.9: Vp/Vs ratio versus Vp. Green/diamond: average value for each depth for shale. Blue/square: average value for each depth for wet sand (Sw= 1.0). Magenta/circle: average value for each depth for sands with Sw = 0.95 (fizz case). Yellow/triangle: average value for each depth for sands with Sw = 0.5.

and the S-impedance Is is given by

$$Is \;=\; V_S\;\rho \tag{3.16}$$

Figure 3.10 shows the results obtained after the fluid substitution procedure. It can be seen from this plot that at low impedances, corresponding to shallow areas, we can identify a better discrimination of fluid in the sands. In fact, it can be seen that the P-impedances for the different saturations follows straight lines which become closer to each other at higher depths.This, the discrimination of fluids becomes hard to achieve in deeper reservoirs. The lithology also can be evaluated using the Ip–Is

crossplot, as can be seen in Figure 3.10.

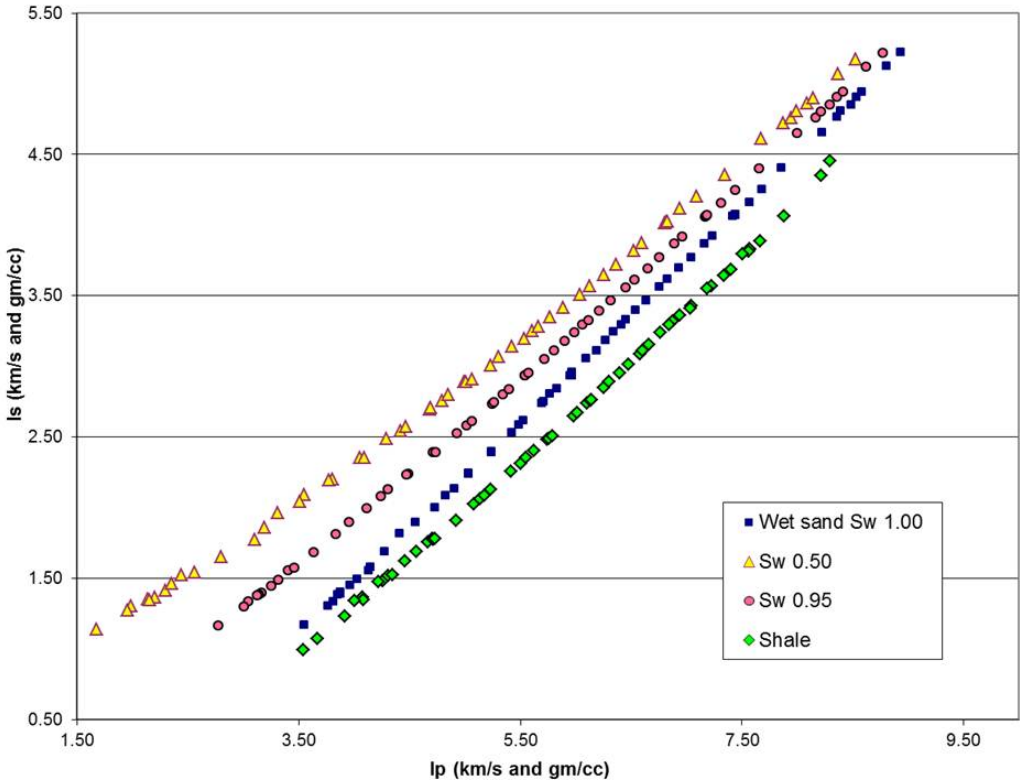

Figure 3.10: P-Impedance versus S-impedance. Green/diamond: average value for each depth for shale. Blue/square: average value for each depth for wet sand (Sw= 1.0). Magenta/circle: average value for each depth for sands with Sw = 0.95 (fizz case). Yellow/triangle: average value for each depth for sands with Sw = 0.5.

The next fluid discriminator to be investigated was the NI–PR crossplot (Hilterman, 2001). The normal incident reflectivity (NI) is given by

$$NI = \frac{V_{p2}\,\rho_2 - V_{p1}\,\rho_1}{V_{p2}\,\rho_2 + V_{p1}\,\rho_1} \tag{3.17}$$

where V_{p2} and ρ_2 correspond to the P-wave velocity and the density for the upper medium (shale) and V_{p1} and ρ_1 correspond to the P-wave velocity and the density for

the lower medium (sand). The Poisson's reflectivity (PR) is given by

$$PR \;=\; \frac{(\sigma_2 \;-\; \sigma_1)}{(1 \;-\; \sigma_{avg})^2} \tag{3.18}$$

where σ_1 and σ_2 correspond to the poisson's ratio of the upper medium (shale) and lower medium (sand), respectively. σ_{avg} corresponds the average value of both poisson's ratios, so that $\sigma_{avg} \;=\; \frac{\sigma_2+\sigma_1}{2}$.

Figure 3.11 shows that shallow areas (high negative NI and PR values) present a better fluid discrimination power than deeper areas. In fact, the average values for NI and PR calculated for each specific depth shows that at deeper reservoir the discrimination between all saturations can become pretty difficult, specially in the case involving the fizz gas case.

The last crossplot used to investigate the fluid discrimination power was the $\lambda\rho$ versus $\mu\rho$ crossplot. This crossplot was proposed by Goodway et al. (1997). $\lambda\rho$ was defined by Goodway et al. as

$$\lambda\rho \;=\; (V_P\,\rho)^2 \;-\; 2\,(V_S\,\rho)^2 \tag{3.19}$$

where $\lambda\rho$ is a pore-fluid discriminator. The $\mu\rho$ attribute is given by

$$\mu\rho \;=\; (V_S\,\rho)^2 \tag{3.20}$$

As discussed by Hilterman (2001), $\lambda\rho$ is the Gassmann's fluid discriminant since this attribute is a good approximation for Gassmann's bulk modulus of the pore-fluid effect. Figure 3.12 shows the $\lambda\rho$ versus $\mu\rho$ crossplot. It can be seen that this crossplot shows a very good discriminator power, as discussed by Goodway et al. (1997) and Hilterman (2001). In fact, the three cases upon investigation, $S_w = 1.0$,

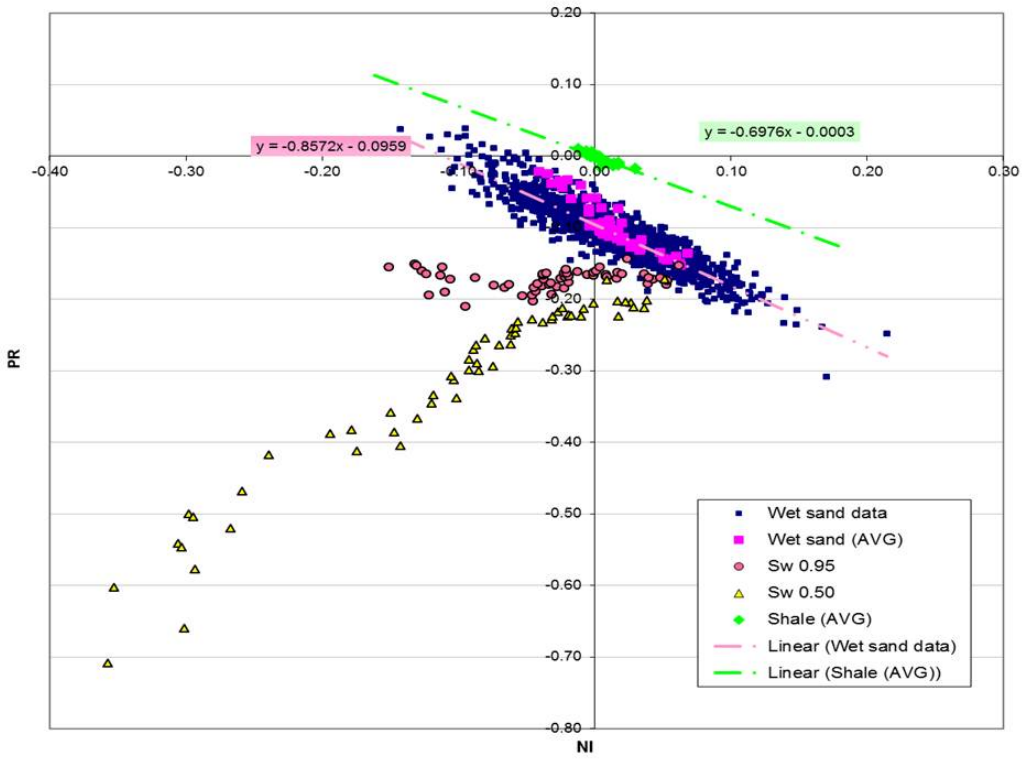

Figure 3.11: NI versus PR. Green: average value for each depth for shale. Blue/square: sample data points for wet sand (Sw= 1.0). Magenta/square: average value for each depth for the wet sand case. Red/circle: average value for each depth for sands with Sw = 0.95 (fizz case). Yellow/triangle: average value for each depth for sands with Sw = 0.5. Dashed-dot lines: linear fitting for the sample data points for wet sand (light pink) and for the average value for each depth for shale (green).

$S_w = 0.95$ and $S_w = 0.50$, present a constant separation in the $\lambda\rho$ axis in the average values calculated for each specific depth. Shallow reservoirs are characterized by small values of $\lambda\rho$ and $\mu\rho$, while deeper reservoirs are characterized by large values of these attributes. Good discrimination between shale and sandstone for deeper reservoirs is also observed in Figure 3.12.

It is important to keep in mind, however, a caveat discussed by Hilterman (2001)

about this crossplot: any noise presented in the data will also be magnified by this kind of attribute together with the fluid effect. In the use of this crossplot with seismic data this caveat can be specially important. Another caveat is that Figure 3.12 presents results for fluid discrimination looking at the average values for each depth obtained after the fluid substitution of all sample data points, and then does not consider actually the spread in the sample values. In the next section this last aspect will be discussed again using a different approach.

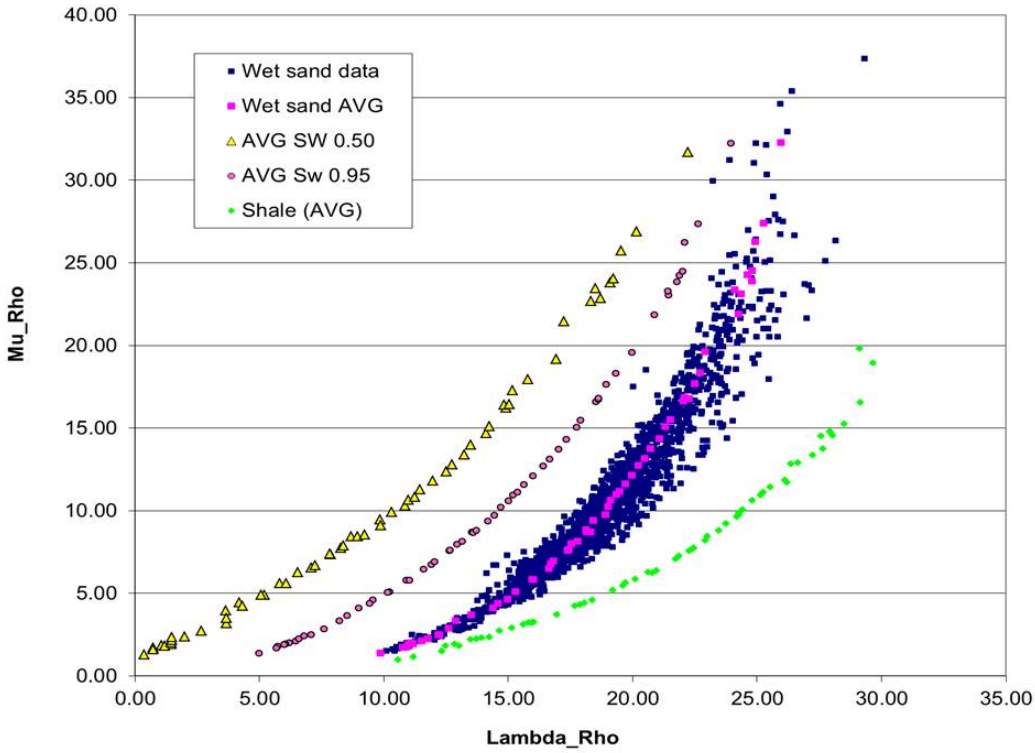

Figure 3.12: $\lambda\rho$ versus $\mu\rho$. Green points: average value for each depth for shale. Blue/square: sample data points for wet sand (Sw= 1.0). Magenta/square: average value for each depth for wet sand case. Red/circle: average value for each depth for sands with Sw = 0.95 (fizz case). Yellow/triangle: average value for each depth for sands with Sw = 0.5.

3.3.1 Monte Carlo simulation, fluid discrimination, & the effect of depth

One of the goals of this chapter was to evaluate the effect of uncertainty over geophysical attributes that are used by the oil industry to delineate and characterize a hydrocarbon reservoir. Another goal was to investigate the reliability of the fluid discrimination procedure based in the fluid substitution results. Both goals are related to the use of the volumetric equation, because fluid substitution results can be used in different steps associated with the determination of the values of the source parameters of the HCPV calculation. The estimation of the fluid discrimination confidence presented in this thesis were obtained from the well log database that contains samples over a depth range from 0.21 km to 3.75 km.

One interesting consideration about the fluid substitution technique is that at the same depth different rock properties are found. Thus, studies based on sensitivity analysis are important to evaluate what are the possibilities in the rock properties in subsurface that can be needed to understand a specific area. With this idea in mind, the Monte Carlo simulation technique was used to perform sensitivity analysis, since distributions of values instead of single average values help to avoid the flaw of averages (Avseth et al., 2005). Ignoring the variability of rock properties in quantitative computations can cause critical errors in the decision-making process.

Applying a Monte Carlo simulation involves specific steps. First, it is necessary to define a domain containing all possible inputs. Second, it is necessary generate inputs randomly from a probability distribution (PDF) over that domain. Third, it is necessary carry out a deterministic calculation on the inputs. Fourth, it is necessary

to aggregate the results.

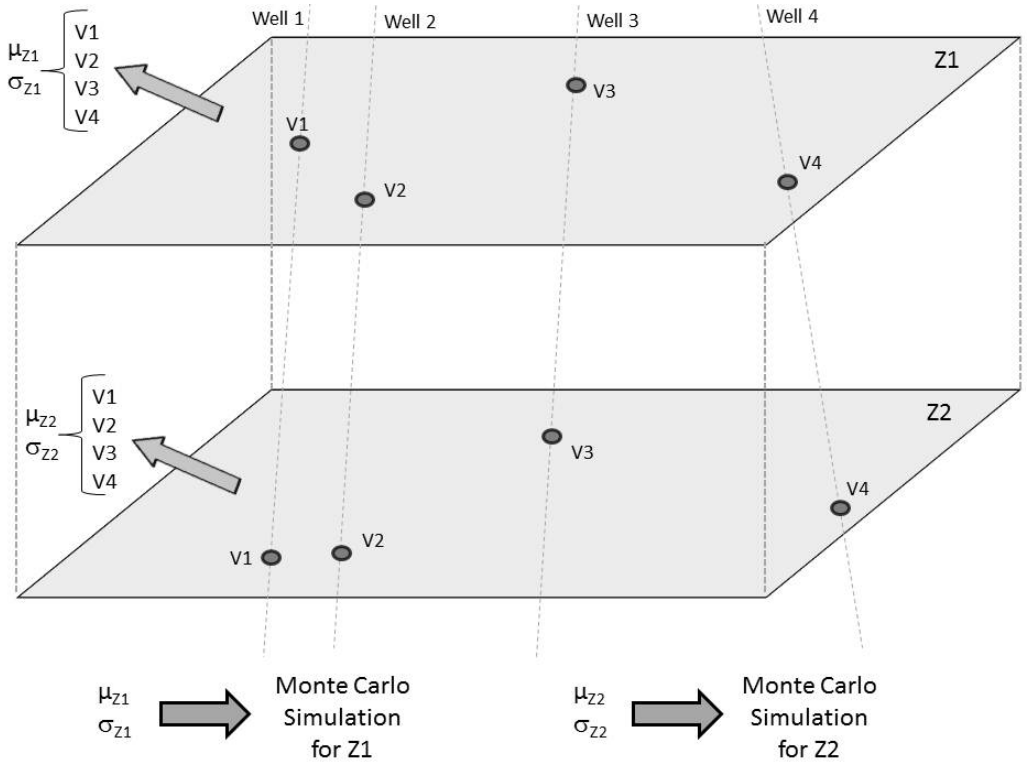

Figure 3.13: Illustration of the procedure to obtain the statistical properties of the original information in the well log dataset. Z1 and Z2 correspond to different depths. The mean and the standard deviation for each original well logged property was calculated for each specific depth. These statistical parameters were used as source parameters for the Monte Carlo simulation.

In the case of this research, steps 1 and 2 described above were carried out together. First, the mean and standard deviation values from the original well log properties described in Section 3.2 were calculated for each specific value of depth. Figure 3.13 illustrates this procedure. Then, a normal distribution PDF was adopted as describing the well log information for each depth. One convenient property of the normal distribution is that it is characterized just by two statistical parameters: the mean and the standard deviation. Using the mean and standard deviation values calculated

for each original well log property for each depth, the domain of all possible inputs (step 1) is generated directly from the carrying out of step 2. After that, each one of the sampled values with the original well log properties was submitted to the step 3, using the Gassmann's equation and the fluid substitution procedure as described in Section 3.1. The results obtaining from this procedure applied in the original well log data (mud weight, temperature, V_P for shale and for wet sand, density for shale and wet sand), the step 4, are presented next.

In the case of the density, a correlated Monte Carlo approach (Avseth et al., 2005) was applied making use of the locally calibrated empirical relationship between the density ρ and V_P (Castagna et al. 1993) as a constraint in the simulation. The procedure was applied as follows. First the mean and standard deviation for V_P and for ρ were calculated. I then used the mean and standard deviation of V_P in the Monte Carlo simulation so that I draw random values for V_P from the application of the latter. This random values of V_P were plugged into the locally calibrated relation observed for V_P and ρ. Random values for density, ρ_{MC}, were then generated in this process. For each value of ρ_{MC} computed using the Monte Carlo simulation I take the difference with the observed value for ρ in the well log data, resulting in a sample of $\Delta\rho = \rho - \rho_{MC}$. From this sample of $\Delta\rho$, the standard deviation $\sigma_{\Delta\rho}$ was calculated

The correlated Monte Carlo for density was then carried out. It consists of using the random values of V_P into the locally calibrated relationship between V_P and ρ, generating a sample of density values from V_P. I added then a random Gaussian error with zero mean and variance equal to the variance of the residuals from the V_P–ρ regression, $\sigma_{\Delta\rho}$. The results obtained from the procedure described above are presented next.

EFFECT OF DEPTH

Figures 3.14, 3.15, 3.16, 3.17, 3.18, 3.19, and 3.20 show the results obtained from the Monte Carlo simulation after applying the observed spatial variability for different depths. These figures show also four different crossplots that are used in many cases as sensitive to the fluid content (which were discussed in Section 3.3). As discussed by Castagna et al. (1993), a better fluid discrimination power is associated with shallow reservoirs than deeper ones. This conclusion can be verified in Figures 3.14 to 3.20. Next, I discussed the effect of depth in each crossplot contained in the figures separately.

The top/left plots in Figures 3.14 to 3.20 show the V_P/V_S versus V_P crossplot. The wet sand case in all figures shows a distribution of points that go along a thin line corresponding to the fact that V_S was calculated from V_P as discussed in Section 3.2. The observed correlation in the V_P/V_S ratio and V_P presents a more wide spread of values when the fizz-gas case ($S_w = 0.95$) and the gas case ($S_w = 0.50$) are considered. This result is because the fluid substitution technique introduces the variability observed in the rock properties associated with some specific depth in the values of the V_P/V_S ratio and V_P. In addition, the observed distribution of points in this crossplot is non-circular, presenting an asymmetrical shape. If we assumed that the distribution of points can be approximated by an ellipse, we can described the elliptical distribution of points as tending to have a larger aspect ratio with increasing depth (the ellipse becomes tight with increasing depth). When the wet sand, fizz-gas, and gas cases are evaluated as a function of the depth, all cases converge for small values of the V_P/V_S ratio and highest values of V_P at deeper reservoirs. In reservoirs deeper than $\sim$ 2km, these 3 distributions of points tend to superimpose to each other.

The overall conclusion in this result is that in deeper reservoirs, any estimation about the fluid content characterization obtained taking into account the V_P/V_S ratio versus V_P crossplot should included a rigorous investigation and evaluation of its reliability.

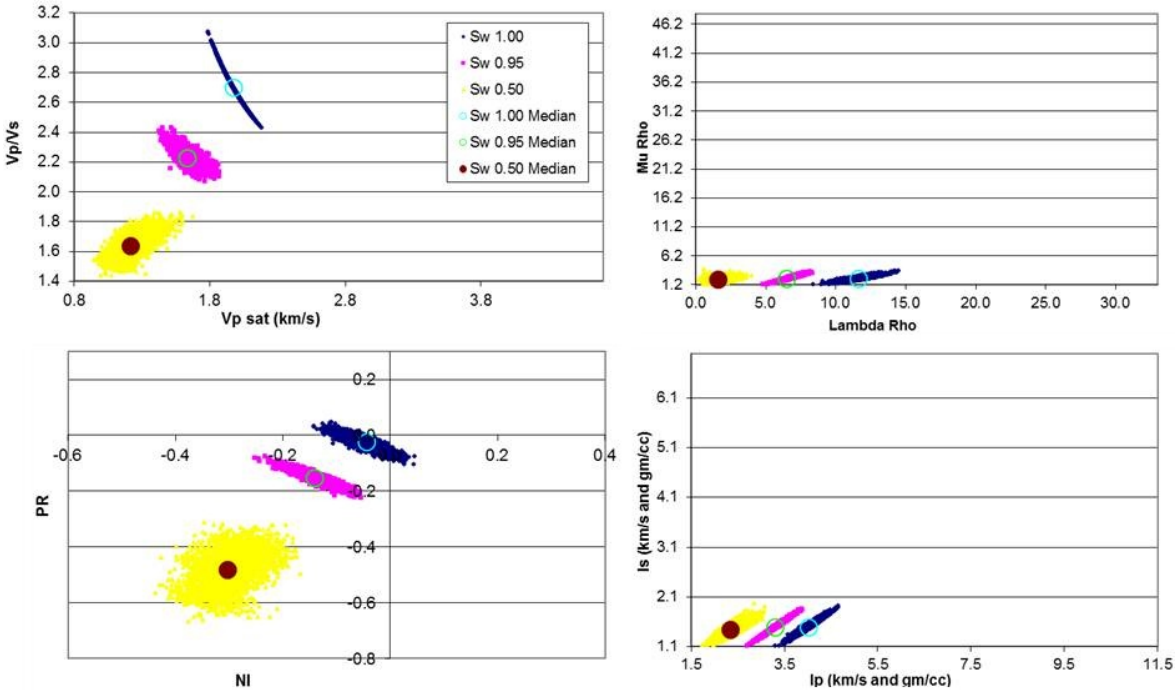

Figure 3.14: Different crossplots which are sensitive to fluid discrimination at depth= 0.64 km. Left/top: Vp/Vs vs. Vp. Right/top: $\mu\rho$ vs. $\lambda\rho$. Left/bottom: PR vs. NI. Right/bottom: I_S vs. I_P. In all plots, the symbols are: Blue/square: sample data points for wet sand (Sw= 1.0). Magenta/square: fizz gas case. Yellow/triangle: gas reservoir case ($S_{,} = 0.50$). The big circle inside the distribution of points corresponds to its respective median point.

The bottom/left plots in Figures 3.14 to 3.20 show the PR versus NI crossplot. This crossplot presents the wider spread of values compared to the other crossplots presented in these figures. One possible explanation for this result is because the NI versus PR crossplot incorporates all observed spatial variability related to the original information in the well log dataset (the NI and PR calculation also include the shale properties values). The distributions obtained using the Monte Carlo simulation again

presents an asymmetrical shape, resembling an elliptical distribution of points. As in the case of the V_P/V_S versus V_P crossplot, the wet sand, fizz-gas, and gas distributions of points become close to each other with increasing depth. Also, in reservoirs deeper than $\sim$2km, these 3 distributions of points tend to superimpose at least partially to each other. Thus, the overall conclusion in this result is that in deeper reservoirs, any estimation about the fluid content characterization obtained taking into account the PR versus NI crossplot should included a rigorous investigation and evaluation of its reliability.

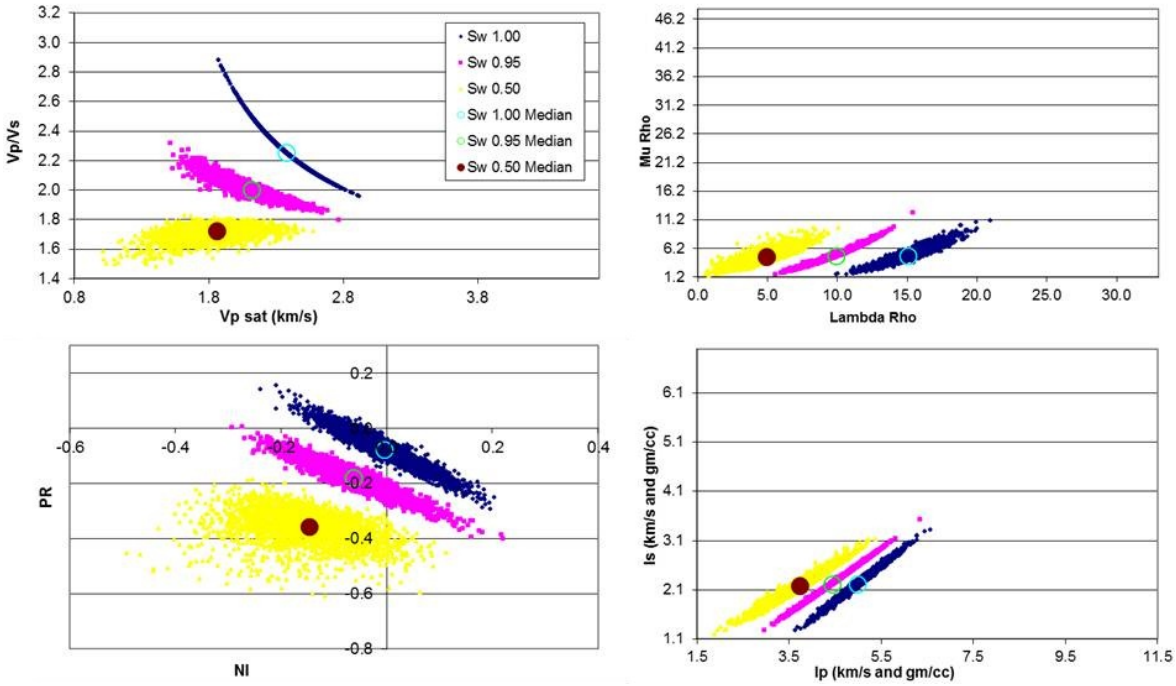

Figure 3.15: Different crossplots which are sensitive to fluid discrimination at depth= 1.25 km. Left/top: Vp/Vs vs. Vp. Right/top: $\mu\rho$ vs. $\lambda\rho$. Left/bottom: PR vs. NI. Right/bottom: I_S vs. I_P. In all plots, the symbols are: Blue/square: sample data points for wet sand (Sw= 1.0). Magenta/square: fizz gas case. Yellow/triangle: gas reservoir case ($S_{,} = 0.50$). The big circle inside the distribution of points corresponds to its respective median point.

The left/top plots in Figures 3.14 to 3.20 show the $\lambda\rho$ versus $\mu\rho$ crossplot. As in

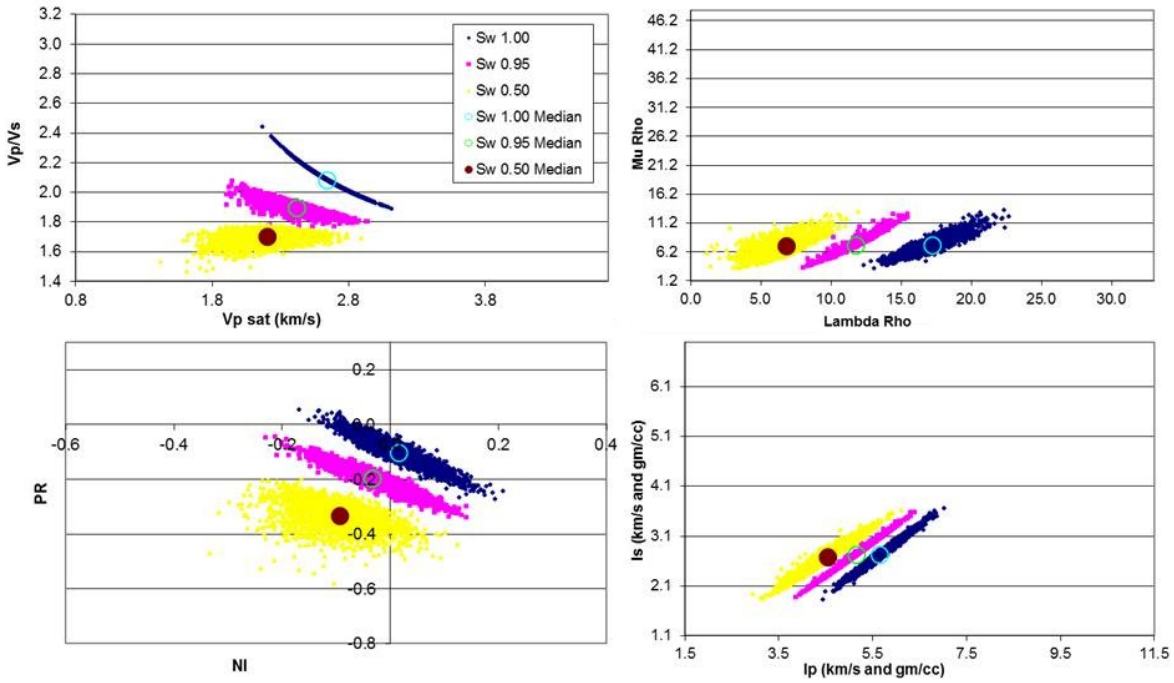

Figure 3.16: Different crossplots which are sensitive to fluid discrimination at depth= 1.62 km. Left/top: Vp/Vs vs. Vp. Right/top: $\mu\rho$ vs. $\lambda\rho$. Left/bottom: PR vs. NI. Right/bottom: I_S vs. I_P. In all plots, the symbols are: Blue/square: sample data points for wet sand (Sw= 1.0). Magenta/square: fizz gas case. Yellow/triangle: gas reservoir case ($S_{,} = 0.50$). The big circle inside the distribution of points corresponds to its respective median point.

the previous crossplots, the spread of the data points increases with depth. Again, the distributions of data points obtained using the Monte Carlo simulation presents an asymmetrical shape, resembling an elliptical distribution of points. However, when the $\lambda\rho$ versus $\mu\rho$ crossplot is compared to the other crossplots, it presents an interesting property: the distributions move along approximately parallel curves with increasing depth. The "distance" measured along the $\lambda\rho$ axis seems to be constant with depth. Thus, the depth seems to have a less important effect in the fluid discrimination in the $\lambda\rho$ versus $\mu\rho$ crossplot. This result can suggest that the $\lambda\rho$ versus $\mu\rho$ crossplot could be a more reliable source for fluid discrimination than the other

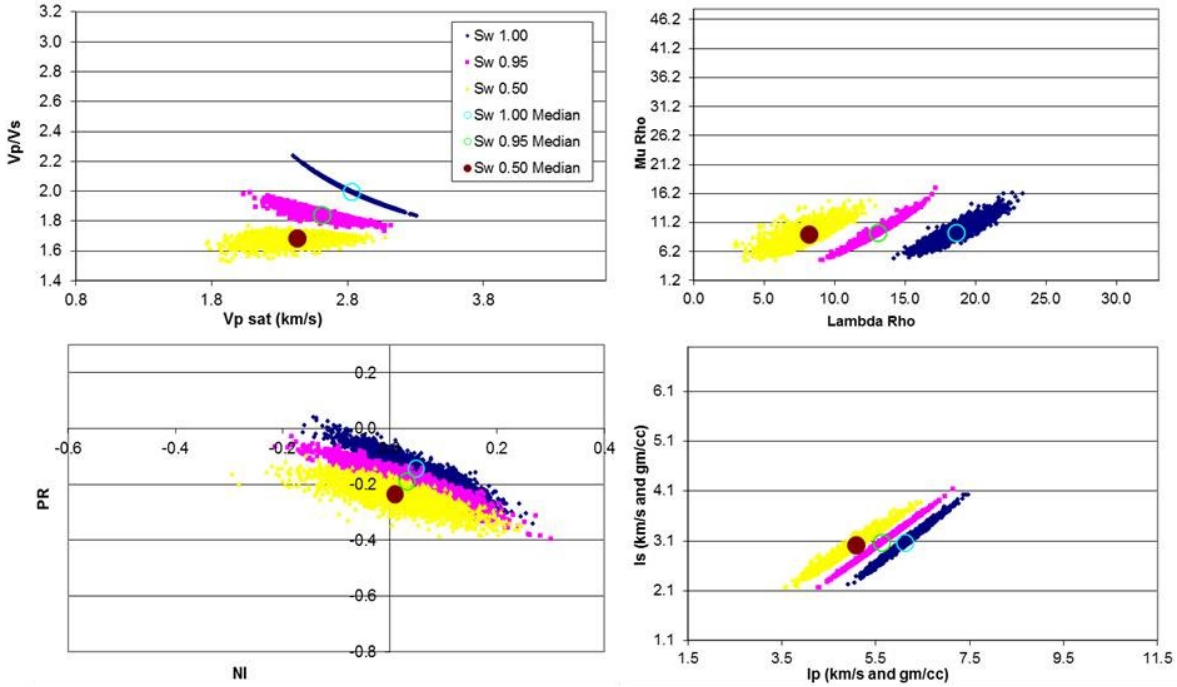

Figure 3.17: Different crossplots which are sensitive to fluid discrimination at depth= 2.10 km. Left/top: Vp/Vs vs. Vp. Right/top: $\mu\rho$ vs. $\lambda\rho$. Left/bottom: PR vs. NI. Right/bottom: I_S vs. I_P. In all plots, the symbols are: Blue/square: sample data points for wet sand (Sw= 1.0). Magenta/square: fizz gas case. Yellow/triangle: gas reservoir case ($S_{,} = 0.50$). The big circle inside the distribution of points corresponds to its respective median point.

crossplots considered in this study. As discussed in the last section, however, the use of the $\lambda\rho$ versus $\mu\rho$ crossplot to perform fluid discrimination should also be subject to rigorous investigation, because any noise presented in the data will also be magnified by this kind of attribute together with the fluid effect.

The bottom/right in Figures 3.14 to 3.20 show the last of the crossplots used in this investigation: I_P versus I_S. As in the case of the V_P/V_S versus V_P and PR versus NI crossplots, the wet sand, fizz-gas, and gas distributions of points become close to each other with increasing depth. The overall conclusion obtained from the I_P versus I_S crossplot is that in deeper reservoirs, any estimation about the fluid

content characterization obtained taking into account this crossplot should included a rigorous investigation and evaluation of its reliability.

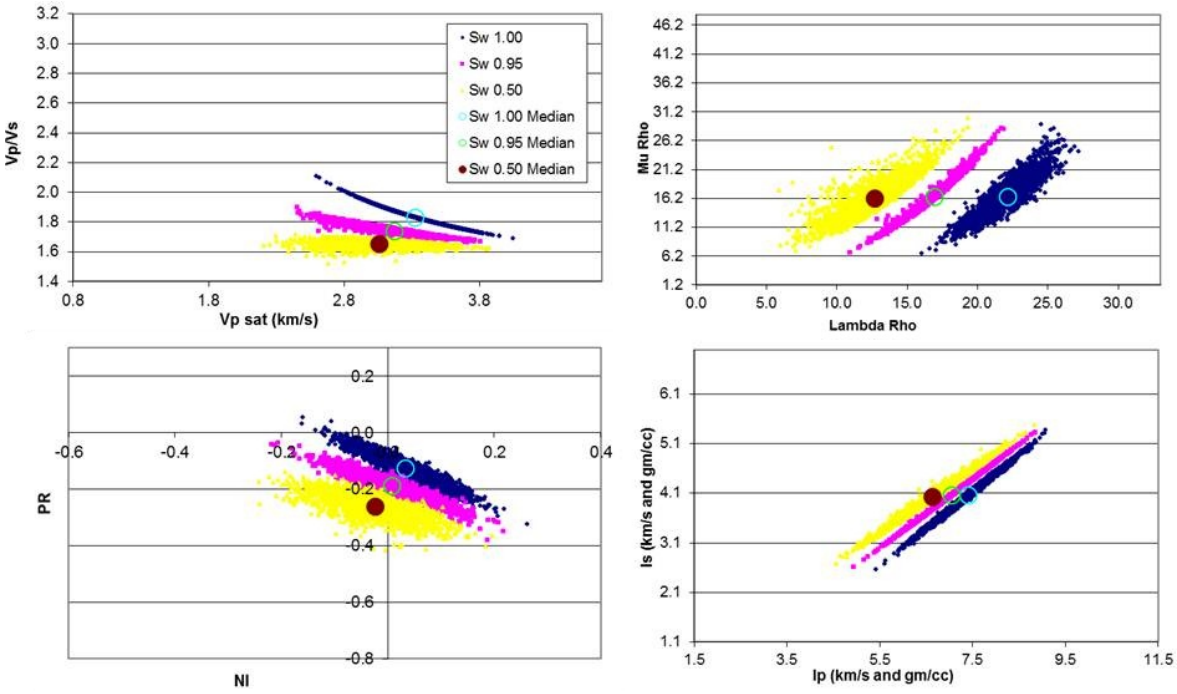

Figure 3.18: Different crossplots which are sensitive to fluid discrimination at depth= 2.90 km. Left/top: Vp/Vs vs. Vp. Right/top: $\mu\rho$ vs. $\lambda\rho$. Left/bottom: PR vs. NI. Right/bottom: I_S vs. I_P. In all plots, the symbols are: Blue/square: sample data points for wet sand (Sw= 1.0). Magenta/square: fizz gas case. Yellow/triangle: gas reservoir case ($S_{,} = 0.50$). The big circle inside the distribution of points corresponds to its respective median point.

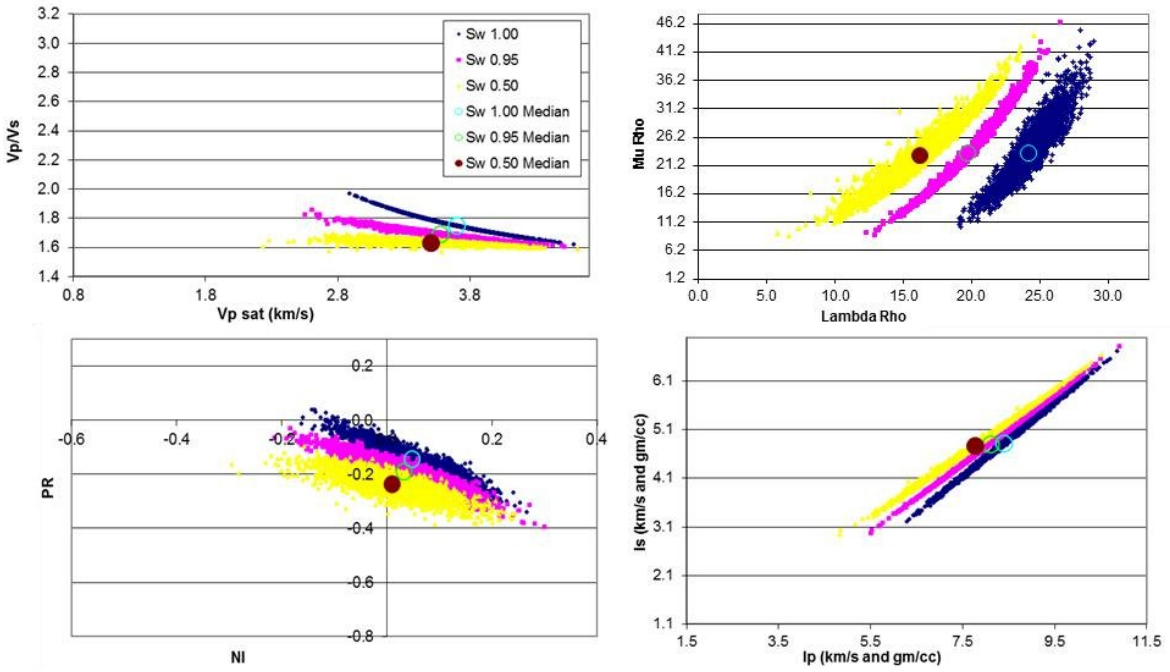

Figure 3.19: Different crossplots which are sensitive to fluid discrimination at depth= 3.40 km. Left/top: Vp/Vs vs. Vp. Right/top: $\mu\rho$ vs. $\lambda\rho$. Left/bottom: PR vs. NI. Right/bottom: I_S vs. I_P. In all plots, the symbols are: Blue/square: sample data points for wet sand (Sw= 1.0). Magenta/square: fizz gas case. Yellow/triangle: gas reservoir case ($S_{,} = 0.50$). The big circle inside the distribution of points corresponds to its respective median point.

GENERAL COMMENTS

The results presented in this section revealed that the depth has an important effect on the fluid discrimination reliability when we consider the observed spatial variability of the measured well log data for each depth. As expected, shallow reservoirs present a better fluid discrimination power, allowing clearly the discrimination of wet sand, fizz-gas, and gas-reservoirs in the case studied in this thesis. When the reservoirs go deeper, a larger concern was identified in the predicted fluid discrimination results. In any case, rigorous investigation and evaluation of the reliability of the fluid discrimination process should be adopted before any conclusion can be

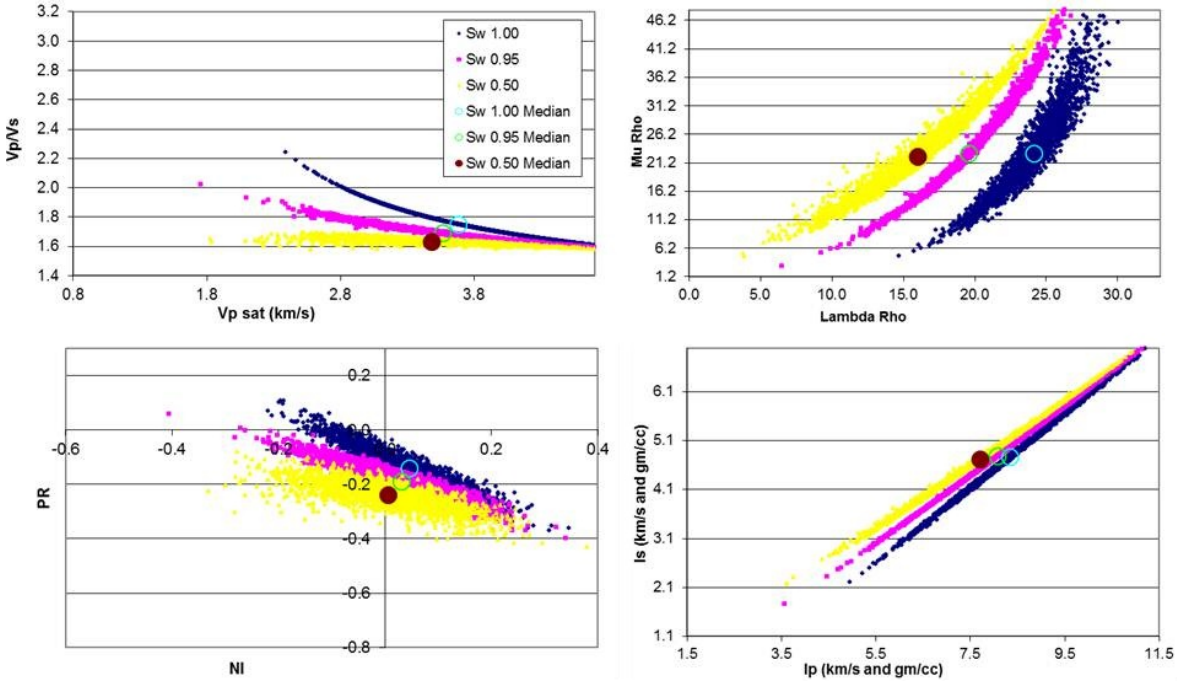

Figure 3.20: Different crossplots which are sensitive to fluid discrimination at depth= 3.57 km. Left/top: Vp/Vs vs. Vp. Right/top: $\mu\rho$ vs. $\lambda\rho$. Left/bottom: PR vs. NI. Right/bottom: I_S vs. I_P. In all plots, the symbols are: Blue/square: sample data points for wet sand (Sw= 1.0). Magenta/square: fizz gas case. Yellow/triangle: gas reservoir case ($S_{,} = 0.50$). The big circle inside the distribution of points corresponds to its respective median point.

presented. Nevertheless, the fluid substitution results were considered robust in most conditions investigated in this thesis, allowing discrimination of gas, fizz gas, and water saturated reservoirs in at least one of the attributes that respond to the fluid content (the $\lambda\rho$ versus $\mu\rho$ crossplot).

The observed variability in the well log data for a specific depth takes into account all the empirical trends associated with the subsurface geology in the available surveyed area. Thus, this suggests that the framework described in this chapter could be applied in the exploration of areas associated with regions analogous to the Gulf of Mexico (shallow offshore). This framework could be used in the process of

the GRV estimation necessary to apply Equations 2.1 and 2.2, since the fluid substitution method can be used to constrain the delineation of the top and base of hydrocarbon reservoirs. Another use of the results obtained with this framework is that this methodology could be used to roughly estimate, using seismic data, the hydrocarbon saturation needed to perform the volumetric calculation if the following assumptions can be verified: 1) the results obtained from the methodology described in this chapter allows the discrimination of the fluid content in hydrocarbon reservoirs; 2) This fluid discrimination power goes through the seismic bandwidth. If these two assumptions are correct, the framework could allow the estimate of the missing parameter in the HCPV calculation: a hydrocarbon saturation distribution map.

Chapter 4

Summary of conclusions

The main objective of this study was to understand how the uncertainties in the geophysical parameters needed to evaluate the hydrocarbon pore volume (HCPV) can be used to obtain a more reliable estimation of it. In the first part of this thesis, the uncertainties of the parameters used to calculate the HCPV were used to estimate a range of HCPV values for Blackfoot reservoir (AB-Canada). Two different approaches were used to link the range of estimated HCPV values to their likelihood. The results obtained using these two approaches presented compatible hydrocarbon volume estimations for the Blackfoot pool, with P10$\sim$ 12 MMbbl, P50$\sim$ 8 MMbbl, and P90$\sim$ 5 MMbbl. One of these methodologies, the Taylor expansion approach, can be used to link deterministic estimations of single values for HCPV to probabilities — if uncertainty estimations for the source parameters needed for the HCPV prediction are available. Investigation about the source of uncertainty in seismic data reveals that the time picking error could explain, in the case of the Blackfoot reservoir, the

uncertainty in the thickness parameter. Further investigation is needed to confirm this last result.

An additional case was used to compare the results obtained from the Taylor expansion approach and the Monte Carlo simulation approach. This last case can not be used to test the uncertainty evaluation methodology used for the Blackfoot reservoir, but can be useful to compare the predictions obtained from the two methodologies. In this additional case, a Taylor expansion approach that adopts the HCPV as a lognormal distribution makes the match between the CDFs from both approaches similar even in the tails of the PDFs. This shows that the HCPV distribution is a lognormal distribution as expected by the theory when the source parameters are independent to each other (Murtha, 2002).

In the second part of this thesis, well log data from Gulf of Mexico revealed a temperature gradient described by the equation $T(^{\circ}C) = 19.45 \cdot depth(km) + 25.01$, which is in agreement with the gradient presented by Husson et al. (2008). Gradients for pore pressure, overburden pressure, porosity, density for shale and for wet sand, P-wave velocity for shale and for wet sand were also estimated from the well log data, and are in agreement with previous results for Gulf of Mexico (Hilterman, 2001, Castagna et al., 1993, Husson et al., 2008).

The results obtained from this second part of the thesis also revealed that the depth has an important effect on the fluid discrimination reliability when we consider the observed spatial variability of the measured well log data. As expected, shallow reservoirs present a better fluid discrimination power, clearly allowing the discrimination of wet sand, fizz-gas, and gas-reservoirs. When the reservoirs go deeper, a larger

concern about the fluid discrimination was identified in the predicted results. In any case, rigorous investigation and evaluation of the reliability of the fluid discrimination process should be adopted before any conclusion can be presented. Nevertheless, the fluid substitution results were considered robust in most conditions investigated in this project, allowing discrimination of gas, fizz gas, and water saturated reservoirs in at least one of the attributes that respond to the fluid content (the $\lambda\rho$ versus $\mu\rho$ crossplot).

The observed variability in the well log data for a specific depth takes into account all the empirical trends associated with the subsurface geology in the available surveyed area. This suggests that the framework described in this second part of the thesis could be applied in the exploration of areas associated with the regions analogous to Gulf of Mexico (shallow offshore). This framework could also be used in the process of the GRV estimation/delineation necessary to apply volumetric calculations since the fluid substitution method can be used to constrain the delineation of the top and base of hydrocarbon reservoirs. Another use of the results obtained with this framework is that this methodology could be used to roughly estimate, using seismic data, the hydrocarbon saturation needed to perform the volumetric calculation if the following assumptions can be verified: 1) the results obtained from the methodology described in chapter 3 allow the discrimination of the fluid content in hydrocarbon reservoirs; 2) This fluid discrimination power goes through the seismic bandwidth. If these two assumptions are correct, the framework could allow the estimate of the missing parameter in the HCPV calculation: the hydrocarbon saturation distribution map, which could be obtained in the same way as the other source parameters used to perform the HCPV calculation.

Chapter 5

Future work

From the results presented in this thesis, different lines of investigation can be proposed as future work. Among them are:

- One of the most important lines of investigation associated with the results obtained with the methodology proposed in Chapter 2 is the comparison of their predicted CDFs with the CDFs obtained directly from real oil industry evaluation. This comparison would allow the validation of the methodology used in this thesis.

- The methodology presented in Chapter 2, where the uncertainty in the source parameters of the volumetric equation were extracted from the comparison between the well log data and the predicted one, was applied only for the Blackfoot reservoir. It would be very important to evaluate the obtained results in different reservoirs. Then, the results obtained in Chapter 2 should be verified with the application of the methodology in different reservoirs in a future work.

• One of the assumptions involved with the two approaches described in Chapter 2 is that the source parameters are assumed independent of each other. If this is not the case, both approaches can consider dependence between source parameters. Thus, one line of investigation that could be developed in a future work involves the application of the two approaches in a case where there are dependencies between source parameters. Some questions that could be asked are: How the results presented in this thesis are affected in this case? How does the uncertainty degree change because of this consideration?

• The association between the time picking error and the thickness uncertainty estimated using the geostatistic analysis is interesting, but should be investigated more thoroughly. If confirmed by further investigation, this association would be a very important result because this could allow the prediction of the thickness uncertainty directly from the seismic data. A detailed investigation about the relation between the geophysical data and the error estimate in the source parameters of the volumetric equation should be performed in a more constrained experiment. The signal-to-noise ratio associated with the seismic data should also be better defined. Attempts to link the S/N ratio associated with the properties of the seismic acquired data to the one in the seismic interpreted data should be performed. The Meunier equation presents a good starting point.

• Another possibility for investigation would be to use the errors in the parameters associated with the distribution maps to perform a kriging estimation of the errors. This would allow a quantification of an uncertainty surface associated with each one of the distributions maps used in the volumetric estimation. With an uncertainty surface associated with each one of the source parameters a new methodology could

be developed. The evaluation of this procedure should be investigated/developed in a future work.

• The Taylor expansion methodology can be easily used in optimizing problems. Thus, the Taylor expansion methodology could be used to obtain a best volumetric model from the geostatistical analysis and the *blind well* procedure, using the comparison between the HCPV obtained from the volumetric method and a estimation for HCPV obtained by a different method (e.g. material balance method).

• The results obtained from Chapter 3 were obtained from a well log dataset which did not present other useful properties which could be important in the characterization of the region samples in the well log data. Among these properties are the volume of shale, resistivity logs, and DTS logs/properties. An interesting line of investigation would be to apply the methodology described in Chapter 3 with a well log dataset containing all information needed to perform a wide and thoroughly investigation.

• Another line of research could be to investigate whether the fluid discrimination results obtained in Chapter 3 can be verified also in seismic data. If the result is verified, then seismic data could be used to estimate the hydrocarbon saturation.

• One consequence of the evaluation related to the above, is the generation of a hydrocarbon saturation distribution map. For example, if the results associated with Chapter 3 can be applied to the Blackfoot reservoir, this would allow the estimation of the hydrocarbon saturation distribution map using the methodologies applied by Todorov (2000) to obtain the thickness, percentage of sand, and porosity distribution maps. With the hydrocarbon saturation distribution map, a net pay thickness could

be estimated using seismic data. This distribution map could be used as a new constraint in the volumetric calculation.

Bibliography

[1] Abrahamsen, P., R. Hauge, K. Heggland, and P. Mostad, 1998, *Uncertain cap rock geometry, spill point and gross rock volume*: SPE 49186, Soc. Petroleum Engineers.

[2] Asquith, G., and D. Krygowski, 2004. *Basic well log analysis*: AAPG Methods in Exploration Series No. 16, Amer. Assoc. of Petr. Geol., 244pp.

[3] Avseth, P., T. Mukerji, and G. Mavko, 2005, *Quantitative seismic interpretation*: Cambridge University Press, 358pp.

[4] Bachrack, R., et al., 2007, *From pore-pressure prediction to reservoir characterization: A combined geomechanics-seismic inversion workflow using trend-kriging techniques in a deepwater basin*: The Leading Edge, v. 26, p. 590-595.

[5] Berryman, J.G., and G.W. Milton, 1991, *Exact results for generalized Gassmanns equation in composite porous media with two constituents*: Geophysics, v. 56, p.1950-1960.

[6] Bratvold, R.B., S.H. Begg, 2008, *I would rather be vaguely right than precisely wrong: a new approach to decision making in the petroleum exploration and production industry*: Amer. Assoc. of Petr. Geol. Bulletin, v. 92, p. 1373-1392.

[7] Brown, A.R., et al., 2011, *Interpretation of three-dimensional seismic data*: Amer. Assoc. of Petr. Geol., 646pp.

[8] Castagna, J.P., 1993a, *AVO analysis: tutorial and review:* in Castagna, J.P. and Backus, M.M., eds., Offset-dependent reflectivity – Theory and practice of AVO anomalies, Soc. Expl. Geophysis. Investigations in Geophysics No. 8, p3-36.

[9] Castagna, J.P., 1993b, *Rock Physics – the link between rock properties and AVO response*: in Castagna, J.P. and Backus, M.M., eds., Offset-dependent reflectivity – Theory and practice of AVO anomalies, Soc. Expl. Geophysis. Investigations in Geophysics No. 8, p. 135-171.

[10] Chaveste, A. and F. Hilterman, 2007, *Well-log inversion and modeling – A tool for understanding ambiguity and sensitivity of seismic data to changes in petrophysical properties*: The leading edge, v. 26, p. 812-817.

[11] Coleman, H.W. and W.G. Steele, 2009, *Experimentation, validation, and uncertainty analysis for engineers*: John Wiley and Sons, 317pp.

[12] Dean, L., 2007, *Volumetric Estimation - Part 3*: Reservoir, Canadian Society of Petroleum Geologists, issue 11, p. 20-23.

[13] Demirmem, F., 2007, *Reserves estimation – the challenge for the industry*: Journal of Petroleum Technology, vol. 59, p. 80-89. Also paper SPE 103434, Soc. Petroleum Engineers.

[14] Deutsch, C.V., 2002, *Geostatistical reservoir modeling*: Oxford University Press, 376pp.

[15] Dubrule, O. 2003. *Geostatistic for seismic data integration in earth models*: Cambridge University Press, 359pp.

[16] Ezekwe, N., 2011, *Petroleum reservoir engineering practice*: Prentice Hall, 770pp.

[17] Feng, H., 2009, *Hydrocarbon indicators derived from AVO analysis*: MS Thesis, University of Calgary, 103pp.

[18] Garotta, R., Marechal, P., and Megesan, M., 1985, *Two-component acquisition as a routine procedure for recording P-waves and converted waves*: Journal of the Canadian Society of Exploration Geophysicists, v. 21, p. 40-53.

[19] GEPRR, 2001, *SPE/WPC/AAPG Guidelines for the evaluation of petroleum reserves and resources*: Soc. Petroleum Engineers, 141pp.

[20] Goodway W. and D.J. Tessman, 2001, *Blackfoot 3C-3D: a VectorSeisTM case history*: CSEG Extended Abstracts, p. 14-17.

[21] Goodway, B., T. Chen, and J. Downton, 1997, *Improved AVO fluid detection and lithology discrimination using Lam petrophysical parameters; lr, mr and l/m fluid stack, from P and S inversions*: 67th Ann. Internat. Mtg., Soc. Expl. Geophys., Expanded abstracts, p. 183-186.

[22] Greenberg, M.L., J.P. Castagna, 1992, *Shear-wave velocity estimation in porous rocks: Theoretical formulation, preliminary verification and applications*: Geophys. Prosp., v. 40, p. 195-209.

[23] Han, De-hua, and M.L. Batzle, 2004, *Gassmann's equation and fluid-saturation effects on seismic velocities*: Geophysics, v. 69, p. 398-405.

[24] Hilterman, F., 2001, *Seismic amplitude interpretation*: Distinguished instructor series No. 4, Soc. of Expl. Geophys., 235pp.

[25] Husson, L., P. Henry, and X. Le-Pichon, 2008, *Thermal regime of the NW shelf of the Gulf of Mexico. Part A: Thermal and pressure fields*: Bull. Soc. Geol. Fr., v. 179, no. 2, p. 129-137.

[26] Isaaks, E.H. and R.M. Srivastava, 1989, *An introduction to applied geostatistics*: Oxford University Press, 561pp.

[27] Lawton, D.C., R.R. Stewart, A. Cordsen, and S. Hrycak, 1996, *Design review of the Blackfoot 3C-3D seismic program*: Crewes Research Report, v. 8.

[28] Lu, H-x., and G. Margrave, 2001, *Reprocessing the 1999 Blackfoot 3C-3D seismic data and anisotropy analysis for the radial component*: Crewes Research Report, v. 13.

[29] McCormack, M.D., J.A. Dunbar, and W.W. Sharp, 1984, *A case study of stratigraphic interpretation using shear and compressional seismic data*: Geophysics, v. 49, p. 509-520.

[30] Mavko, G., T. Mukerji, and J. Dvorkin, 2009, *The rock physics handbook*: Cambridge University Press, 511pp.

[31] Meunier, J. 2011, *Seismic acquisition from yesterday to tomorrow*: Distinguished instructor series No. 14, Soc. of Expl. Geophys., 236pp.

[32] Miller, S.L.M., 1996, *Multicomponent seismic data interpretation*: MS Thesis, University of Calgary, 85pp.

[33] Miller, R.L., and J.S. Kahn, 1962, Statistical analysis in the geological sciences: John Wiley and Sons, 483pp.

[34] Murtha, J.A., 2002, *Sums and products of distributions: rules of thumb and applications*: SPE 77422, Soc. Petroleum Engineers.

[35] Murtha, J.A. and J. Ross, 2009, *Uncertainty and the volumetric equation*: Journal of Petroleum Technology, Guest editorial, September 2009.

[36] PRMS 2007, *SPE/WPC/AAPG/SPEE Petroleum resources management system*: Soc. Petroleum Engineers, 47pp.

[37] PRMS-AD, 2011, *SPE/WPC/AAPG/SPEE/SEG Guidelines for application of the petroleum resources management system*: Soc. Petroleum Engineers, 197pp.

[38] Ringrose, P.S., 2007, *Myths and realities in upscaling reservoir data and models*: SPE 106620, Soc. Petroleum Engineers.

[39] Rose, P.R., 2001, *Risk analysis and management of petroleum exploration ventures*: Amer. Assoc. of Petr. Geol., AAPG Methods in Exploration Series No. 12, Amer. Assoc. of Petr. Geol., 164pp.

[40] Sidle, R.E., and W.J. Lee, 2011, *Qualifying seismic as a "reliable technology" – an example of downdip water-contact location*: SPE Economics and Management, p. 163-172.

[41] Smith, T., C.H. Sondergeld, and C.S. Rai, 2003, *Gassmann fluid substitutions: a tutorial*: Geophysics, v. 68, p.430-440.

[42] Stewart, R.R., S. Huddleston, and T. Kan, 1984, *Seismic versus sonic velocities: A vertical seismic profiling study*: Geophysics, v. 49, p. 1153-1168.

[43] Tearpock, D.J., 2011, *Petroleum resources and reserves: an overview of recommended geological practices*: AAPG 2011 annual meeting course, Houston-TX, April 14, 2011, 245pp.

[44] Todorov, T., 2000, *Integration of 3C-3D seismic data and well logs for rock property estimation*: MS Thesis, University of Calgary, 88pp.

[45] Todorov, T. and R.R. Stewart, 1997, *Geostatistical analysis of 3C-3D seismic data for depth, isopachs, and sand/shale distribution*: Crewes Research Report, vol. 9.

[46] US Securities and Exchange Commission, 2008, *Modernization of oil and gas reporting, conforming version (final)*: 17 CFR Parts 210, 211, 229, and 249, [Release Nos. 33-8995; 34-59192; FR-78; File No. S7-15-08], RIN 3235-AK00, US SEC, Washington, DC (29 December 2008), http://www.sec.gov/rules/final/2008/33-8995.pdf (downloaded 14 December 2009).

[47] Wang, Z., 2001, *Fundamentals of seismic rock physics*: Geophysics, v. 66, p. 398-412.

[48] Worthington, P.F., 2009, *Net pay: What is it? What does it do? How do we quantify it? How do we use it?*: SPE 123561, Soc. Petroleum Engineers.

[49] Zoback, M.D., 2010, *Reservoir geomechanics*, Cambridge University Press, 449pp.

Appendix A

Thickness error from the time picking error

The total thickness error is the maximum acceptable error in the thickness. This maximum error is obtained calculating the maximum thickness and the minimum thickness, in time, for a given time picking error estimation. This total thickness error in time is then the difference between the maximum acceptable time thickness and the minimum acceptable time thickness. Figure A.1 illustrates the approach.

The maximum time thickness is given by

$$thickness_{maximum} \;=\; thickness + \Delta t \;=\; thickness + 2t_e \tag{A.1}$$

and the minimum time thickness is given by

$$thickness_{minimum} \;=\; thickness - \Delta t \;=\; thickness - 2t_e \tag{A.2}$$

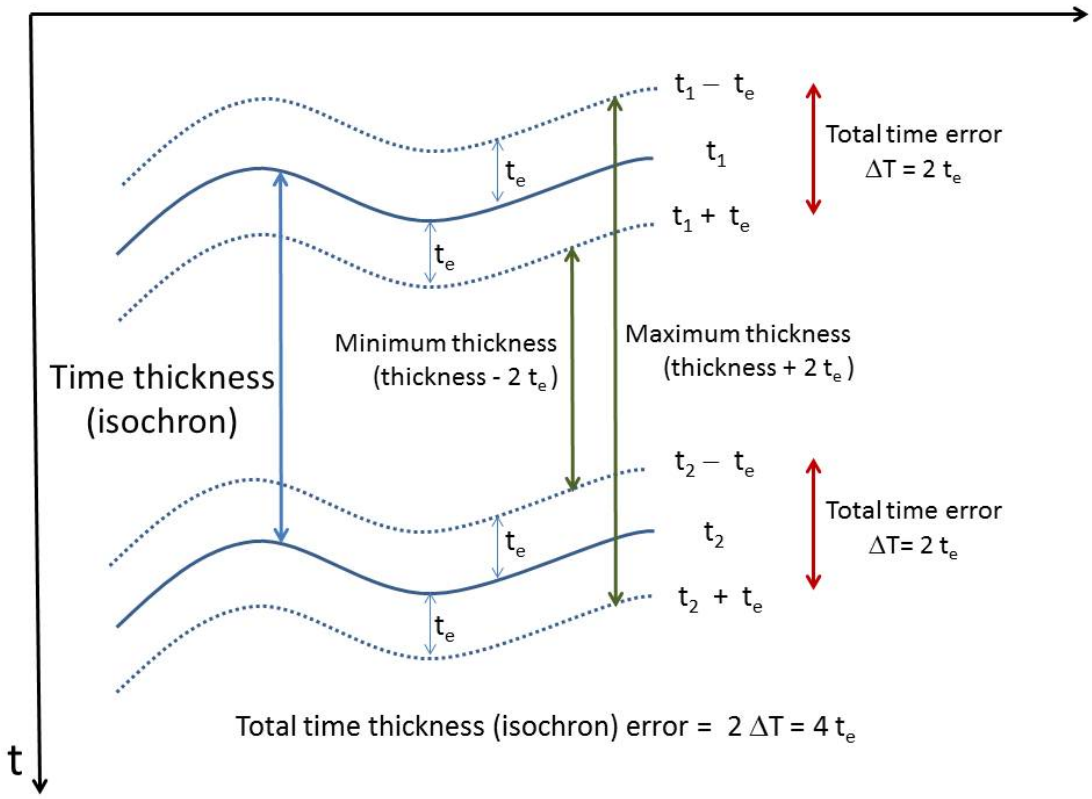

Figure A.1: Schematic for the total time picking error.

The total time thickness or isochron error is then

$$thickness_{error}^{time} \;=\; 2\Delta t \;=\; 4t_e \tag{A.3}$$

The relationship between the traveltime t and the depth z is given by

$$z \;=\; \frac{V\ t}{2} \tag{A.4}$$

We have that the relationship between the time picking error t_e and the error in depth is given by

$$\Delta z \;=\; \frac{V\ \Delta t}{2} \tag{A.5}$$

where $\Delta t \;=\; 2\,t_e$.

The total thickness error in depth is then

$$Thickness^{z}_{error} \;=\; \frac{V\ Thickness^{time}_{error}}{2} \tag{A.6}$$

and then

$$Thickness^{z}_{error} \;=\; \frac{V\ 4t_e}{2} \;=\; 2Vt_e \tag{A.7}$$